GFZ
Helmholtz Centre
POTSDAM

GeoMod2014

Modelling in Geosciences

Programme & Extended Abstracts

31 August - 5 September 2014

Editors:
Kirsten Elger
Øystein Thordén Haug
Malte Ritter

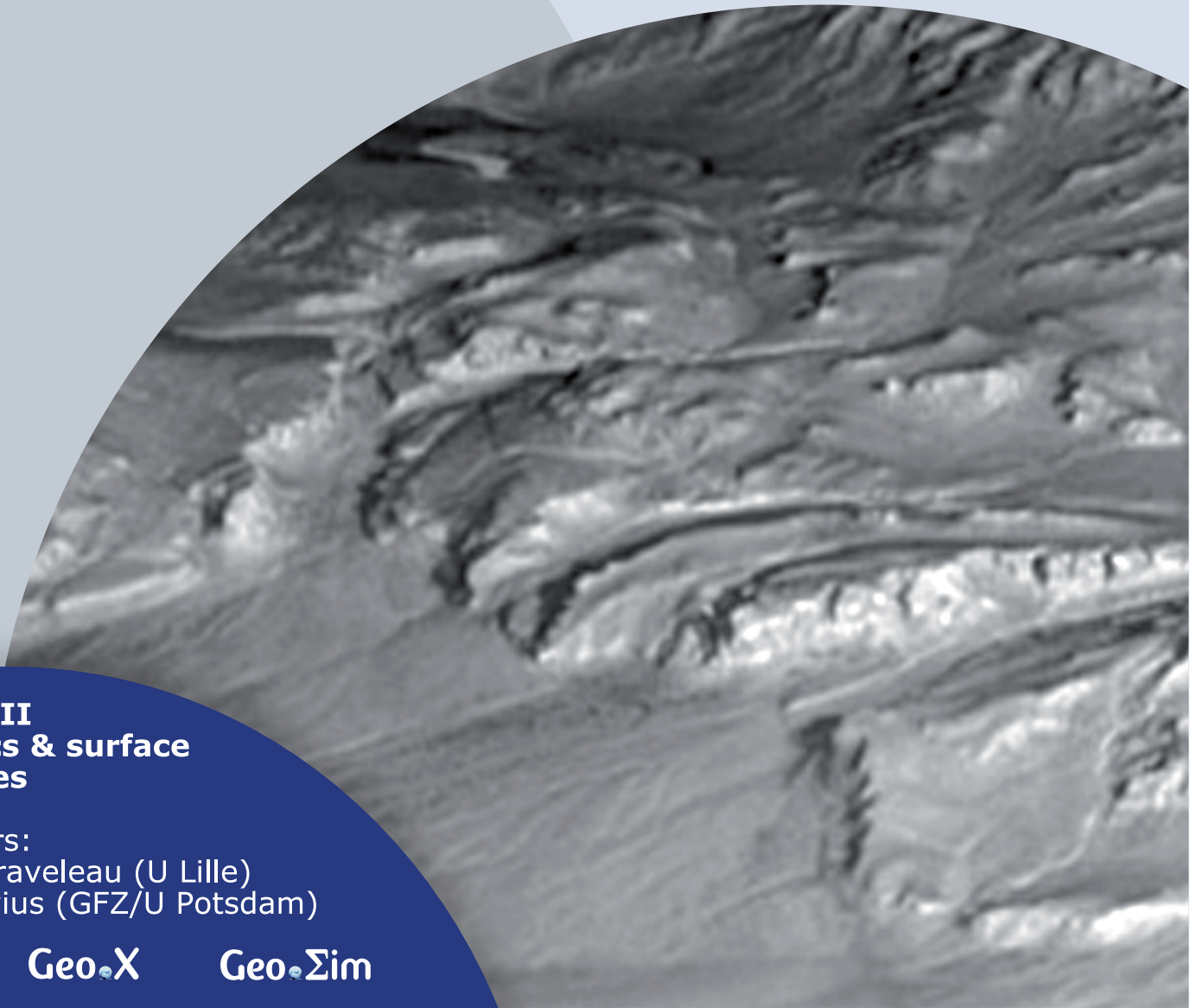

Session II
Tectonics & surface processes

Conveners:
Fabien Graveleau (U Lille)
Niels Hovius (GFZ/U Potsdam)

DFG GeoX GeoΣim

Recommended Citation

Elger, K; Haug, Ø. T.; Ritter, M. C. (Eds), (2014): Proceedings of GeoMod2014 – Modelling in Geosciences: Programme and Extended Abstracts 31 August–5 September 2014, GeoMod2014 – Modelling in Geosciences (Potsdam 2014), Potsdam: GFZ German Research Centre for Geosciences. DOI: http://doi.org/10.2312/GFZ.geomod.2014.001.

Disclaimer and Copyright

Imprint

Publisher
Helmholtz Centre Potsdam
GFZ German Research Centre for Geosciences
Telegrafenberg
14473 Potsdam
Published in Potsdam, Germany

Editors
Kirsten Elger
Øystein T. Haug
Malte C. Ritter

doi: 10.2312/GFZ.geomod.2014.001

About this book

This volume contains the extended abstracts of contributions presented during GeoMod 2014 at the Helmholtz Centre Potsdam GFZ German Research Centre for Geosciences (GFZ Potsdam), showing the state of the art of the tectonic modeling community.

GeoMod is a biennial conference dedicated to latest results of analogue and numerical modelling of lithospheric and mantle deformation. It started in 2002 in Milan as RealMod2002, then moved to Lucerne (GeoMod2004), Florence (2008), Lisbon (2010), and Lausanne (2012).

GeoMod2014 took place from 31 August to 3 September 2014 with 138 participants from 25 countries on all continents. The scientific programme of GeoMod2014 was organized in seven topical sessions listed below. The conference was followed by a 2-day short course on "Constitutive Laws: from Observation to Implementation in Models" (including lectures, lab visits, and practical exercises), as well as a 1-day hands-on tutorial on the ASPECT numerical modelling software.

GeoMod2014 focused on rheology and deformation at a wide range of temporal and spatial scales: from earthquakes to long-term deformation, from microstructures to orogens and subduction systems. For the first time, the discipline of volcanotectonics was included, while the (mantle) geodynamics community was more strongly represented than in previous editions. The bridge to field geology has traditionally been strong. At GeoMod 2014, fitting to the focus on rheology, the rock mechanics community was also represented. We thank our sponsors DFG, GFZ Potsdam and Geo.X, the conveners and all participants for contributing to a successful conference.

The GeoMod2014 Committee

The Scientific Committee
Onno Oncken
Georg Dresen
Stephan Sobolev
Matthias Rosenau
Karen Leever

The Organising Committee
Kirsten Elger
Franziska Alberg
Students support: Zahra Amirzada, Felix Eckelmann, Øystein Thordén Haug, Shaoyang Li, Malte Ritter, Tasca Santimano, Sarah Schröder, Johannes Wagner

Sessions, Conveners, and keynote speakers

(Seismo-)tectonics
Conveners: Boris Kaus (U Mainz), Onno Oncken (GFZ/FU Berlin),
Keynotes: Kelin Wang (Geological Survey Canada, Alberta), Bertrand Maillot (U Cergy-Pontoise)

Tectonics & Surface Processes
Conveners: Fabien Graveleau (U Lille), Niels Hovius (GFZ/U Potsdam),
Keynotes: Ritske Huismans (U Bergen), Stéphane Dominguez (U Montpellier II)

Volcanism and Volcanotectonics
Conveners: Olivier Galland (U Oslo), Eoghan Holohan (GFZ)
Keynotes: Rikke Pedersen (U Iceland), Olivier Roche (U BP Clermont-Ferrand)

Geodynamics
Conveners: Francesca Funiciello (U Roma Tre), Stephan Sobolev (GFZ),
Keynotes: Anne Davaille (U Paris-Sud), Bernhard Steinberger (GFZ)

Rheology
Conveners: Georg Dresen (GFZ/U Potsdam), Hiroki Sone (GFZ),
Keynotes: Yuri Fialko (U California), Laurent Montési (U Maryland)

Fluids and Deformation
Conveners: Stephen Miller (U Bonn), Marcos Moreno Switt (GFZ),
Keynotes: Boris Galvan (U Bonn), Takeshi Tsuji (U Kyushu)

Methods and Materials (poster-only session)
Conveners: Matthias Rosenau (GFZ), Marcel Frehner (ETH Zürich)

Short course on "Constitutive Laws: from Observation to Implementation in Models"
Lecturers: Onno Oncken (GFZ Potsdam), Matthias Rosenau (GFZ Potsdam), Fabio Corbi (GFZ Potsdam), Georg Dresen (GFZ Potsdam), Stephan Sobolev (GFZ Potsdam), Sascha Brune (U Sydney)

Hands-on tutorial on "ASPECT: a next-generation geodynamic modelling software"
(Advanced Solver for Problems in Earth's ConvecTion)
Lecturers: Anne Glerum (Utrecht University), Juliane Dannberg (GFZ Potsdam). Supervised by Wolfgang Bangerth (Texas A&M University, ASPECT main developer), Stephan Sobolev (GFZ Potsdam), Bernhard Steinberger (GFZ Potsdam).

Contents

Session II.

Tectonics and Surface Processes

Session Description: Tectonics and Surface Processes

Conveners: Fabien Graveleau (U Lille), Niels Hovius (GFZ/U Potsdam)

Interactions between tectonics and surface processes are a primary control on the dynamics of topography, deformation of the lithosphere and the evolution of sedimentary basins. Due to this link, landforms contain information about tectonic processes, basins about the development of surrounding topography, and lithospheric structures about the history of Earth's surface. To read this information, and to resolve with it processes that happen elsewhere in this coupled system is an outstanding challenge in the Geosciences. Different approaches must come together to address this challenge. Geomorphic, geological, sedimentological and geophysical observations can describe past or present manifestations of the system, but such observations do not necessarily resolve the nature of the processes that link between tectonics and surface processes, and their characteristic scales. Numerical and analogue modelling can fill this gap with simplifications and abstractions of the essential physics of the system, yielding predictions that can be tested against the geological reality. To this session, we warmly welcome works that develop both approaches, as well as innovative contributions addressing technical and theoretical challenges in modelling of the interactions between tectonics and surface processes.

Neotectonic evolution of the El Salvador Fault Zone. Insights from 4D analogue experiments.

J. Alonso-Henar[1,2], G. Schreurs[3], J.J. Martínez-Díaz[1,4], J.A. Álvarez-Gómez[5]

[1]*Department of Geodynamics, Faculty of Geology, Universidad Complutense Madrid. Spain*
[2]*CEI Campus Moncloa, UCM-UPM, Madrid, Spain.*
[3]*Institute of Geological Sciences, University of Bern, Bern, Switzerland*
[4]*Instituto de Geociencias IGEO (UCM,CSIC), Madrid, Spain*
[5]*GNS Science, New Zeland*
e-mail: *jahenar@geo.ucm.es*
session: *Tectonics and Surface Processes*

Introduction

The El Salvador Fault Zone (ESFZ) is an active, c. 150 km long and 20 km wide segmented, dextral strike-slip fault zone within the El Salvador Volcanic Arc striking N90° -100° E (figure 1) (Martinez-Diaz et al., 2004). Although several studies have investigated the surface expression of the ESFZ, little is known about its structure at depth and its kinematic evolution. Structural field data and remote sensing images reveal a trenchward migration of the volcanic arc. Some evidences suggest that not all structures within the ESFZ can be explained with the current tectonic context, but require a phase of extension or an extensional component of deformation at some stage in the evolution of the ESFZ. Such extension and migration of the volcanic arc could be related to a subduction roll-back of the Cocos Plate beneath the Chortis Block in Mio-Pliocene times.

We carried out 4D analogue model experiments to test whether or not an early extensional phase is required to form the present-day fstructure of the ESFZ. We have carried out different experiments combining transtensional, strike-slip and extensional settings in different ways and with different geometries of a weak zone related to the current position of the volcanic arc (table 1 and figure 1 B). The deformation was imaged with X-ray computed tomopgraphy. All the experimental process has been carried out in the Experimental Tectonic Laboratory of the Institute of Geological Sciences of the University of Bern and in the CT Scan room of the Institute of Forensic Medicine of the University of Bern. Some of the experiments were analyzed with a X ray Scan Tomography as a non-destructive way that allows us to see the 3D structure during the evolution of the experiment (Colleta et al., 1991).

Results

The results of the models that better mimics the geometry of ESFZ are the models 443 and 448 (figures 2 and 3). Both models include an extensional phase that create several independent grabens along the discontinuous weak zone. During a second deformation phase (simple shear in model 443 and transtension in model 448), all the grabens are connected and inter-graben areas with more diffuse deformation appear. In the experiment 443, the stages 2 and 3 in the Figure 2 are the closest to the geometry of ESFZ In the experiment 448, the stage 2 also reproduce geometries similar to ESFZ.

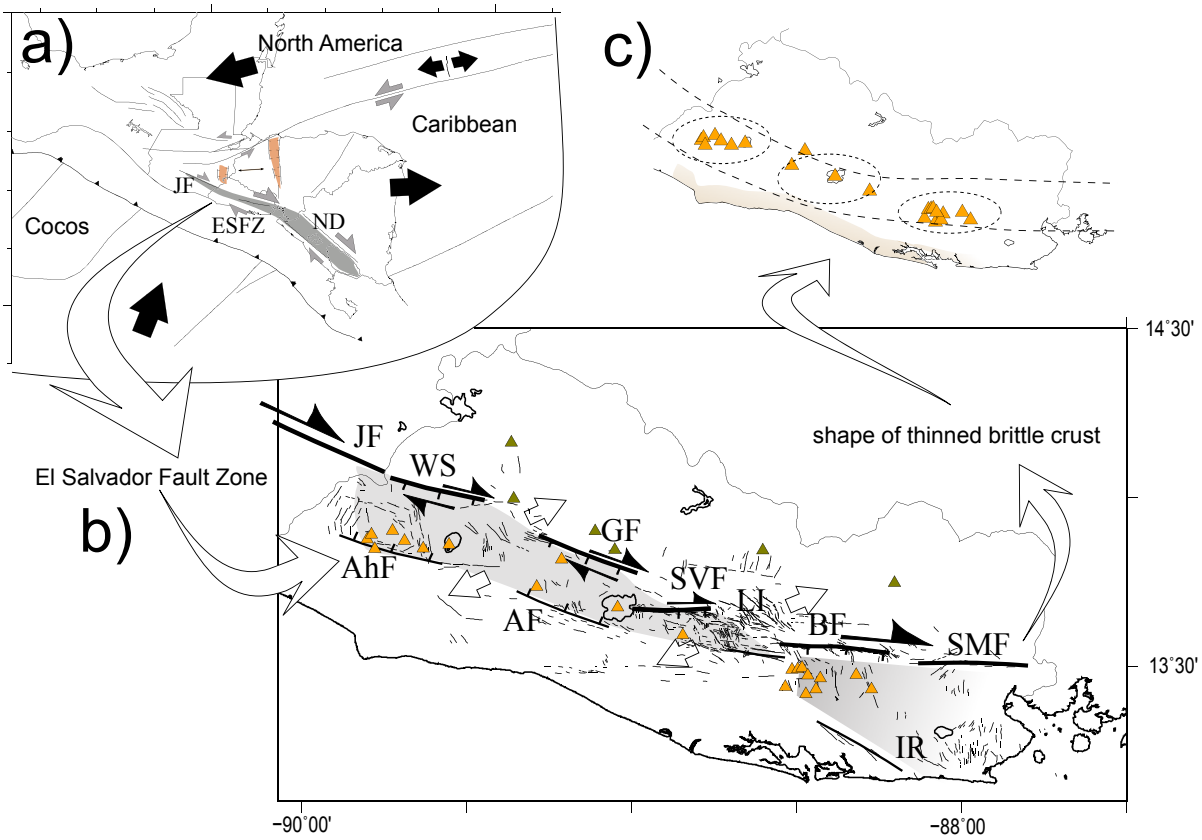

Fig. 1.: A: Tectonic setting of northern Central America. Orange triangles show the positions of volcanoes in the Central America Volcanic Arc. Abbreviations are: PF: Polochic Fault; MF Motagua Fault; JF: Jalpatagua Fault; ESFZ: El Salvador Fault Zone; HE: Hess Scarp. B: Synoptic sketch of the geometry of the continuous and discontinuous weak zone used in the experimental procedure. C: Main structures of the El Salvador Fault Zone. Green triangles are Miocene Volcanoes, orange triangles are Pleistocene Volcanoes. Upper right corner: JF: Jalpatagua Fault; WS: Western segment; AhF: Ahuachapan Fault; GF: Guaycume Fault; AF: Apaneca Fault; SVF: San Vicente Fault; LI: Lempa Intersegment Zone; BF: Berlin Fault; SMF: San Miguel Fault; IR: Intipucá Range. Faults from Canora et al., 2010 and 2012.

Discussion and conclusions

Our experiments suggest that a two-phase tectonic evolution explain better the ESFZ structure: an early pure extensional phase linked to a segmented volcanic arc is necessary to form the main structures of the ESFZ and can explain the shallow geometry of the fault zone. This extensional phase is followed by a strike-slip dominated regime, which results in inter-segment areas with local transtension and segments with almost pure strike-slip motion. The previous extensional phase could be related with a subduction roll-back of the Cocos Plate beneath the Chortís Block. This roll-back could heat in a non-homogeneous way the upper crust. Large magma chambers along the volcanic arc control the formation of grabens along the CAVA crossing El Salvador. Once the roll-back ceased, the structures generated during the first phase where reactived as strike-slip faults. Between the main strike slip faults intersegment zones would be developed with distributed deformation and local transtension areas. Pull-apart basins and releasing bends would also be created (figures 2 and 3).

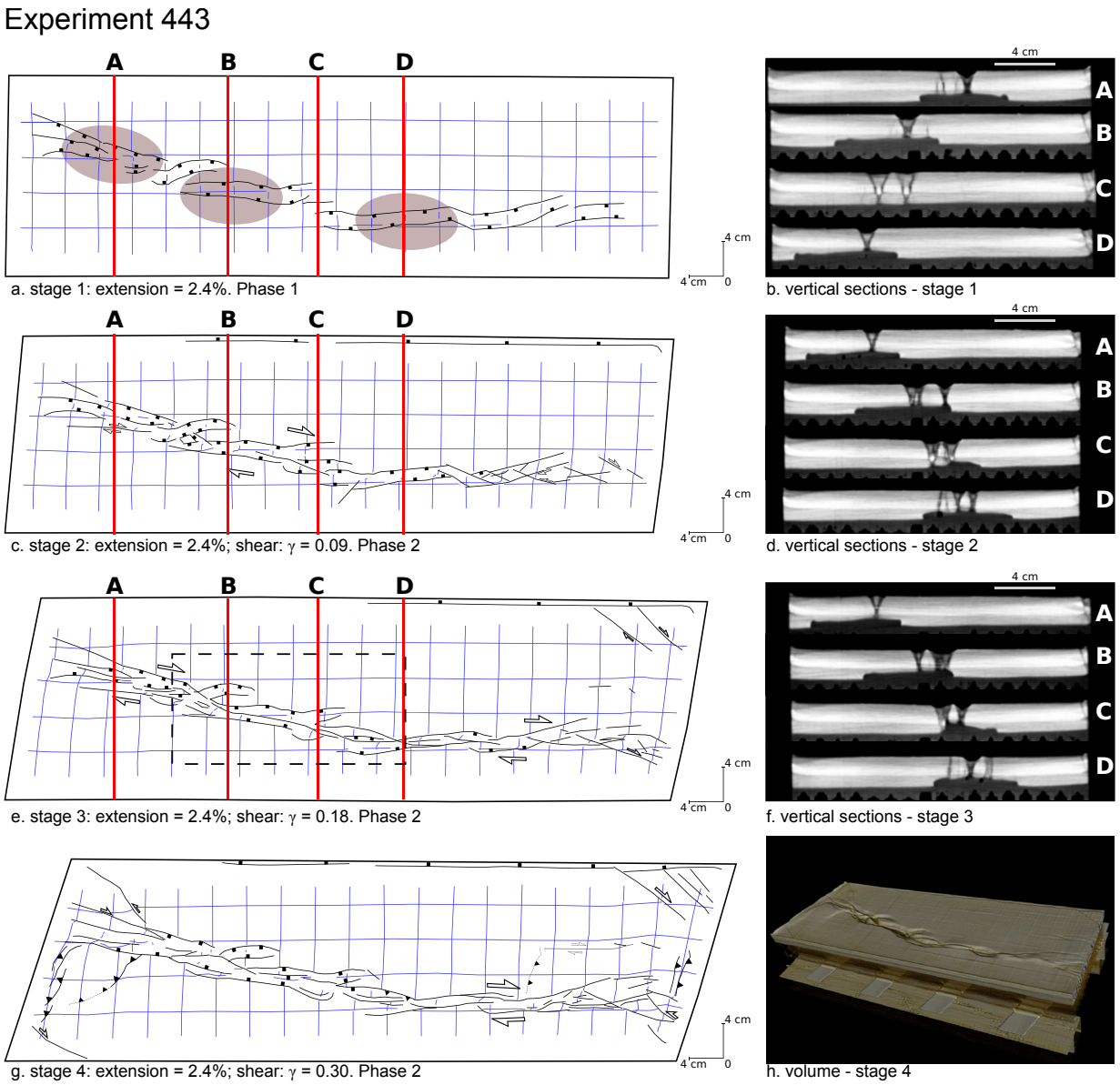

Fig. 2.: Experiment 443, extension followed by pure strike-slip, running over a discontinuous weak zone. Vertical sections and volume from the CT Scan.

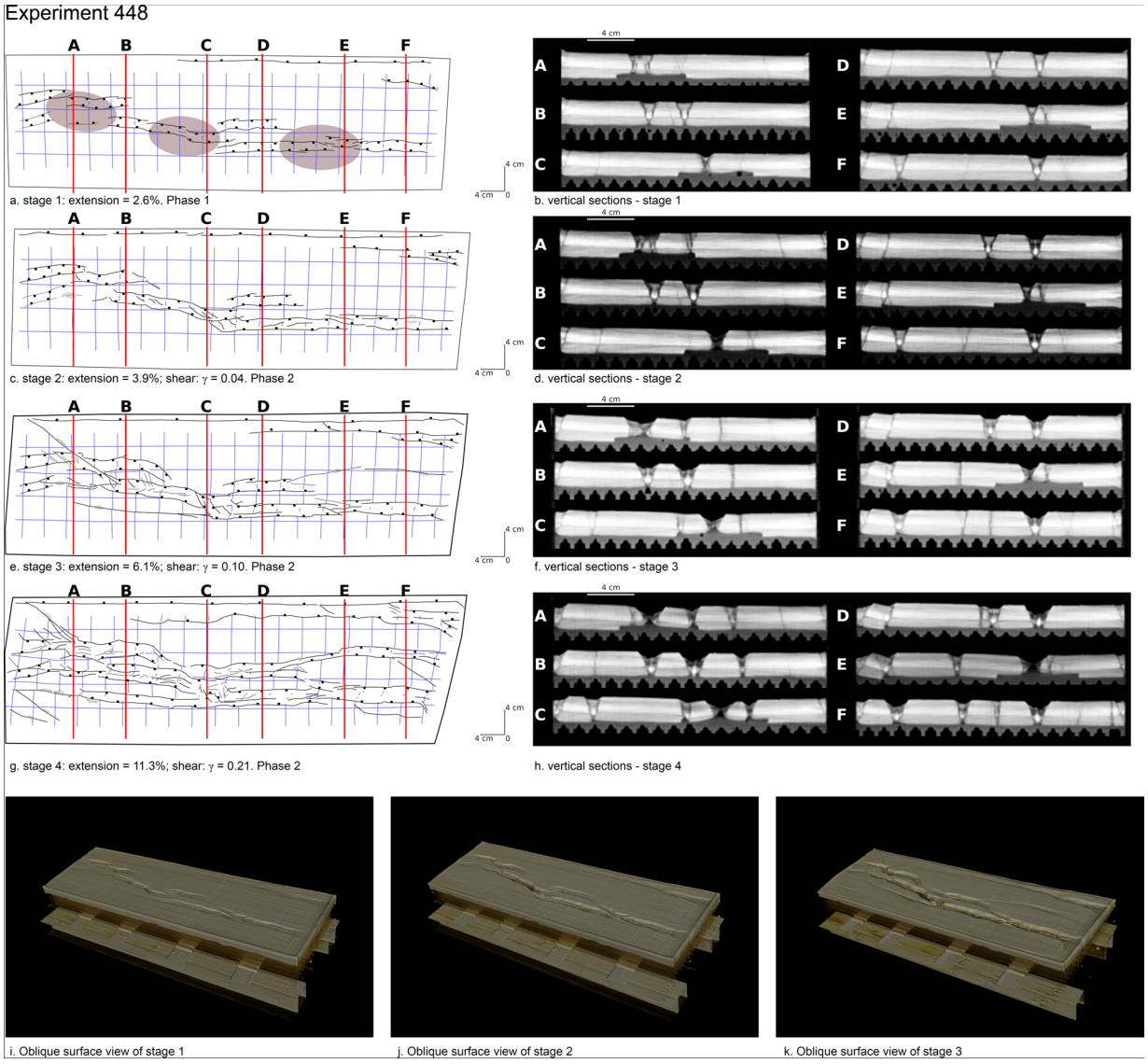

Fig. 3.: Experiment 448, Extension followed by transtension running over a discontinuous weak zone. Vertical sections and volumes from the CT Scan.

Tab. 1.

Exp. No.	Kind of weak zone	Kind of kinematic	Original dimensions (mm)	Extension (mm)	Shear (mm)	Ductile layer thickness (cm)	Brittle layer thickness (cm)	Max. Shear strain
435	Continuous	Strike-slip	230 × 786	0	80	0.5	2.5 or 2	0.35
438	Discontinuous	Strike-slip	230 × 786	0	80	0.5	2.5 or 2	0.35
443	Discontinuous	Extension + Strike-slip	230 × 786	5,5	70	0.5	2.5 or 2	0.3
444	Continuous	Extension + Strike-slip	230 × 786	8	51	0.5	2.5 or 2	0.21
445	Discontinuous	Transtension	230 × 786	22	54	0.5	2.5 or 2	0.21
446	Continuous	Transtension	230 × 786	22	54	0.5	2.5 or 2	0.21
447	Continuous	Extension + Transtension	23 × 80	28	49	0.5	2.5 or 2	0.19
448	Discontinuous	Extension + Transtension	23 × 80	26	49	0.5	2.5 or 2	0.19

References

Canora, C., Martínez-Díaz, J.J., Villamor, P., Berryman, K., Álvarez-Gómez, J.A., Pullinger, C., Capote, R., 2010. Geological and seismological analysis of the Mw 6.6 13th February 2001 El Salvador earthquake: Evidence for surface rupture and implications for seismic hazard. Bulletin of the Seismological Society of America 100 (6), 2873- 2890.

Canora, C., Villamor, P., Martínez-Díaz, J.J., Berryman, K., Álvarez-Gómez, J.A., Capote, R., Hernández, W., 2012. Paleoseismic analisys of the San Vicente segment of the El Salvador Fault Zone, El Salvador, Central America. Geologica Acta 10, 103-123.

Colleta, B. , Bale, P., Ballard, J.F., Letouzey, J., And Pinedo, R., 1991. Cumputed X-ray tomography analysis of sandbox models: Examples of thin-skined thrust systems: Geology, v. 19, p. 1063-1067.

Martinez-Diaz, J., Alvarez-Gomez, J., Benito, B., and Hernandez, D., 2004. Triggering of destructive earthquakes in el salvador. Geology 32(1), 65-68.

Schreurs, G., 2003. Fault development and interaction in distributed strike-slip shear zones: an experimental approach. In: Storti, F., Holdsworth, R.E., Salvini, F. (Eds.), Intraplate Strike-slip Deformation Belts. Geological Society, London, Special Publications 210, 35–52.

Restraining and releasing bands along a sinistral strike-slip shear zone: A physical modeling approach

Blanco, A.[1], Alves da Silva, F.C.[2]

[1]*Programa de Pós-Graduação em Geodinâmica e Geofísica (PPGG), Universidade Federal do Rio Grande do Norte – UFRN*
[2]*Departamento de Geologia - Universidade Federal do Rio Grande do Norte – UFRN*
e-mail: *ablanco@sapo.pt*
session: *Tectonics and Surface Processes*

Introduction

Modeling has become a powerful tool to reproduce geological structures in diverse tectonic environments. Strike-slip faults and associated pull-apart basin modeling appear in many papers in the literature. In this work, we modeled a sinistral strike-slip fault and associated releasing and restraining bends, and explore the nucleation and development of thrusts, normal fault, as well as their relationship with the principal deformation zone represented by strike-slip fault.

Modeling methods

In the experiments described here, we used only quartz sand from dunes. Narrow layer of artificially painted sand was intercalated into natural color sand pack as markers of the deformation (total pack width is 3cm). The sand box dimensions were 50×35×20 cm (l × w × h), with three fixed walls and a mobile one (figure 1). The motor-controlled speed of the mobile wall was 0,42 mm/s. The velocity discontinuity, in the bottom of the box, is represented by a paperboard, attached to the moving wall, which geometry stimulates the development of contractional and extensional sites at the edges of a transcurrent segment (anticlockwise displaced) (figure 1).

The experiments, reproduced several times, were registered both by conventional photos and by PIV (Particle Image Velocimetry). Distension was about 6 cm and the final stage cut in slices, each of which with 0,5 cm, enabling the analysis of the structures in the subsurface. An arbitrary North was created only to facilitate the reference of the formed structures. The strike of the transcurrent fault was settled north-south.

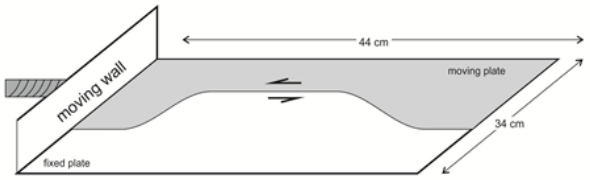

Fig. 1.: Line drawing of the basal portion of the sand box illustrating the geometry of the velocity discontinuity.

Models results

Three distinct sites of deformation were developed in the models involving normal, reverse and strike-slip faults. In the south, the contraction induced the nucleation of oblique NE-SW trending reverse faults characteristic of restraining bends (figure 2a). The southward propagation of the transcurrent segment led to the development of NW-SE back thrusts. In surface, this region marks a topographic high in the top of which some small extensional structures could form. In subsurface a positive flower geometry is recorded (figure 2b).

The northern extremity of the model shows

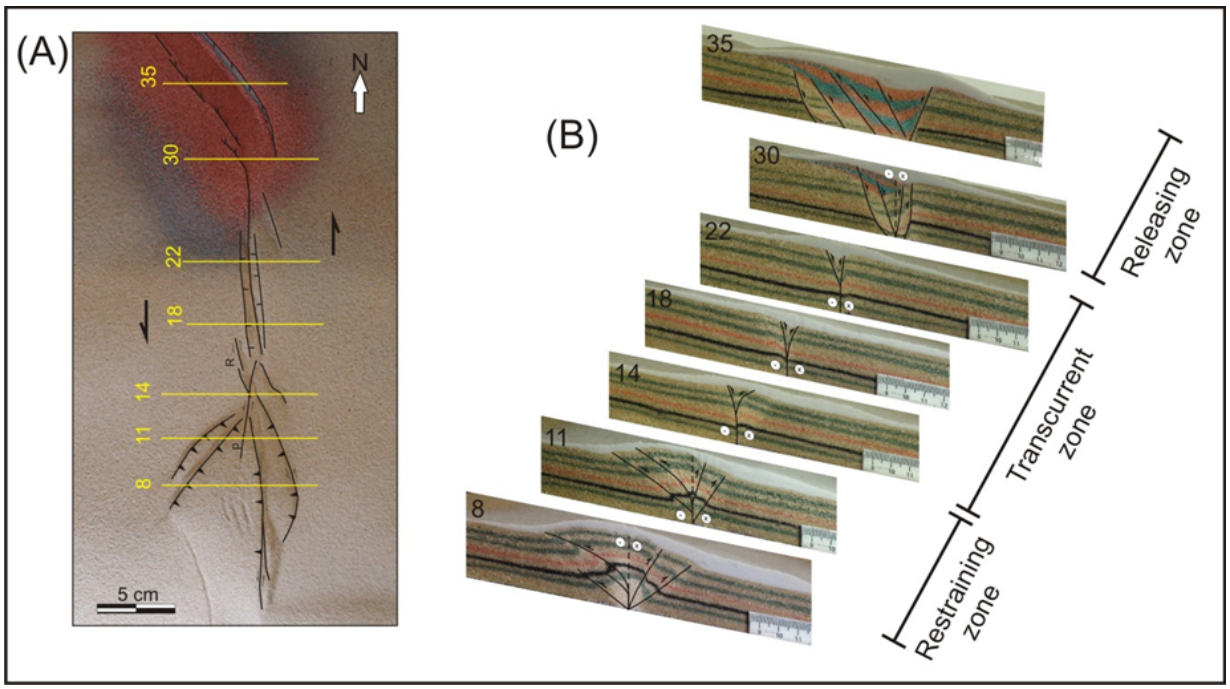

Fig. 2.: (A) Surface of the experiment at its final stage of deformation (displacement of 6 cm). The main structures are drawn and the sections locations are marked; (B) Interpreted sections displaying the geometry of the structures in subsurface. Notice the positive flower (pop-up like structure) formed in the restraining bend and the basin developed at the releasing bend.

NW-SE trending normal faults that originated an oblique basin characteristic of releasing bends (figure 2a). The sections 30 and 35 (figure 2b, see location in figure 2a) reveal a steep dipping master fault in the eastern and several less inclined antithetic faults in the western side. At least in the SE extremity of the basin, in the interface between normal faults and the strike-slip segment, a negative flower like-structure was developed (figure 2b, section 30). During the deformation, the north board fault became inactive while a sequence of antithetic faults progressively developed toward SE consequently widening the basin. Figure 3 shows the strain and the geometry of the basin on surface. In figure 3a, we verify that the progress of the strike-slip fault into the basin led to the development of a new normal fault to the SE and the earlier formed one became inactive.

The sinistral strike-slip fault is better marked in the central part of the model, connecting the restraining and releasing bends. In the very early stage of its development, R shears nucleated along with Y shear. The initial stage of these structures is not visible at naked eye, so it was recorded by PIV (figure 4a). In the restraining bend, one R segment became important prior the development of the reverse faults (figure 4b). With the ongoing deformation, the strike-slip segment along with the NE-SW trending thrust became dominant and R segment turns into NW-SE trending back thrust (figures 4c, d). Then in the restraining bend, a positive flower developed, as shown in figure 2b (sections 8 and 11).

Final remarks

The experiments showed the nucleation of R and Y shear very early (0,5cm of displacement) in the strike-slip fault. There is an important interaction between the transcurrent segment and the restraining and releasing bend's faults. In the restraining site, the transcurrent fault develops in between forward and backward thrusts (these

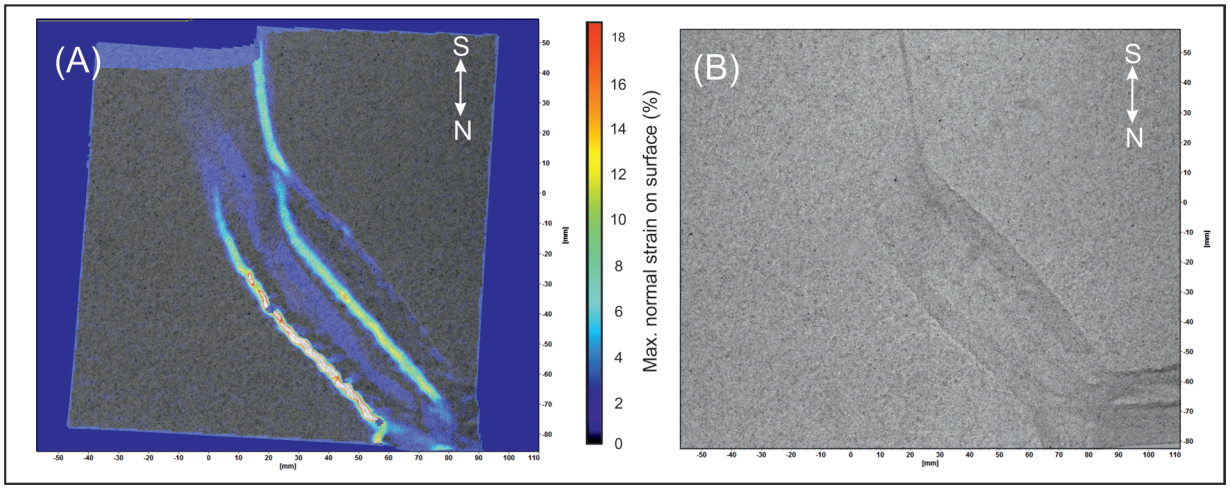

Fig. 3.: (A) PIV picture showing the maximal strain in surface. Note a small segment of strike-slip fault connected with a normal fault approximately in the middle of the basin. The board fault attenuated once deformation progress southward. (B) Conventional photo depicting the basin geometry. In the SE extremity, sand collapsed into the basin covering part of the faults.

later nucleated initially as R shear), forming positive flower. When advancing into the oblique basin, in the realizing bend, the interaction with normal faults led to negative flower formation. At surface, restraining and releasing area are marked by positive and negative topography, respectively (figure 5).

During the experiments, the movement along the strike-slip fault was intended to be pure transcurrence, but once only one plate moved relative to the other, the 0,2 mm thick paperboard used as velocity discontinuity provoked a slight opening along the strike-slip, resulting in a transtensional component.

Acknowledgements

Blanco A. thanks the Brazilian ANP (Agência Nacional do Petróleo) for his PhD scholarship. The Laboratório de Modelagem Estrutural da UFRN is sponsored by Rede de Geotectônica of CENPES/PETROBRAS.

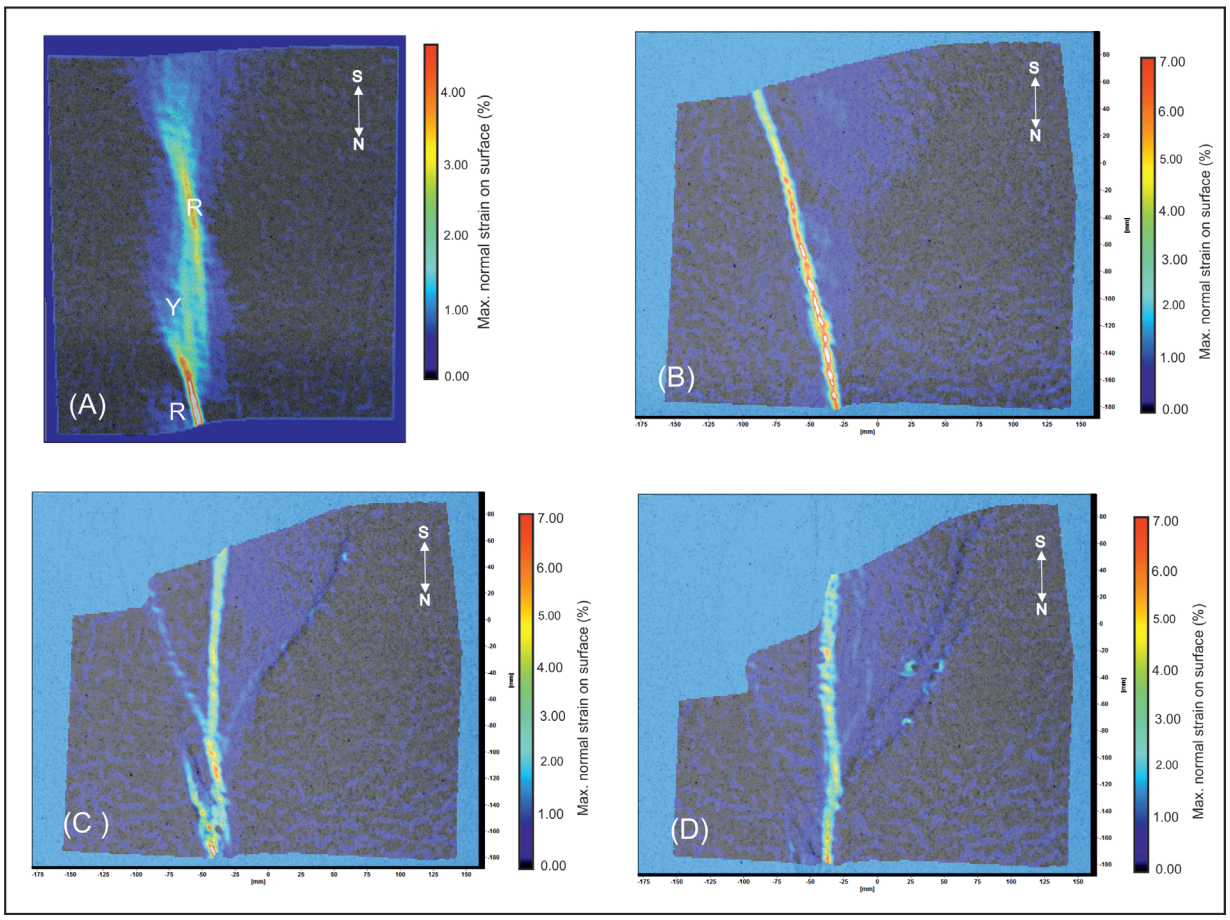

Fig. 4.: PIV picture depicting the maximal strain on surface. (A) Earlier stage of deformation with the development of R and Y shear; (B) R shear in the restraining bend; (C) (D) development of the strike-slip segment in between thrusts and back-thrusts faults

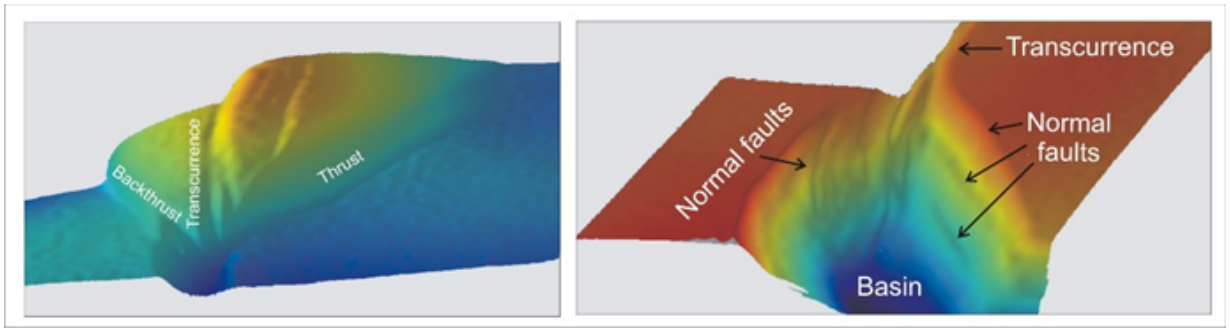

Fig. 5.: 3D model of the restraining and releasing beds, respectively.

Numerical basin modelling of a salt rim syncline: insights into rim syncline evolution and salt diapirism

Christian Brandes[1], Jutta Winsemann[1]

[1]*Institut für Geologie, Leibniz Universität Hannover, Callinstraße, 30167 Hannover, Germany*
e-mail: *brandes@geowi.uni-hannover.de*
session: *Tectonics and Surface Processes*

Salt rim synclines are directly linked to salt diapirs and their sedimentary filling is the key for understanding the temporal and spatial evolution of the respective diapir. Furthermore, the development of rim synclines is a driving mechanism for down-building. The load of the adjacent rim syncline causes lateral salt flow from the source layer into the diapir.

This study deals with rim syncline and salt wall development in northern Germany. With up to 300 salt structures, the North German Basin is a perfect natural laboratory for studying salt-dominated basins. The analysed rim syncline is called Schöningen rim syncline and developed along the flank of the Helmstedt-Staßfurt salt wall in northern Germany. The entire salt wall is 70 km long and trends NW-SE. Including the rim synclines on both sides, the complete structure is 6 to 10 km wide.

Basis for the study are exploration wells that were drilled by the Braunschweigische Kohlen-Bergwerke (BKB, now E.ON Kraftwerke GmbH) over five decades. Altogether, 357 wells were used to construct a 3D subsurface model. The subsurface modeling was performed with the software package GOCAD®and the model covers an area of 32 km^2. The basin modelling part of this study was carried out with the software PetroMod®2D, which was developed by the Schlumberger Aachen Technology Center (AaTC), IES GmbH, Germany. PetroModâ is a software that simulates and analyses the burial history and temperature evolution of a sedimentary basin. It is a dynamic forward simulation based on the finite element method.

The Schöningen rim syncline is 8 km long and 3 km wide. The basin-fill is up to 366 m thick and characterized by 13 more or less continuous lignite seams with thicknesses between 0.1 and 30 m. The coal-bearing succession is subdivided into the early Eocene Lower Seam Group (LSG) and the Middle Eocene Upper Seam Group (USG). The clastic units in the syncline include seven depositional stages: (1) tidally influenced fluvial estuarine channel deposits; (2) mixed tide- and wave- dominated estuarine deposits; (3) prograding wave dominate delta deposits; (4) transgressive shoreline deposits; (5) braided fluvial channel deposits; (6) estuarine deposits; and (7) prograding tide-dominated channel deposits. The succession defines four 3rd order sequences and several higher order sequences that are possibly related to Milankovitch cycles (Osman et al., 2013).

Based on the well data, the basin-fill architecture of the rim syncline was reconstructed in 3D. The basin axis runs parallel to the trend of the salt wall. Several cross-sections perpendicular to the basin axis indicate that the basin-fill has a very pronounced lenticular shape. This shape varies from more symmetric in the NW to clearly asymmetric in the SE, where the steeply dipping beds are close to the salt wall and more gently dipping units are found along the opposite side of the basin margin. The 3D model displays that the basin-fill of the rim syncline consists of a vertical stack of concave packages, where younger units cover a smaller area than the older ones. The depositional units show a lateral migration towards the NNE.

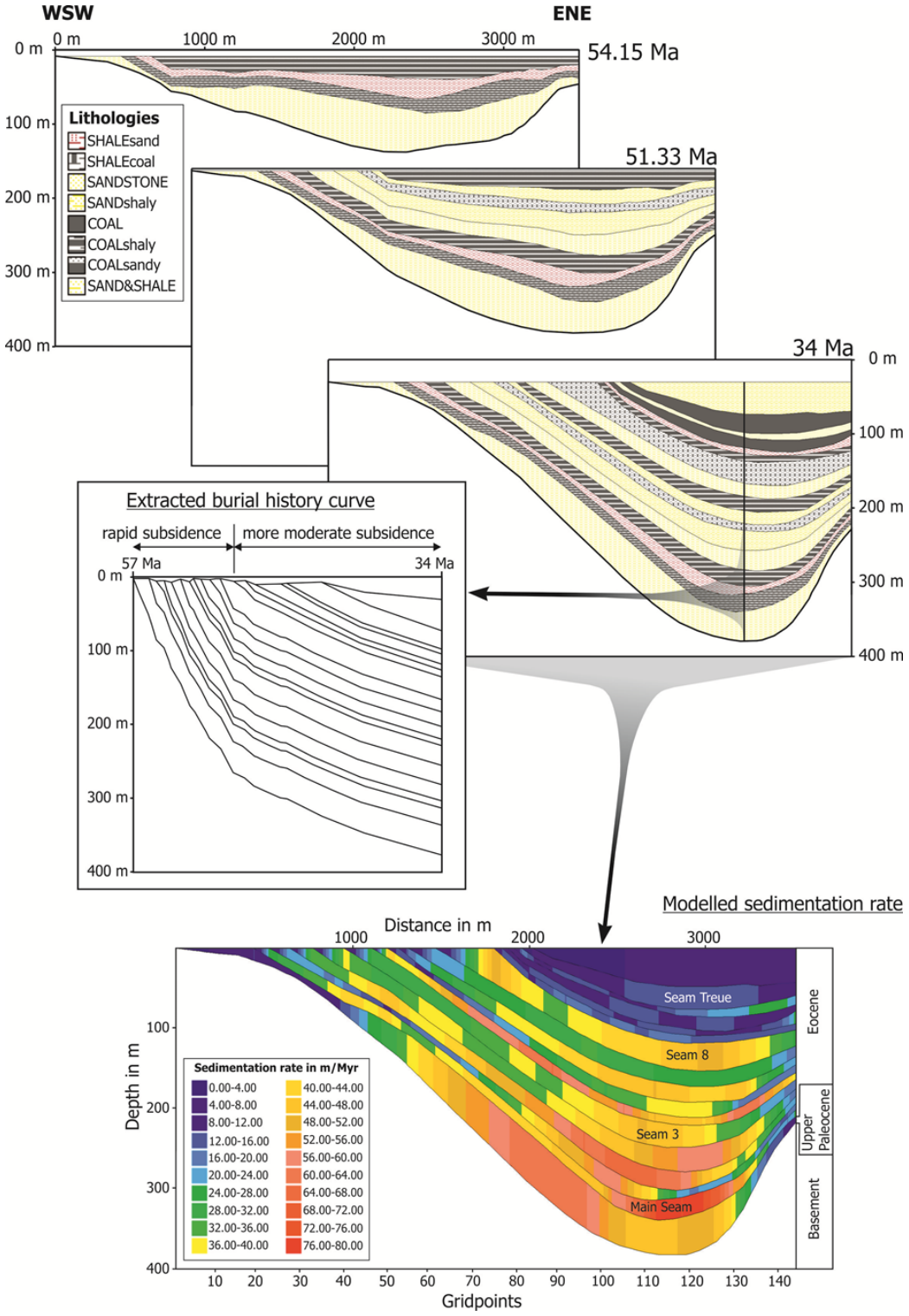

Fig. 1.: Basin modelling results. The simulation shows the progressive migration of the depocentre of the rim syncline towards the salt wall. From the 2D simulation, a burial history curve was extracted, which shows an initial rapid subsidence between 57 and 50 Ma and a more moderate subsidence from 50 to 34 Ma. The highest sedimentation rate of 76 to 80 m/Myr occurred during the deposition of the main seam. During the formation of the Upper Seam Group, the rates were significantly lower with values between 20 to 12 m/Myr (modified after Brandes et al., 2012).

For the basin simulation, a cross-section was extracted from the static 3D subsurface model. This cross-section trends ENE-WSW, is 3.5 km long and runs perpendicular to the basin axis. It is a very suitable cross-section for the basin simulation because there are 16 wells located on the section, which provide lithology and age control. The finite element grid that is used for the 2D simulation has rectangular cells defined by vertical grid lines and horizontal event lines. The horizontal event lines are time lines derived from the geological cross-section. The vertical grid lines are placed at an equal distance along the section to generate a mesh. During the simulation, the finite element grid is fixed to the basin-fill and subsides with the depositional units. The modeling workflow with PetroMod®has been described in detail by Poelchau et al. (1997). The first step for basin simulations is the construction of a conceptual model. This was done on the basis of the 2D cross-section derived from the 3D subsurface model. The geometry of the basin-fill was transferred to PetroMod®and the depositional history of the basin was divided into distinct layers. Absolute ages and lithologies were assigned to each layer. The lithology controls the behaviour during compaction. The lithology for each depositional layer was derived from the wells. Each lithology is characterized by several physical parameters. Based on the well data, we chose the appropriate lithology for the simulation. The water depth is determined based on fossils, facies and lithology. The conceptual model for the 2D simulation consists of 18 layers, which have been defined on the basis of well data and are characterized by a standardized lithology as provided by the program. The geometry of the individual layers is derived from the 3D subsurface model. For the simulation, a finite element mesh was used with 144 vertical grid lines.

The simulation shows that the present-day asymmetry of the basin-fill, which is characteristic for the southern part of the Schöningen rim syncline, was already developed in the early phases of basin evolution. The maximum subsidence is concentrated close to the salt wall. In addition, the modeling results show a progressive migration of the depocentre of the rim syncline towards the salt wall (Brandes et al., 2012). A similar migration of the depocentre towards the salt wall was observed based on isopach maps derived from the 3D subsurface model. Though the isopach maps are not decompacted they show the same depocentre evolution as the basin simulation. We therefore assume that most of the thickness variations visualized on the isopach maps, represent the subsidence pattern and are not compaction effects.

From the 2D simulations, a geohistory curve was extracted that shows initial rapid subsidence between 57 and 50 Ma and a more moderate subsidence from 50 to 34 Ma. The subsidence of the basin can therefore be subdivided into two distinct phases.

The sedimentation rates were highest in the area of the basin axis. A clear decrease in sedimentation rates through time can be observed. In the early phase of basin evolution, the sedimentation rates were high, with values of 60 – 80 m/Myr during the formation of the Main Seam and Seams 1 and 2. Subsequently, the sedimentation rates decreased to 32 – 56 m/Myr during the formation of Seams 3 to 9. In the final stage of basin evolution, the sedimentation rates were much lower with values of 2 – 20 m/Myr.

The southeastern part of the Schöningen rim syncline has an asymmetric geometry with the deepest part of the basin close to the flank of the diapir. In contrast, the northwestern part, is more symmetric. The geometry of the rim syncline seems to be a function of the diapir morphology. This may be coupled to the well known fact that sediments close to a diapir margin tend to be sheared by the rising diapir (Stewart, 2006), an effect which is probably enhanced where the diapir becomes broader and the related rim syncline is more asymmetric.

The fill of the Schöningen rim syncline consists of a vertical stack of concave depositional units, where the younger units cover a smaller area than the older ones. This implies that the area where deposition took place became constantly smaller over time. It is very likely related to a decrease in subsidence and the migration of the depocentre.

The 2D basin simulation shows the progressive migration of the depocentre towards the flank of the diapir.

The geohistory curve of a rim syncline may reflect salt migration from the source layer into the salt wall. The geohistory curve derived from our basin simulation shows initial rapid subsidence between 57 and 50 Ma and more moderate subsidence from 50 to 34 Ma. It implies that initial salt-withdrawal was rapid but later decreased probably due to depletion of the source layer. Though a salt weld is not developed, this points to a certain depletion of the source layer. Even without the development of a salt weld, the salt flow into the diapir can be significantly reduced. Hudec and Jackson (2007) described that halving the thickness of the salt layer will slow down the flow by a factor of 8. This would explain why the rise of the Helmstedt-Staßfurt salt wall stopped, though there is still salt in the source layer. The highest subsidence rate for the Schöningen rim syncline is 76 - 80 m/Myr during the early phase of basin formation.

Isopach maps derived from the 3D subsurface model indicate that the depocentre evolution is complex and did not take place in a uniform fashion. There is not a simple migration of the depocentre towards the flank of the diapir as the 2D section implies. Depocentres also shifted laterally, parallel to the basin axis. The shifting of the depocentres might be a consequence of non-uniform salt-withdrawal from the source layer and give a first hint of along-strike variations in salt movement.

References

Brandes, C., Pollok, L., Schmidt, C., Wilde, V. and Winsemann, J. (2012) Basin modelling of a lignite-bearing salt rim syncline: insights into rim syncline evolution and salt diapirism in NW Germany. Basin Research, 24, 699-716.

Hudec, M.R. & Jackson, M.P.A. (2007) Terra infirma: Understanding salt tectonics. Earth Science Reviews, 82, 1-28.

Osman, A., Pollok, L., Brandes, C., Winsemann, J. (2013) Sequence stratigraphy of a Paleogene coal-bearing rim syncline: interplay of salt dynamics and sea-level changes, Schöningen, Germany. Basin Reseach, 25, 675-708.

Poelchau, H.S., Baker, D.R., Hantschel, T., Horsfield, B. & Wygrala, B. (1997) Basin simulation and the design of the conceptual model. In: Petroleum and basin evolution (Ed. by D.H. Welte, B. Horsfield & D.R. Baker), pp. 3-70, Springer Verlag.

Stewart, S. (2006) Implications of passive salt diapir kinematics for reservoir segmentation by radial and concentric faults. Marine and Petroleum Geology, 23, 843-853.

Modelling Syntectonic Sedimentation in a Extensional Faults System

Ana Carmona[1], Roger Clavera-Gispert[1], Oscar Gratacós[1], Stuart Hardy[1,2], Josep Anton Muñoz de la Fuente[1]

[1] *GEOMODELS Research Institute, Departament de Geodinàmica i Geofìsica, Universitat de Barcelona, Barcelona, Catalonia, Spain*
[2] *Icrea, Institució Catalana de Recerca i Estudis Avançats, Catalonia, Spain*
e-mail: *anacarmona@ub.edu*
session: *Tectonics and Surface Processes*

Introduction

Relay ramps and transfer fault zones are typical in extensional environments. These structures play a significant role in sediment dispersal as they control the sedimentary pathways. Unlike for subaerial settings, the impact of subaqueous relay ramps on sediment dispersal, clastic sedimentation or carbonate deposits evolution, is less studied. In these subaqueous cases, numerical approximations could be a good approach to understand the syntectonic sedimentation.

Considering this, a numerical model is used to study the sedimentary infill in an extensional basin and specifically related to a relay ramp system. The main aim of this contribution is to show the potential of the syntectonic sedimentation program to analyse these extensional systems. In this contribution, initial results are presented together with an analysis of the treated configuration.

The program

The program uses a novel approach that combines a discrete element model (DEM) (Finch et al., 2004; Hardy and Finch, 2006) and a process based sedimentary model, the SIMAFADIM-CLASTIC program (Gratacós et al., 2009), to link both processes, deformation and sedimentation, in a single model (Carmona et al., 2010). It provides information in many useful different ways, no just the resulting topography to combine sedimentation plus deformation, it also gives detailed information about the deposition and facies distribution as well as the evolution of this new strata with the deformation, therefore the resulting structure. It also allows the study of the evolution of the deformation into the pre and syntectonic materials, so the affection of these new material in the evolving structure.

The program can simulate different extensional environments, e.g., movement of one or two faults (overlapped -relay ramp- or not) in different scales (since cm to km). For one particular configuration it allows playing with different parameters, as positions and movement rates of the faults, and the overlap distance and separation distance in the case of a two faults system (figure 1). The sedimentary model also allows different boundary conditions, as the number of clastic sediments, the sedimentation and transportation parameters that characterize each sediment type (density, settle rate, critical velocity for deposition), the inflowing water and sediment source points and the proportion for each sediment type.

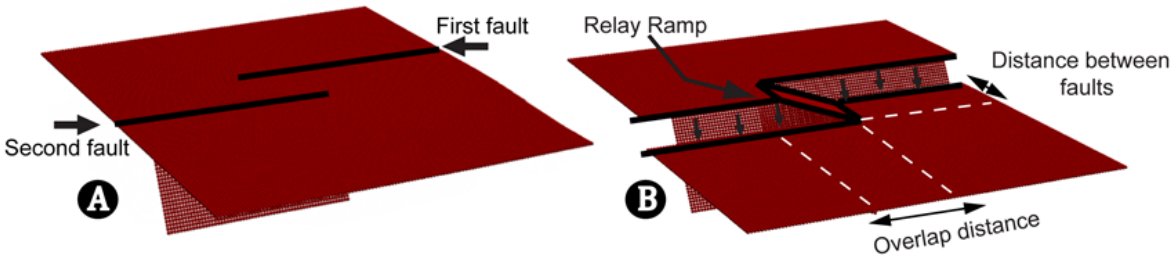

Fig. 1.: Boundary box base of the DE model for the two overlapped extensional faults configuration at the beginning of the simulation (A) and in the final stage (B).

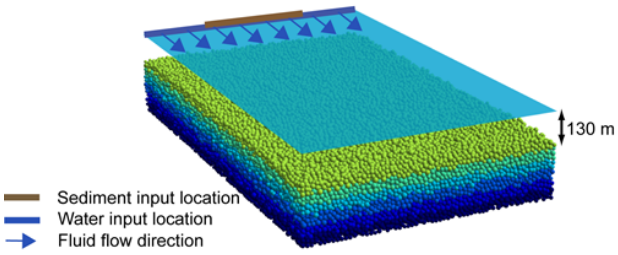

Fig. 2.: Initial and boundary conditions for the sedimentation model.

Initial configuration

In this example, the DEM assemblage has a size of 2,000 m × 1,500 m × 300 m and consists of 111,132 spheres of four different radii: 12.5, 11.25, and 10.0, 8.75 m. Two faults are defined in the DE boundaries (figure 1) with an overlap distance of 500 m and distance between the two faults of 375 m. Total displacement along the faults plane is 200 m. Simulated time is 3,060 years.

A finite element mesh of 300 nodes for the Simsafadim-Clastic program is located above the assemblage surface. An initial bathymetry of 130 m is defined in the basin. Sealevel is constant during the evolution of the model, so changes in bathymetry will be consequence of sedimentation and deformation. Two clastic sediments are defined in the model. The inflowing water and sediment points are defined as is shown in figure 2.

First preliminary results and discussion

To analyse the evolution of the model figure 3 shows four representative time steps of the DEM. It can be appreciated the displacement of the faults (FD) and the new sediments added by the sedimentary model. In each time step, it is worthy to note an asymmetric deposition pattern for the syntectonic sediment due to the fault configuration. It can also be observed how sedimentation migrates basinwards and it takes place mainly in the region where subsidence is more relevant since more accommodation space is available.

To have a look to the final results the model has been divided in seven cross-sections, four longitudinal and three transversal (figure 4). The pretectonic materials have been represented in blue just to have a better view of the new deposited materials. Analysing the sytectonic sediments, growth strata can be observed in both relay ramp and basinward directions (see longitudinal and transversal sections in figure 4).

Syntectonic sediments shows different geometries into the basin related to the fault position and its influence over the accommodation space. In the overlapping area (figure 4 B) the pretectonic surface slope is lower than the surrounding parts (figures 4 A and 4 C) with only one fault and consequently a steeper pretectonic surface slope. So the thickness of the new materials over the overlap area increases slower basinward than in the rest of the model, where the deformation area is smaller and the jump between the footwall

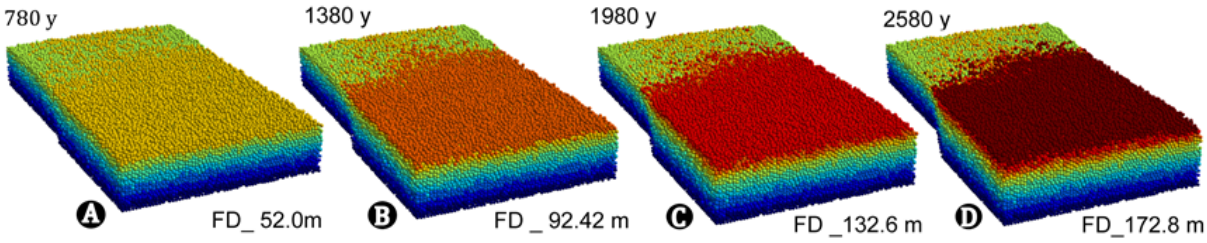

Fig. 3.: Evolution of the DE element model represented by four different time steps. In yellow and reddish colours are represented the new DE added by the sedimentation model.

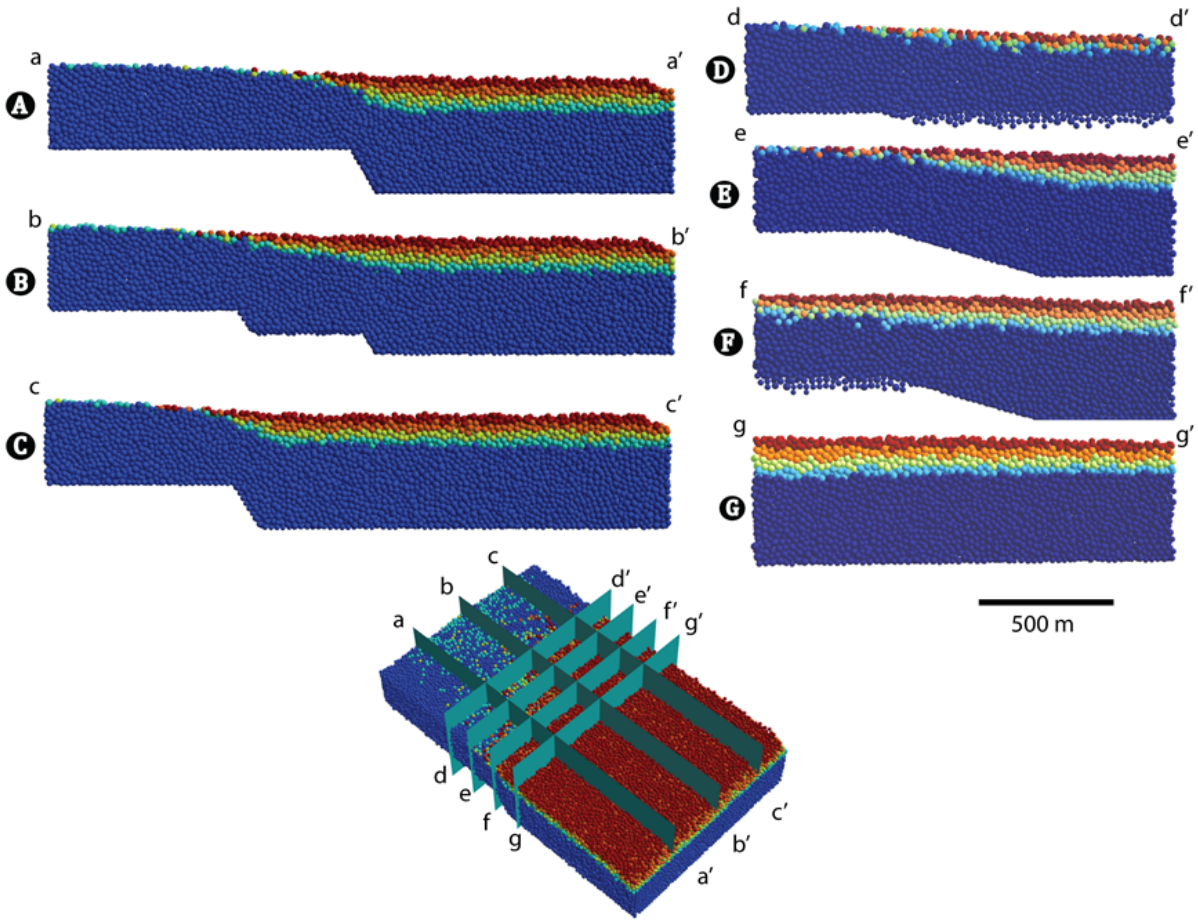

Fig. 4.: Cross-sections of the final stage of the DE model, three transversal, A, B and C; and four longitudinal D, E, F and G. The pretectonic materials are represented in deep blue for a better visualization of the syntectonic materials.

and the hangingwall areas is steeper.

In figure 5, there are represented the evolution of the fluid flow and the thickness of each clastic sediment type in the same four time steps. Regarding to the fluid flow, an asymmetric values and a velocity increase over the time can be appreciated.

Looking to the sedimentation of both materials we can observe again the asymmetric pattern of deposition due to the position of the two faults. Coarse materials settle in the whole basin, proximal and distal areas, obviously taken more relevance in distal parts where more accommodation space is created. As the model moves forward the deposition of the coarse material is concentrated just in the distal area.

On the other hand, fine material sedimentation just takes place in distal regions where the fluid flow is lower and allows its deposition. The sedimentation of the fine materials is prograding basin forward and its thickness decreases in each time step.

Also, we can appreciate that, for both materials, sedimentation is slightly higher in the subsidence area near the second fault. This is probably due to the fact that the bypass, i.e., regions where fluid flow values do not allow significant deposition, is wider in the region that precedes the second fault, so that the amount of sediment in suspension that arrive to this subsidence area is higher.

Conclusions

The results show that the program is a good tool to analyse the change of sedimentation patterns with the evolution of the deformation.

The example presented showed that the evolution of the sedimentation is consistent with the position and movement of the two faults.

Future work should analyse the same initial configuration used in this example but with different boundary conditions, in order to better understand subaquatic extensional systems with relay ramps

References

Carmona A, Clavera-Gispert R, Gratacós O, Hardy S (2010) Modelling syntectonic sedimentation: Combining a discrete element model of tectonic deformation and a process-based sedimentary model in 3D. Mathematical Geosciences 42(5): 519–534

Finch E and Hardy S, Gawthorpe R (2004) Discrete element modelling of extensional fault propagation folding above rigid basement fault blocks. Basin research 16: 489-506

Gratacós O, Bitzer K, Cabrera L, Roca E (2009) Simsafadim-clastic: A new approach to mathematical 3d forward simulation modelling for terrigenous and carbonate marine sedimentation. Geologica Acta 7(3): 311–322

Hardy S, Finch E (2006) Discrete element modelling of the influence of cover strength on basement involved fault-propagation folding. Tectonophysics 415:225–238

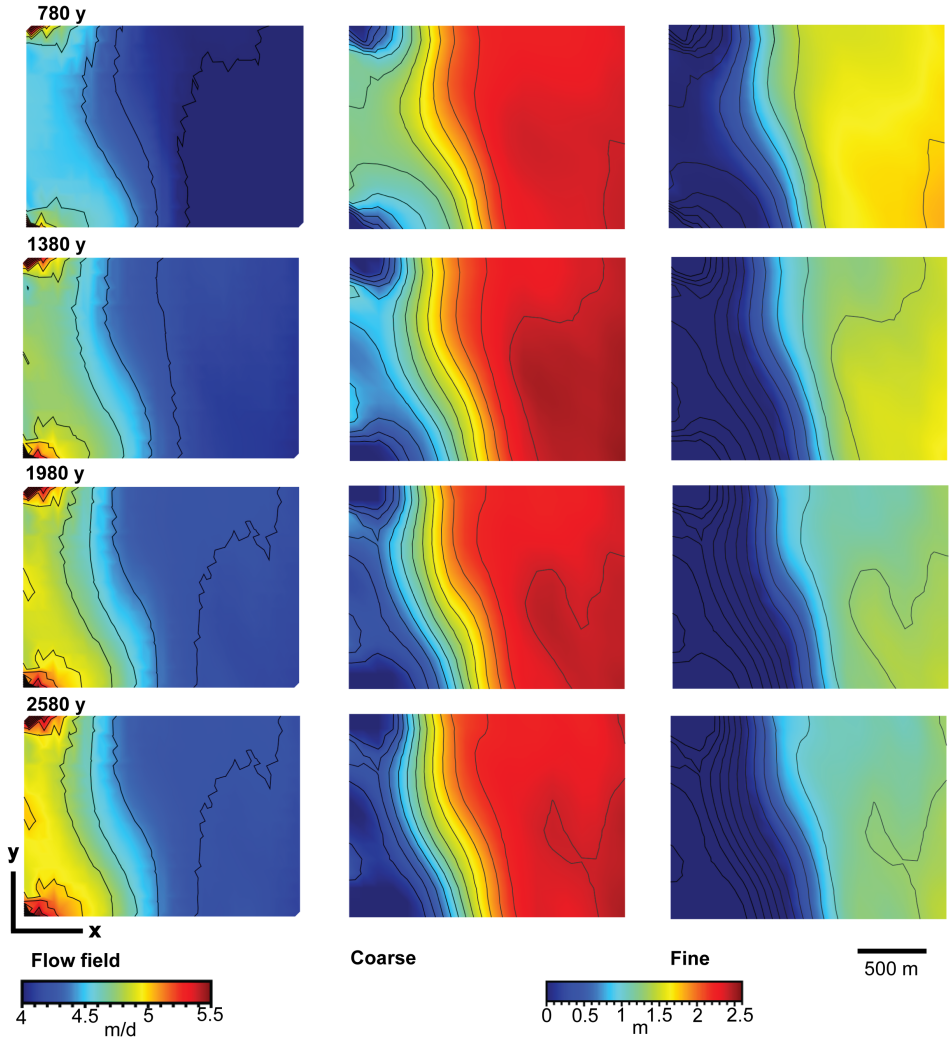

Fig. 5.: Evolution of the fluid flow (m/y), and deposition (in m) of each material, coarse and finer in four different time steps

Process-Based Forward Numerical Modelling SIMSAFADIM-CLASTIC: The Vilomara Composite Sequence case (Eocene, Ebro basin, NE Iberian Peninsula).

Roger Clavera-Gispert[1,2], Oscar Gratacós[1,3], Miguel López-Blanco[1,4], Raimon Tolosana-Delgado[5]

[1]*Institut de recerca Geomodels. Universitat de Barcelona. Spain*
[2]*Abteilung Geologie. Universität Bayreuth, Germany*
[3]*Dept. Geodinàmica i Geofísica. Universitat de Barcelona. Spain*
[4]*Dept. Estratigrafia i Paleontologia. Universitat de Barcelona. Spain*
[5]*Dept. of Modelling and Valuation, Helmholtz Institute Freiberg for Resource Technology. Germany*
e-mail: *roger@clavera.cat*
session: *Tectonics and Surface Processes*

Abstract: SIMSAFADIM-CLASTIC is a 3D process-based forward numerical model that simulates the stratigraphic infill and evolution of marine sedimentary basins (Bitzer and Salas, 2001, 2002; Gratacós et al., 2009a, 2009b; Carmona et al., 2010; Clavera et al., 2013). The program is designed to model processes of transport and sedimentation for clastic terrigenous and clastic carbonate sediments. The program, also include the interaction between carbonate producing organisms and clastic sediments in suspension. Considering that, the objective of the program is to model and to represent the spatial and temporal interplay of the generated sedimentary bodies, obtaining realistic depositional architectures in order to reproduce the 3D sediment distribution and the complex heterogeneity present in the sedimentary record.

The model for siliciclastic transport and sedimentation is based on a potential fluid flow. This fluid flow model can establish the general trend of the flow system to determine the sediment transport in the basin over a geological time scale at basin scale (hundred meters to kilometres) with an acceptable computational time. Regarding to the sediment transport, the fluid flow model can determine the movement of solid particles in suspension due to fluid movement processes that include advection, diffusion, and dispersion.

The carbonate production model is based in the generalized equation of Lotka-Volterra ecological modelling. The program takes into account the influence of environmental factors to model the carbonate producing organisms associations (water depth, nutrients, clastic sediment concentration is suspension, fluid flow velocity and bottom slope), and the interaction among them (predation, prey, mutualism, competition...).

Other processes are modelled to generate (or reduce) accommodation space in the marine basin, including sea level variations, compaction, and isostasy.

In order to show the application and possibilities of the code, the Vilomara Composite Sequence (VCS) of Sant Llorenç del Munt (SLM) fan delta complex (Ebro basin, NE Iberian Peninsula) is modelled.

The Bartonian/Priabonian SLM clastic wedge is located on the south-eastern margin of the Ebro foreland basin, adjacent to the Catalan Coastal Ranges. López-Blanco et al. (2000a, 2000b), and Gómez-Paccard et al. (2012) provide an analysis of the tectonosedimentary, tectonogeomorphic and paleoclimatic setting of the Sant Llorenç del

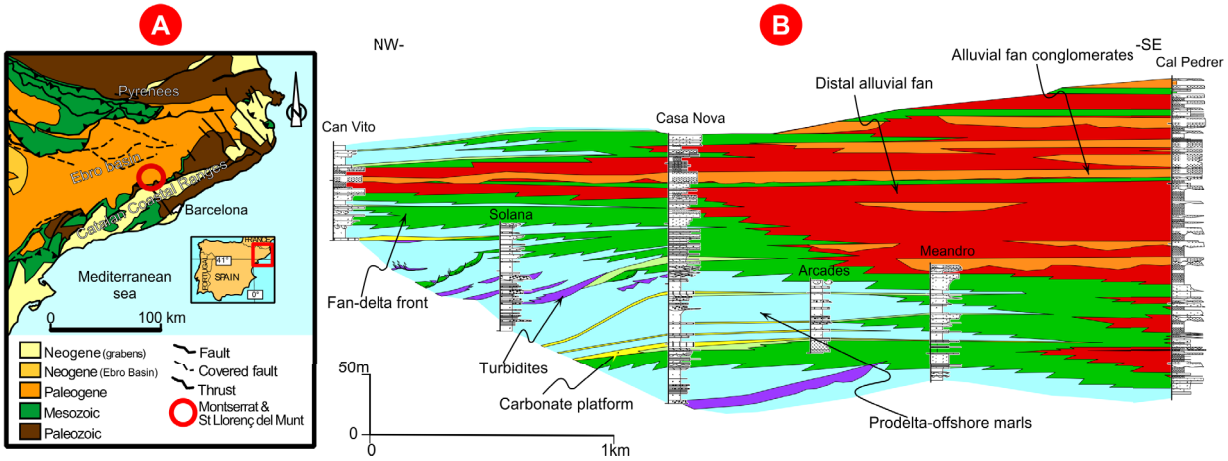

Fig. 1.: Geological and geographic situation of the studied area (A) and the correlation panel of six stratigraphic logs in the western part of Sant Llorenç del Munt system (B) (From López-Blanco et al., 2000b).

Munt complex, as well as an estimate of the rates of geological processes controlling the fan-delta development.

VCS was deposited during the regressive composite sequence set of the transgressive–regressive megasequence of Milany described by the SLM fan-delta complex, and comprises an alternation of detrital sediments interbedded with subordinate carbonate platform deposits. The facies associations in the VCS are from proximal to distal: proximal alluvial fan, distal alluvial fan, fan-delta front, carbonate platform, and fan-delta slope and prodelta.

The VCS is structured into a lower transgressive sequence set (TSS) and an upper regressive sequence set (RSS). This transgressive-regressive trend is built from the piling of seven repetitive, metre-scale transgressive–regressive high-frequency fundamental sequences (Fig.1). These sequences are bounded by maximum regressive surfaces, which correspond to the time of regressive- to-transgressive turnaround of the shoreline, located at the first indication of upward deepening following a regression. These sequences are made up of a transgressive systems tract (TST), overlain by a regressive systems tract (RST), separated by a maximum flooding surface (MFS). They record fluctuations in detrital input, most probably related to a combination of allocyclic (periodic to episodic, relative sea-level changes, tectonic pulses and Milankovitch climatic oscillations) and autocyclic factors (variations in the organization of distributary channels). TSTs develop during periods of low terrigenous input and/or increasing accommodation; RSTs are a response to episodes of high terrigenous input and/or decreasing accommodation space.

Taking into account these previous geological settings, the observed depositional architecture has been interpreted as controlled by fluctuations in the sediment supply rate and changes in accommodation space. The models obtained using SIMSAFADIM-CLASTIC can help us to discuss which of both parameters, fluctuations in the sediment supply rate and/or changes in accommodation space, has great influence on the geometry and on facies distribution.

To show this and considering the observed field data, 3 different configurations have been done considering the variation of key parameters (Fig.2): sediment supply and sea level. Configuration A (Fig.2A) models the influence of variation in sea level, for this reason it varies the sea level as shown in Fig.2 and sediment supply is constant; Configuration B (Fig.2B) models the influence of sediment supply, and this configuration varies sediment supply as shown in Fig.2B and sea level rises linearly (to minimize the affection of it generating the necessary space); and configuration C (Fig.2C) combines sea level and sediment supply

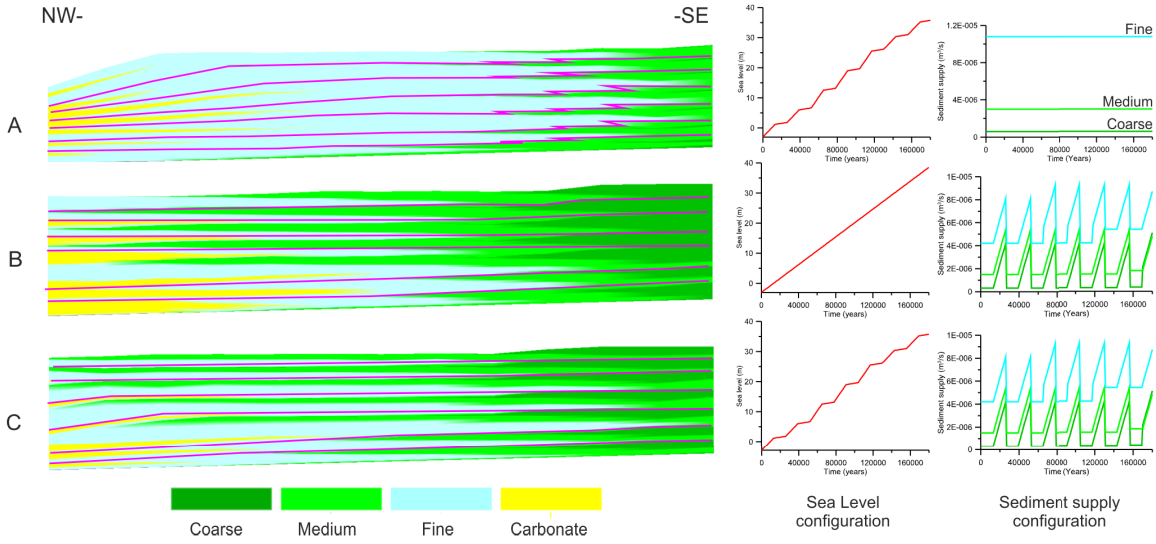

Fig. 2.: Cross-sections and related sea level and sediment supply in each configuration in function of the main affecting parameter defined: A. sea level. B. sediment supply. C. sea level and sediment supply (see text for more explanations).

variations as shown in Fig.3C.

The results for the Configuration A show the carbonate sediments trends to join in the distal part of the basin, and the coarse sediments from fan-delta front does not prograde to the centre of the basin and are located in most proximal part in the SE. This model does not show the internal Transgressive –regressive trend of the VCS.

The Configuration B results show tabular geometry of the sedimentary bodies, the carbonate sediments have been growth from the central part of the basin to the distal parts with a great thickness. The coarse and medium sediments from fan-delta front prograde inside de basin. This configuration shows the internal Transgressive -regressive trend of the VCS.

The Configuration C results show a sigmoidal geometry; the carbonate development is less thick than Configuration B and growth from central part of the basin till distal parts in NW. The coarse and medium sediments of fan-delta front prograde from proximal parts in SE to central part of the basin. This configuration shows the internal Transgressive –regressive trend of the VCS.

From these configurations, Configuration C is the most accurate model and shows a better correlation with the data observed in the field than others configurations, concluding that both, sea level and sediment supply play an important role in the architecture of the depositional system. Even so, Configuration A shows more distant results from observed data; while Configuration B shows better sediment distribution compared with field data, concluding that the sediment supply affects more than accommodation space in the body geometry and sediment distribution.

References

Bitzer, K., Salas, R. (2001) Geologic Modeling and Simulation - Sedimentary Systems, 1 edn., chap. Simulating carbonate and mixed carbonate-clastic sedimentation using predator-prey models, pp. 169-204. Kluwer Academic.

Bitzer, K., Salas, R. (2002) Simsafadim: Three-dimensional simulation stratigraphic architecture and facies distribution modelling of carbonate sediments. Computers and Geosciences 28(10), 1177- 1192.

Carmona, A., Clavera-Gispert, R., Gratacós, O., Hardy, S. (2010) Modelling syntectonic sedimentation: Combining a discrete element

model of tectonic deformation and a process-based sedimentary model in 3d. Mathematical Geosciences 42(5), 519-534.

Clavera-Gispert, R., Carmona, A., Gratacós, O., Tolosana-Delgado, R. (2012) Incorporating nutrients as a limiting factor in carbonate modelling. Palaeogeography, Palaeoclimatology, Palaeoecology 329-330, 150-157.

Gómez-Paccard, M., López-Blanco, M., Costa, E., Garcés, M., Beamud, E., Larrasoaña, J.C. (2012)Tectonic and climatic controls on the sequential arrangement o fan alluvial fan/fan-delta complex (Monserrat, Eocene, Ebro Basin, NE Spain). Basin research, 24, 437-455.

Gratacós, O., Bitzer, K., Cabrera, L., Roca, E. (2009a) Simsafadim- clastic: A new approach to mathematical 3d forward simulation modelling for terrigenous and carbonate marine sedimentation. Geologica Acta 7(3), 311-322.

Gratacós, O., Bitzer, K., J.L.Casamor, Cabrera, L., Calafat, A., Canals, M., Roca, E. (2009b) Simulating transport and deposition of clastic sediments in an elongate basin using the simsafadim-clastic program: The camarasa artificial lake case study (ne spain). Sedimentary Geology 222(1-2), 16-26.

López-Blanco, M., Marzo, M., Piña, J. (2000a) Transgressive-regressive sequence hierarchy of foreland, fan delta clastic wedges (Montserrat and Sant Llorenç del Munt, Middle Eocene, Ebro basin, Spain) Sedimentary Geology, 138 (1-4). pp 41-69.

López-Blanco, M., Marzo, M., Burbank, D., Vergés, J., Roca, E., Anadón, P.,Piña, J. (2000b) Tectonic and climatic controls on the development of foreland fan deltas: Montserrat and Sant Llorenç del Munt systems (Middle Eocene, Ebro basin, NE Spain) Sedimentary Geology, 138 (1-4). pp 17-39.

The balance between uplift and fluvial erosion over a single seismic cycle – an example from Taiwan

Kristen Cook[1], Fabien Graveleau[2], Jens Turowski[1], Niels Hovius[1], John Suppe[3]

[1]*Helmholtz Zentrum Potsdam, GFZ Section 5.1, Potsdam, Germany*
[2]*Géosystèmes, Université Lille 1, CNRS UMR 8217, Villeneuve d'Ascq*
[3]*Department of Geosciences, National Taiwan University, Taipei*
e-mail: *kristenlcook@gmail.com*
session: *Tectonics and Surface Processes*

The relationship between tectonic and geomorphic processes is important for understanding how topography evolves, and how the landscape reflects tectonic and climatic signatures. We present a case study of the relationship between uplift and erosion on the scale of a single seismic cycle, in which we can observe the creation of substantial coseismic topography and its subsequent removal by fluvial erosion. In Sept. 1999, the Mw 7.6 Chi-Chi earthquake struck western Taiwan. At the northern end of the rupture zone, in the Daan River valley, the earthquake activated the Dongshi Anticline, resulting in up to 13 m of uplift due to coseismic folding. Where the Daan River crosses the anticline, the river responded to the coseismic uplift by very rapidly cutting into the uplifted topography, and by 2009 the river had carved a narrow bedrock gorge extending the width of the anticline. In the current stage of erosion, the river has ceased cutting down, and is now eroding laterally. Although widening within the gorge is relatively slow, the river is cutting back the upstream boundary of the anticline at a rate of about 15 m/yr. At this rate, the river will remove the uplifted topography and returned to its pre-uplift morphology in about 50 years. The post-1999 erosion rates in the Daan River are several orders of magnitude faster than background rates, and represent a transient phase of erosion in response to the disequilibrium created by coseismic uplift. In this case, the river is able to respond to the coseismic uplift of the Dongshi anticline solely through this transient response, and without long term changes in the river's morphology. This example highlights the potential importance of short-lived signals of uplift and erosion in the relationship between tectonics and landscape morphology.

Joint analog modeling of marine and terrestial geological processes: state of the art and new developments

S. Dominguez[1]

[1] *University of Montpellier 2, CNRS, UMR 5243 Geosciences, Place E. Bataillon, F-34095 Montpellier, France*
e-mail: *stephane.dominguez@gm.univ-montp2.fr*
session: *Tectonics and Surface Processes*

In Geosciences, an invisible frontier separates marine geologists and geophysicists from their "terrestrial" colleagues. In other words, most of geologists are specialized on dry or wet geological context and often lack of an integrating view linking land and sea observation. Consequently, the interactions and couplings between these two domains, where intense material fluxes and geomorphological processes concentrate, remain relatively unstudied. This is also the case for the analog modeling approach that generally focus exclusively either on terrestrial processes like mountain building, river dynamics, watershed evolution or on marine ones like marine sedimentation processes, submarine landslides, turbidite currents dynamics. Up to now, very few experimental works have investigated the interactions that exist between land and submarine geological processes at the scale of a whole active or passive margin.

Compared for instance to active foreland settings, several first order additional key parameters must be taken into consideration (Figure 1), like eustatic changes of sea level, sea bottom tectonic deformation, underwater sediment transport controlled by current dynamics, biogenic hemipelagic sediment production and also fluid pressure driven processes (mud diapirism, hydrofracturation,...).

Some of them have been investigated using analog modeling. One should notice that the state of the art can be quickly summarized since there is apparently a limited amount of published works available in the literature. Among those, several workers have developed original experimental setups, modeling self-channelized gravity currents to study the formation of submarine fans and canyons (e.g. Muto and Steel 2001; Métivier et al., 2005; Lajeunesse et al., 2010). Others have modeled experimentally passive margin sedimentation, particularly to study delta stratigraphy architecture (e.g. Van Heijst et al. 2001b; Kim and Paola, 2007; I. Fardiansyah & A. Budiman, GPRG) with convincing results when compared to their natural counterparts imaged by seismic profiling (Figure 2). Most of these experimental works, however, simulate land sediment input to the sea using a simple pipe providing a water+sand mixture flow which does not allow to reproduce feedback process, that is the influence of marine sedimentation on landscape morphology dynamics. S. Y. J. Lai and H. Capart (Hydraulic and Ocean Engineering National Cheng Kung University) have been among the firsts to perform geomorphic experiments coupling landscape and submarine erosion/sedimentation processes (Figure 2). Their results show striking analogies between model and nature in terms of aerial and submarine morphologies.

Why such type of experiments are still relatively scarce ? The fact is that analog modeling faces several limitations related to the use of fresh and salty water to erode landscape morphology and to simulate the sea which inevitably induced scaling distortions (Paola, 2009). Finding an appropriate analog material rheology to model both

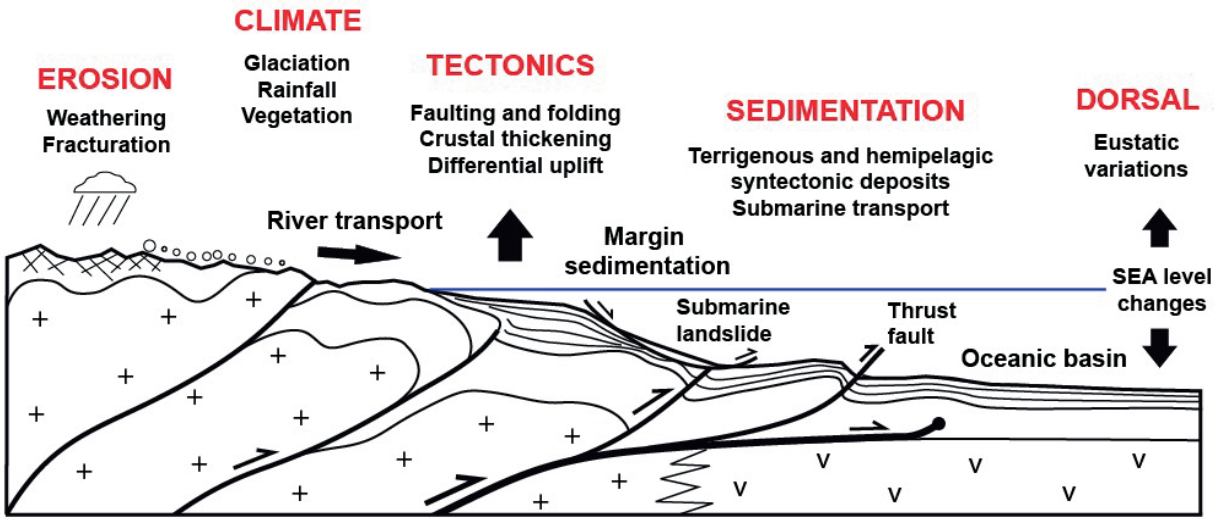

Fig. 1.: Geodynamic context and main interactions between active geological, climatic, terrestrial and marine processes

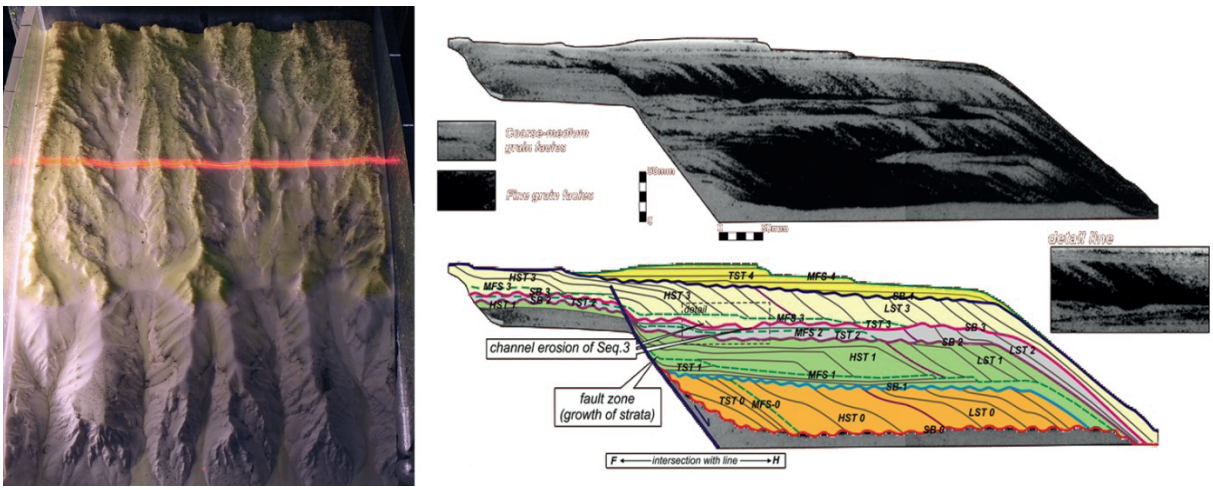

Fig. 2.: Left) geomorphic experiment coupling landscape and submarine erosion/sedimentation processes performed by S. Y. J. Lai and H. Capart (Hydraulic and Ocean Engineering National Cheng Kung University, Taiwan). Right) geomorphic experiment dedicated to study interactions between margin sedimentation /active faulting/sea level changes performed by I. Fardiansyah & A. Budiman (GPRG, Indonesia).

landscape and seascape morphogenetic processes is also another difficulty to overcome, especially when tectonic deformation must be also taken into account.

To illustrate the scientific issues and the potential of modeling coupled sea-land geological processes, I will present some recent technical developments and preliminary results dealing with the tectonic inversion of the Algerian passive margin (Figure 3) and an ongoing project to study tectonic and morphogenetic sea-land processes on the Eastern coast of Taiwan. The Algerian margin is a tectonized passive margin that undergoes active compression since at least Late Quaternary. As a result, its submarine morphology and terrestrial reliefs suffered huge changes in the last 2 millions years including coastal emersion, margin shortening and steepening. The Eastern coast of Taiwan is one of the most tectonically active region in the world. Here, the collision

between the Luzon volcanic arc, carried by the Philippine Sea Plate, and the continental margin of the Eurasian plate induces the formation of a high mountain range (4000m) that literally emerge from the sea at a very high speed. It is, then, another appropriate natural laboratory to study the couplings between submarine and terrestrial geological processes.

These two natural examples and corresponding experimental models will be used to demonstrate that analog modeling is potentially a relevant tool to investigate such complex geodynamic contexts which cannot be studied yet numerically in 3D with the same degree of detail. The final objective of this presentation will be to outline the interest of developing new experimental projects, scientific collaborations and improving technics to enlarge the field of investigation of analog modeling.

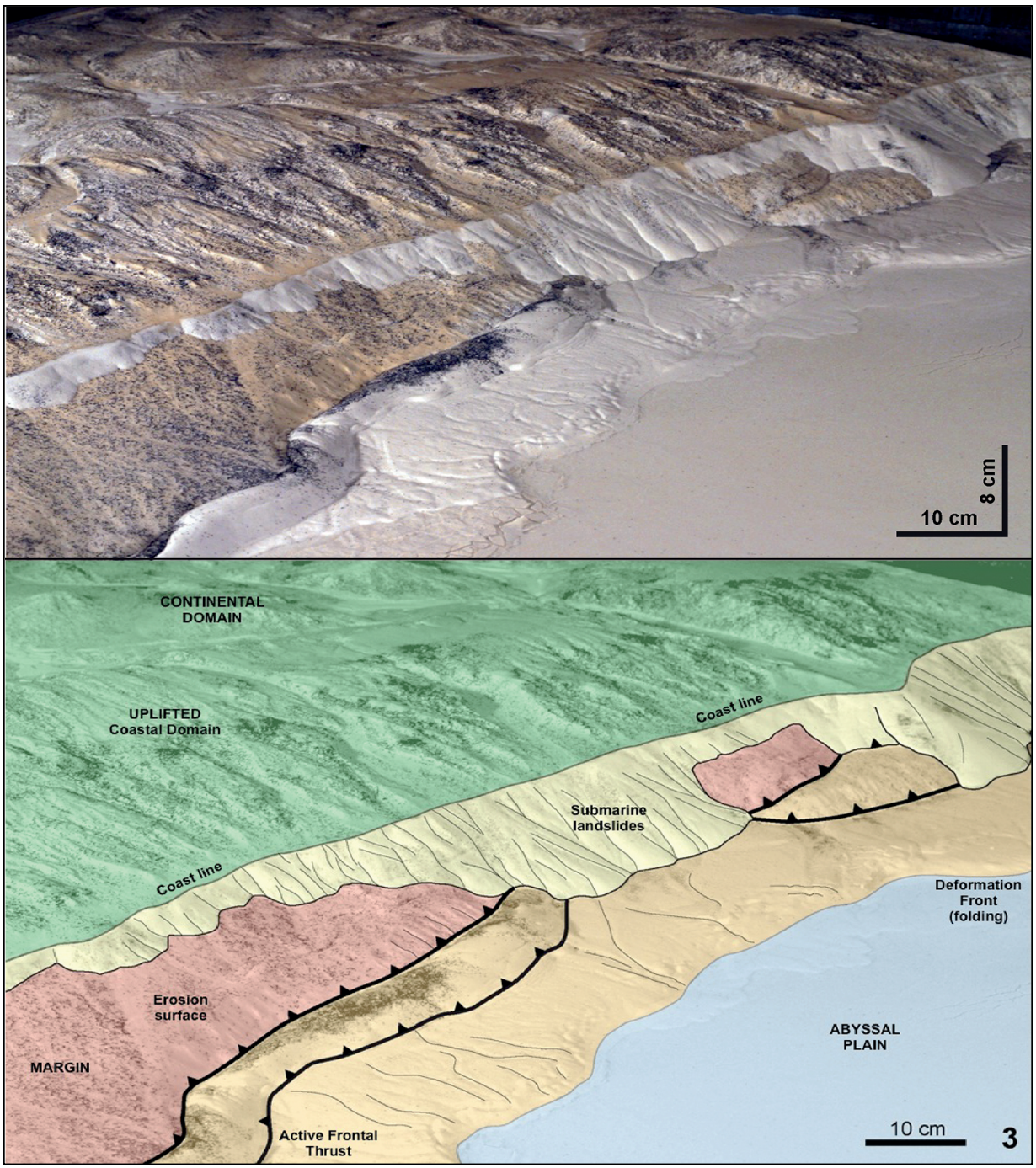

Fig. 3.: Example of the final stage (water has been removed) of a morphotectonic analog experiment simulating the Plio-Quaternary morpho-tectonic evolution of the Algerian margin. Hemipelagic (and pelagic) sedimentation was not simulated, only terrigenous sedimentation (sediments transported from land to the ocean by rivers) were modeled

Fold growth rates in 3D buckle folds

Marcel Frehner[1]

[1] *Geological Institute, ETH Zurich, Switzerland*
e-mail: *marcel.frehner@erdw.ethz.ch*
session: *Tectonics and Surface Processes*

Summary: Geological folds are inherently 3D structures; therefore they also grow in three dimensions. Here, fold growth in all three dimensions is quantified by numerically simulating upright single-layer folds in 3D Newtonian media. Horizontal uniaxial shortening leads to a buckling instability, which grows from a point-like initial perturbation in all three dimensions by fold amplification (vertical), fold elongation (parallel to fold axis), and sequential fold growth (parallel to shortening direction) The two lateral directions exhibit similar averaged growth rates leading to bulk fold structures with aspect ratios close to 1. However, fold elongation is continuous with increasing bulk shortening, while sequential fold growth exhibits jumps whenever a new sequential fold appears. Compared to the two lateral growth directions, fold amplification exhibits a slightly higher growth rate.

Introduction

Geological folds are important natural features for structural geologists. In the field, the orientation and geometry of small-scale folds in the three-dimensional (3D) space helps identify larger-scale structures not visible in one single outcrop. Fold structures also provide an essential basis for tectonic interpretations, for example for estimating tectonic shortening directions. Equally important, the wavelength, the arclength, and the overall geometry of a fold are functions of the rheological parameters of a folded rock layer and its surrounding matrix. Therefore, analyzing the shape of a fold can reveal information about the rheological properties of the involved rocks (Huddleston and Treagus, 2010).

The fold shape that can be observed in the field is a result of the fold growth history. Therefore, it is essential to not only describe the fold shape but also to understand the process of fold growth. Geological folds are inherently 3D structures; hence their growth also needs to be studied in 3D.

Definitions of 3D fold growth

To avoid confusion, the following terminology for fold growth in 3D is used here, using the coordinate system defined in Figure 1:

- Fold amplification (growth in z-direction) describes the growth from a fold shape with low limb-dip angle to a shape with larger limb-dip angle.
- Fold elongation (growth in y-direction) is parallel to the fold axis and describes the growth from a dome-shaped (3D) structure to a more cylindrical fold (2D).
- Sequential fold growth (growth in x-direction) is parallel to the shortening direction and describes the growth of additional folds adjacent to the initial isolated fold. The initial fold is termed 0th sequential fold; later grown folds are numbered consecutively.

Here, lateral fold growth is used as an umbrella term for both fold elongation and sequential fold growth.

Aim of this study

Existing studies do not quantify all three growth directions at once. Analytical solutions for 3D

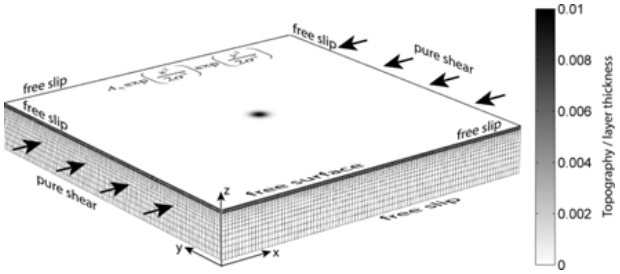

Fig. 1.: Initial numerical model grid, boundary conditions, and coordinate system for studying 3D fold growth. Gray values on the top interface represent the initial topography (equation given in the figure), normalized by the thickness of the top layer. Arrows indicate the pure-shear shortening boundary condition.

folding (e.g., Fletcher, 1991) neglect the two lateral growth rates because a periodic initial perturbation is assumed. The few numerical 3D folding studies (e.g., Schmid et al., 2008) do not quantify fold growth, but rather investigate one specific 3D phenomenon (e.g., linkage). The aim of the presented study is to numerically simulate simplified test cases of 3D folding and to quantify fold growth in all three dimensions to better understand the first-order relationships between the different growth directions.

Model and Methods

3D buckle folding is assumed to be a slow flow process governed by Newtonian rheology. The self-developed finite-element (FE) code solving the corresponding continuum mechanics equations is a 3D version of the code tested and used in Frehner and Schmalholz (2006) and Frehner (2011). The model (Figure 1) consists of a higher-viscosity layer (thickness H_L=1) on top of a lower-viscosity layer (thickness H_M»H_L) with viscosity ratio R. The model has a free surface and is compressed horizontally in x-direction with a constant shortening strain rate, D_{xx}<0. This corresponds, for example, to pure-shear analog models with lubricated base and side walls or to fold belts, where flow parallel to the fold axes is prohibited.

To allow a mechanical folding instability to develop, a point-like initial perturbation is added to the bottom and top interfaces of the upper layer corresponding to a two-dimensional Gaussian (equation given in Figure 1; A_0=0.01). The effective initial wavelength of the Gaussian is defined as

$$\lambda_0^{eff} = 2 \times FWHM = 2 \times \sqrt{8ln(2)\sigma} \qquad (1)$$

The full width at half maximum (FWHM) corresponds to the circle diameter in the x-y-plane, within which the initial perturbation is larger than $A_0/2$ (i.e., half maximum).

During the FE-simulations, the bulk amplitudes (or extent) of the fold structure in all three coordinate directions are calculated based on the folded upper surface of the model:

- Amplitude in z-direction:

$$A_z = z\Big|_{x=0,y=0} - z_{ref} \qquad (2)$$

- Amplitude in y-direction:

$$A_y = max(y) \text{ where } z\Big|_{x=0} - z_{ref} = \frac{A_0}{2} \qquad (3)$$

- Amplitude in x-direction:

$$A_x = max(x) \text{ where } z\Big|_{y=0} - z_{ref} = \frac{A_0}{2} \qquad (4)$$

The reference topography, z_{ref}, is the average of the upper model surface. In Figure 2, A_z corresponds to the color in the model center and A_y and A_x correspond to half the extent of the central contour line in y-direction and to half the maximal extent of all contour lines in x-direction, respectively.

Exponential growth is assumed in all three directions. Taking into account the shortening and extension directions, the exponential bulk amplitude evolution laws are (t is time):

- Exponential growth in z-direction:

$$A_z = A_z\Big|_{t=0} exp[-(q_z+1)D_{xx}t] \qquad (5)$$

- Exponential growth in y-direction:

$$A_y = A_y\Big|_{t=0} exp[-q_y D_{xx}t] \qquad (6)$$

- Exponential growth in x-direction:

$$A_x = A_x\Big|_{t=0} exp[-(q_x - 1)D_{xx}t] \qquad (7)$$

Equations (2)–(7) are valid for the fold structure as a whole (bulk values). Similarly, amplitudes can be calculated for each individual sequential syn- and antiform. The amplitudes in z- and y-direction of the initial (or 0^{th} sequential) fold are equal to the bulk amplitudes.

Results and Interpretations

As an example, the simulation with viscosity ratio R=100 and initial perturbation σ=6 (Figure 1) is shown and discussed below.

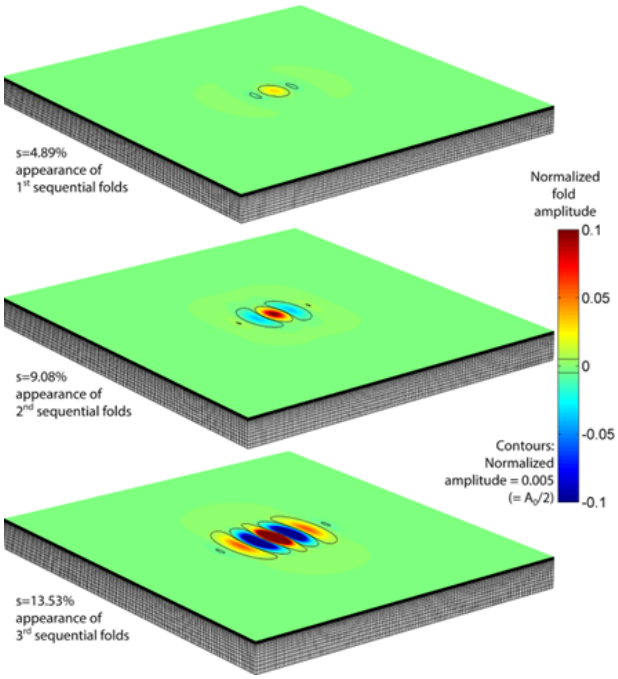

Fig. 2.: Snapshots of a typical FE-simulation showing the evolution of the 3D fold structure with increasing background shortening, s. The fold amplitude (z-direction) is normalized by the thickness of the top layer; black lines are contour lines of the normalized fold amplitude equal to half the initial value (0.005). The maximum extent in x- and y-direction of these contour lines is used to calculate the fold amplitude in x- and y-direction (Equations (5) and (4)). Parameters for this simulation are: R=100 and σ=6.

Fold shape evolution and individual folds

Figure 2 shows snapshots of the evolving fold structure with increasing background shortening ($s = 1^{\smile} exp(D_{xx}t)$). The fold grows in all three dimensions. Fold amplification (z-direction) is evident from the increasing topography (indicated by colors); fold elongation (y-direction) is evident from the elongation of the $A_0/2$ topographic contour line in the model center; sequential fold growth (x-direction) is evident from the sequential appearance of new $A_0/2$ topographic contour lines.

The initial isolated fold starts with normalized amplitudes, aspect ratio, and amplitude ratios all equal to 1 (Figure 3), which represents the initial condition of the simulation. Both the z- and y-amplitudes of the individual folds increase with increasing shortening. At the same time, growth in x-direction of the individual folds is limited to an x-amplitude of around 1 (Figure 3a) showing that the fold structure as a whole grows in x-direction by sequential folding, and not by the growth of one individual anti- or synform. The combination of the two lateral growths leads to an increasing aspect ratio of the initial isolated fold (Figure 3b). New sequential folds appear already with an elevated aspect ratio and continue elongating with further shortening (see also Figure 2). Generally, fold amplitude ratios with the z-amplitude as the denominator (Figure 3c) decrease with increasing shortening, indicating that fold growth in z-direction exhibits a higher rate than the two lateral directions.

Bulk fold amplitudes and growth rates in 3D

Figure 3 also shows the data for the bulk fold structure (thick lines). The bulk amplitudes in z- and y-direction are equal to the amplitudes of the initial isolated fold and increases continuously with increasing shortening. Growth of the fold structure in x-direction (Figure 3a) is marked by sudden jumps every time a new sequential fold appears. Despite these jumps, the average amplitude in x-direction is of the same order as

in y-direction leading to an almost constant bulk fold aspect ratio of around 1 (Figure 3b). Such equal growth in both lateral directions also occurs when using different parameter combinations and seems to be a universal feature of 3D fold growth. However, these two lateral growths exhibit a lower rate compared to fold amplification (growth in z-direction) leading to fold amplitude ratios clearly below 1 (Figure 3c). This is also the case for the other tested parameter combinations.

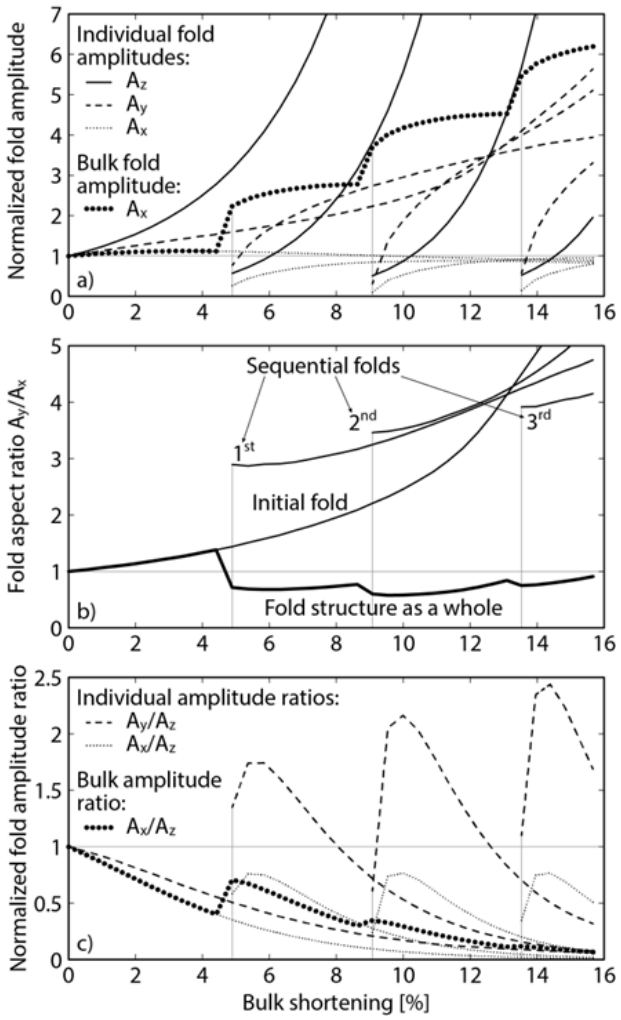

Fig. 3.: Fold amplitude (a), fold aspect ratio in the x-y-plane (b), and fold amplitude ratio (c) with increasing shortening for the individual sequential folds (individual anti- and synforms; thin lines) and the bulk fold structure (thick lines) for the same simulation as in Figure 2. The bulk fold amplitudes in z- and y-direction are equal to the individual fold amplitudes of the initial fold. All values are normalized by the initial amplitude in each corresponding direction. b) and c) are derived from a). Vertical gray lines indicate the first appearance of sequential folds.

Applying Equations (5)–(7) to the amplitude data in Figure 3a, the fold growth rates in all three directions can be calculated (Figure 4). The fold amplification rate (z-direction) increases slightly (from ∼19–25) with increasing shortening (Figure 4a), while the fold elongation rate (y-direction) stays roughly constant at a value of around 10. The sequential fold growth rate (x-direction) exhibits sharp jumps when new sequential folds appear. In the long term, both lateral fold growth rates are similar, represented by a lateral growth rate ratio close to 1 (Figure 4b), and about half of the fold amplification rate (growth rate ratio around 0.5; Figure 4b). This general relationship between the different fold growth rates also occurs for all other tested parameter combinations.

Discussion

Recently, interest in the lateral growth and linkage process of natural folds has been renewed by the oil- and gas-industry because it can lead to compartmentalization of structurally controlled reservoirs within an anticline. Previous studies only considered fold elongation to explain the linkage process (Bretis et al., 2011; Grasemann and Schmalholz, 2012), without including the second lateral growth direction (sequential fold growth). However, this study demonstrates that both lateral growth directions are equally important. In case two initially isolated fold structures grow in all three directions, the initial fold of one structure (0^{th} sequential fold) may well link with the 1^{st} sequential fold of the second structure. Grasemann and Schmalholz (2012) termed this scenario *no linkage*, yet it is equally important for understanding linked bulk fold structures and the term *1st order linkage* is proposed here. Accordingly, Grasemann and Schmalholz (2012)'s *linear linkage* and *oblique linkage* scenarios (linkage of two initial folds) are categorized as *0th*

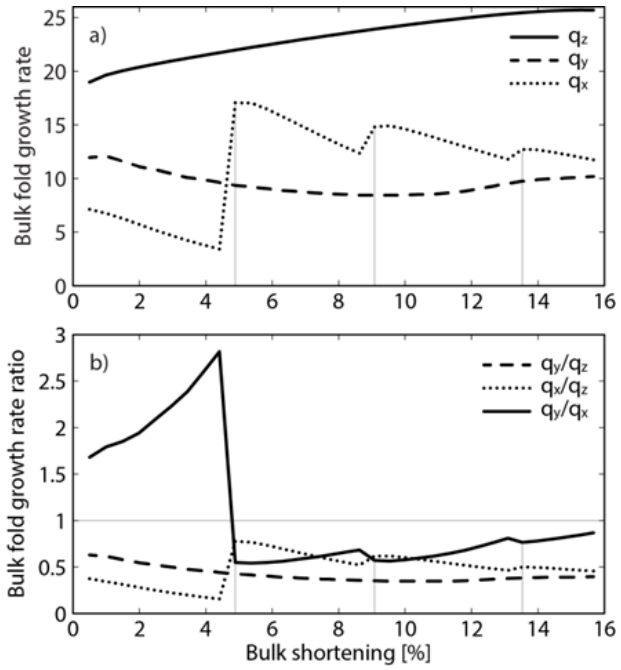

Fig. 4.: Fold growth rates (a) and ratio between fold growth rates (b) for the bulk fold structure with increasing shortening for the same simulation as in Figure 2 and 4. (a) is derived by applying Equations (6)–(8) to data shown in Figure 3a. (b) is derived from (a). Vertical gray lines indicate the first appearance of sequential folds.

order linkage.

The numerical simulations represent simplified test cases in that they only comprise a two-layer system, linear viscous (Newtonian) rheology, and no erosion at the upper surface. Therefore, the modeled geometries may not be translated one-to-one to natural fold structures. However, the aim of these simulations is to demonstrate first-order phenomena of 3D fold growth. The general result of almost equal fold growth rates in both lateral directions (fold elongation and sequential fold growth) and slightly larger fold growth rate in vertical direction (fold amplification) is expected to still hold in more realistic modeling scenarios or natural situations.

Conclusions

Numerical 3D folding simulations using a range of parameter combinations demonstrated that a fold structure grows in the two lateral directions with similar rates while the fold amplification rate is slightly higher. Such growth behavior results in fold structures that hardly change their bulk aspect ratio with increasing shortening. If a fold structure originates from an isolated perturbation (e.g., diapir) its aspect ratio remains roughly 1:1; if a fold structure originates from a line perturbation (e.g., fault) its aspect ratio remains large. However, large-aspect ratio fold structures can also be formed by linkage of two or more individual fold structures. Thereby, higher-order linkage (linkage between sequential folds of different order) is equally important as 0^{th} order linkage because of the equal fold growth rates in the two lateral directions.

Acknowledgements

Discussions with Neil Mancktelow and Naiara Fernandez are greatly acknowledged. This work has been supported by the ETH Zurich, Switzerland.

References

Bretis, B., Bartl, N. and Grasemann, B., 2011. Lateral fold growth and linkage in the Zagros fold and thrust belt (Kurdistan, NE Iraq). Basin Research, 23, 615–630.

Fletcher, R.C., 1991. Three-dimensional folding of an embedded viscous layer in pure shear. Journal of Structural Geology, 13, 87–96.

Frehner, M., 2011. The neutral lines in buckle folds. Journal of Structural Geology, 33, 1501–1508.

Frehner, M. and Schmalholz, S.M., 2006. Numerical simulations of parasitic folding in multilayers. Journal of Structural Geology, 28, 1647–1657.

Grasemann, B. and Schmalholz, S.M., 2012. Lateral fold growth and fold linkage. Geology, 40, 1039–1042.

Hudleston, P.J. and Treagus, S.H., 2010. Information from folds: A review. Journal of Structural Geology, 32, 2042–2071.

Schmid, D.W., Dabrowski, M. and Krotkiewski, M., 2008. Evolution of large amplitude 3D fold patterns: A FEM study. Physics of the Earth and Planetary Interiors, 171, 400–408.

Furrow-and-ridge morphology on rockglaciers explained by gravity-driven buckle folding: A case study from the Murtèl rockglacier (Switzerland)

Marcel Frehner[1], Isabelle Gärtner-Roer[2], Anna H.M. Ling[1,2]

[1] *Geological Institute, ETH Zurich, Switzerland*
[2] *Department of Geography, University of Zurich, Switzerland*
e-mail: *marcel.frehner@erdw.ethz.ch*
session: *Tectonics and Surface Processes*

Summary: Our study promotes buckle folding as the dominant process for the formation of furrow-and-ridge morphology on rockglaciers. Applying analytical buckle folding expressions to a high-resolution digital elevation model of the Murtèl rockglacier allows us to estimate the viscosity ratio between the higher-viscous active layer and its almost pure ice substratum. Using these constraints in a dynamic finite-element model of viscous rockglacier flow reproduces all key natural observations of the furrow-and-ridge morphology.

Introduction

Rockglaciers often feature a prominent furrow-and-ridge morphology, for which the Murtèl rockglacier in Switzerland (Figure 1) is a spectacular example. Previous studies suggesting that a longitudinal compressive flow in the lower part of a rockglacier is responsible for these structures are based on qualitative descriptions and remained speculative.

Buckle folding is the mechanical response of a layered viscous material to shortening if the mechanical contrast between the layers is significant. The resulting buckle folds are common structures in rocks and are well-studied in field outcrops, experimentally, numerically, and mathematically.

We propose that gravity-driven buckle folding is also the main responsible process for the formation of the transverse furrow-and-ridge morphology on rockglaciers. In this cross-disciplinary study we use the buckle folding theory, which is well-established in the field of structural geology, and apply it to the field of rockglacier geomorphology.

Data and Methods

For building a representative model we require two key ingredients: accurate geometrical information and information on the material behavior (i.e., rheology). Both ingredients are elucidated below in two subchapters

Geometrical Information

We analyze the surface topography using a 1 m-resolution digital elevation model (DEM) based on low-altitude aerial photographs. The three-dimensional (3D) furrow-and-ridge morphology is evident when considering the 200 m-diameter differential elevation (diffDEM; Figure 1C). The average wavelength of the furrow-and-ridge structure is around 20 m; the average amplitude is around 2 m.

Borehole deformation measurements (Arenson et al., 2002) demonstrate that the lower part of the Murtèl rockglacier is immobile and detached from the upper 30 m by a discrete shear zone. Borehole image logs and integrated interpretations of geoelectric, seismic, and georadar data

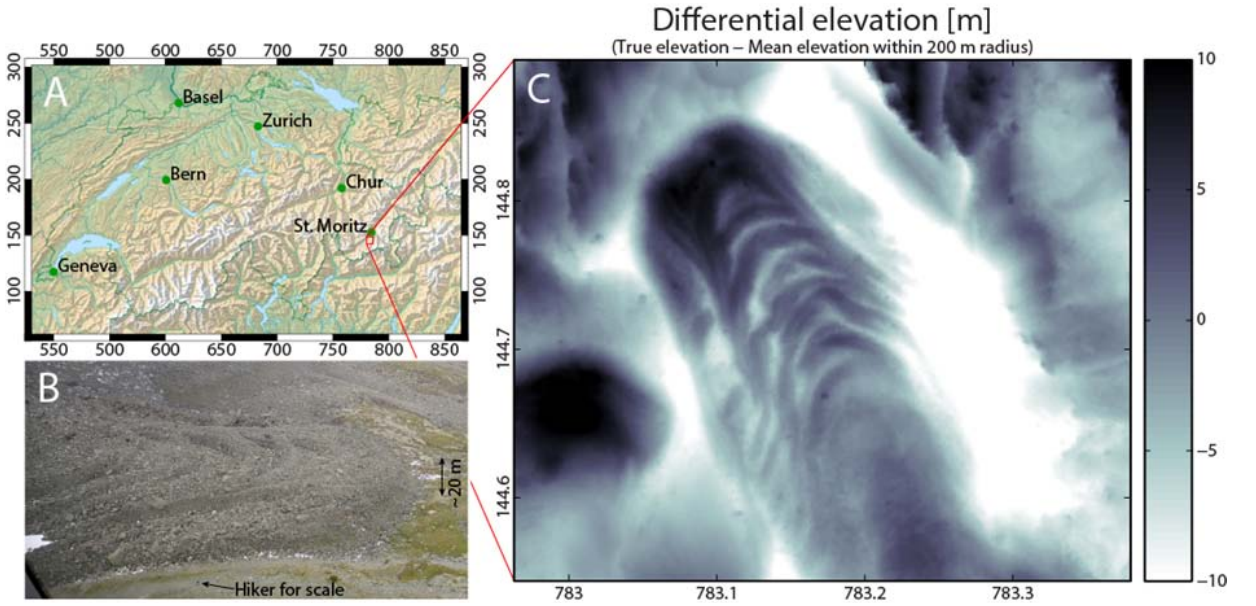

Fig. 1.: Location (A; source Swiss Federal Office of Topography) and surface structure (B, C) of the Murtèl rockglacier in Switzerland. The differential elevation is calculated as the true elevation minus the mean elevation within a 200 m diameter circle. The employed 1 m-resolution DEM is based on photogrammetry. Coordinates in Swiss coordinate system CH1903.

(Maurer and Hauck, 2007) suggest that the upper part is relatively homogeneous and consists of almost pure ice. The top-most active layer is 3–5 m thick and is a mixture of ice and rock fragments with sizes from sand to boulders (Figure 1B), which freezes and unfreezes during the course of a year. Kääb et al. (1998) speculated that the thickness of the active layer below ridges is larger than below furrows.

Based on this geometrical information we approximate the Murtèl rockglacier as a two-layer system consisting of a lower 27 m thick layer and an upper 3–5 m thick layer. Both layers are assumed to obey a viscous flow law, the upper exhibiting a higher viscosity because of its rock fragment content. We consider the part below 30 m not important for the formation of furrows and ridges and we neglect it.

Rheological information

Borehole deformation experiments (Arenson et al., 2002) demonstrate that the shear zone at 30 m depth accommodates 60% of the total deformation. The parabolic flow profiles above the shear zone can be approximated using a viscous flow law. For the active layer it is not possible to determine the power-law exponent, first because it is a complex mixture of ice and rock fragments and second because the borehole data is too sparse in this layer. Hence, we treat both layers as Newtonian (linear viscous) materials. This assumption has the advantage that the modeled deformation does not depend on strain rate and on absolute viscosity values, but only on the viscosity ratio.

To determine the viscosity ratio, R, we assume that the furrow-and-ridge morphology is a result of viscous buckle folding. The Fold Geometry Toolbox (FGT; Adamuszek et al., 2011) automatically analyzes the geometry of a folded layer and applies various buckle folding theories to determine the viscosity ratio between the folded layer and its surrounding. We feed the FGT with longitudinal sections of the furrow-and-ridge geometry derived from the diffDEM (Figure 1C). We vary the thickness of the active layer (3–5 m; Figure 2A) according to its uncertainty and also use a non-constant thickness (Kääb et al.,

1998). The FGT yields viscosity ratios of R=9–21 depending on the input model (Figure 2B).

Numerical Finite-Element Modeling

Based on the above geometrical and rheological analysis we designed a finite-element (FE) model (Figure 3B) to simulate rockglacier flow under the effect of gravity. The model solves the governing force balance and rheological (Newtonian) equations in 2D (details in Frehner, 2011; Frehner et al., 2012). For the Murtèl rockglacier the 2D approximation is justified because of its straight tongue-like geometry and unidirectional flow field (Kääb et al., 1998). The initial model surface is randomly disturbed (Figure 3A), representing natural irregularities of rock fragments and boulders, but also allowing the mechanical buckling instability to initialize.

Results

Figure 3C and 4A show the initial model state. Because we only consider the viscosity ratio, calculated stresses cannot be taken as absolute stress levels. The active layer exhibits layer-parallel compression towards the rockglacier toe, which is also reflected by the orientation of the most compressive stress parallel to the layer. Immediately below the active layer, compression is much smaller but still layer-parallel. These discontinuous stresses across the layer interface drive the buckling instability.

For further analysis we focus on the rockglacier toe (Figure 4), where active buckling takes place. The modeled buckle folds develop self-consistently with a wavelength of around 20 m. Around 150 m from the rockglacier front, compression in the active layer is largest; hence buckle folds develop the fastest. Further towards the front, buckle folds still develop, but at a lower rate. This is directly comparable to the Murtèl rockglacier (Figure 1C). The amplitudes in Figure 4C of about 2 m are comparable to the present-day amplitudes on the Murtèl rockglacier; hence, Figure 4C represents today's situation while Figure 4B represents an earlier situation.

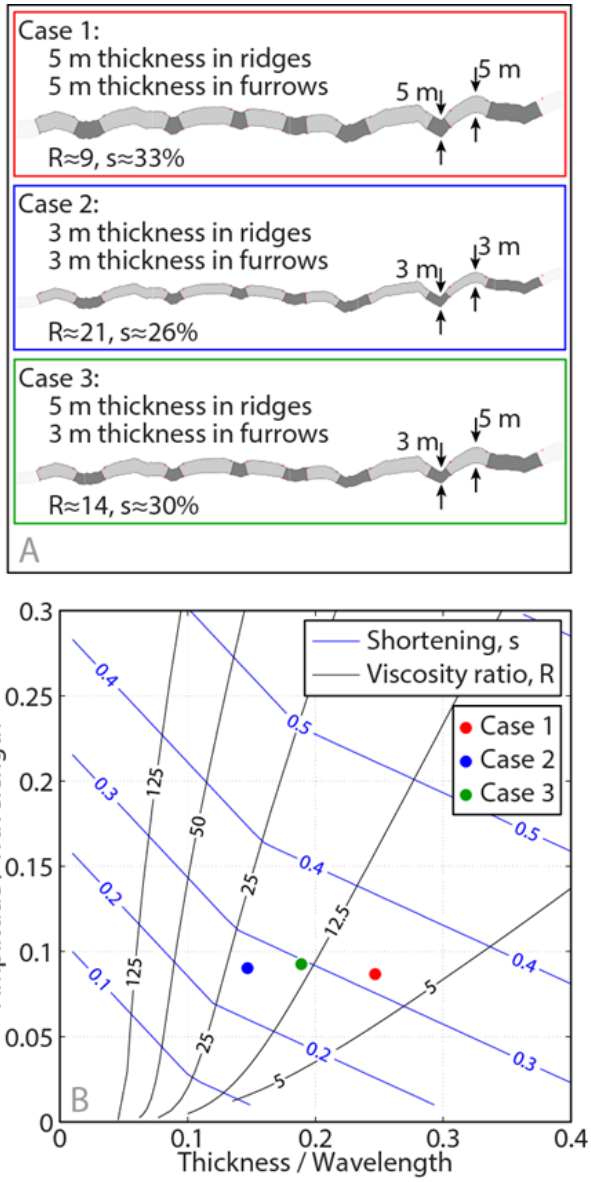

Fig. 2.: Geometrical and rheological information of the Murtèl rockglacier (modified screenshots from the FGT). A: Different input models using different layer thicknesses of the active layer. Gray shades: furrows and ridges as identified by the FGT. B: Resulting fold amplitude-to-wavelength and thickness-to-wavelength ratios with overlain shortening and viscosity ratio contour lines.

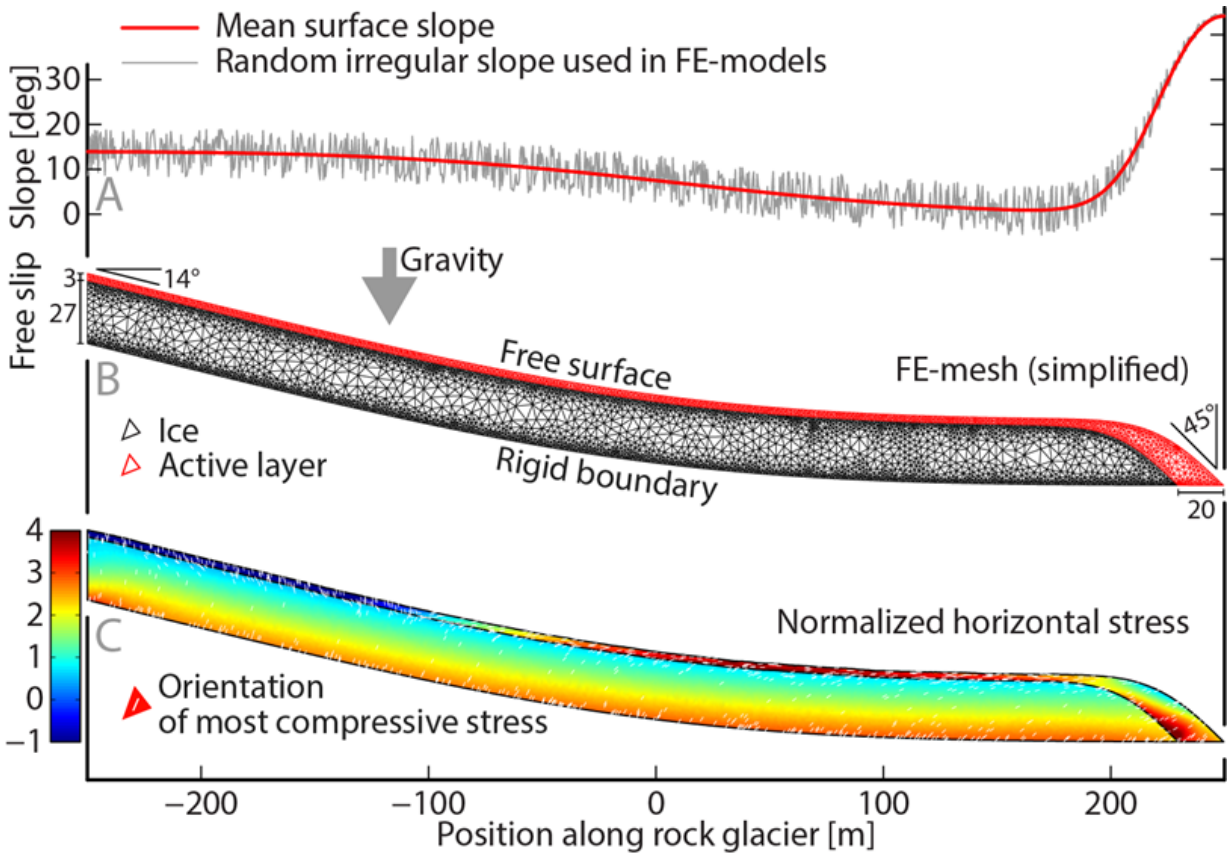

Fig. 3.: Initial and boundary conditions of the FE model, which is inspired by the Murtèl rockglacier. The numerical mesh (B) is simplified because the real mesh is too dense to be depicted. C shows the initial normalized horizontal stress (positive = compression) and the orientation of the most compressive stress as white lines.

Figure 4D shows the modeled borehole deformation (colored lines) from the surface down to 5 m above the fixed model bottom. The deformation of all boreholes and for both time intervals exhibits the typical parabolic shape, confirming the viscous flow profile within the rockglacier. The developing buckle folds disturb this otherwise smooth deformation profile in the active layer. Naturally, data measured on the Murtèl rockglacier (gray lines) show more variations. However, on average the deformation profiles are also parabolic and disturbed in the active layer. Hence, the modeled borehole deformation profiles can be directly compared to the real data.

Discussion

Because we do not accurately describe the shear zone, our FE simulation only accounts for 40% of the total deformation. Borehole deformation data and photogrammetric and terrestrial geodetic surveys yield surface velocities of the Murtèl rockglacier of 5 (Kääb et al., 1998) to 6 cm a–1 (Arenson et al., 2002; Müller et al., 2014). With 40% of this surface velocity, 625–950 years are necessary to reach the modeled surface displacement of 15–19 m (Figure 4D). While the natural 3D deformation (compared to the 2D model) may not significantly alter the deformation geometry, it does affect the rate of deformation. The curved furrows and ridges (Figure 1C) indicate a viscous flow pattern also in map-view resembling an open-channel flow. We estimate the velocity re-

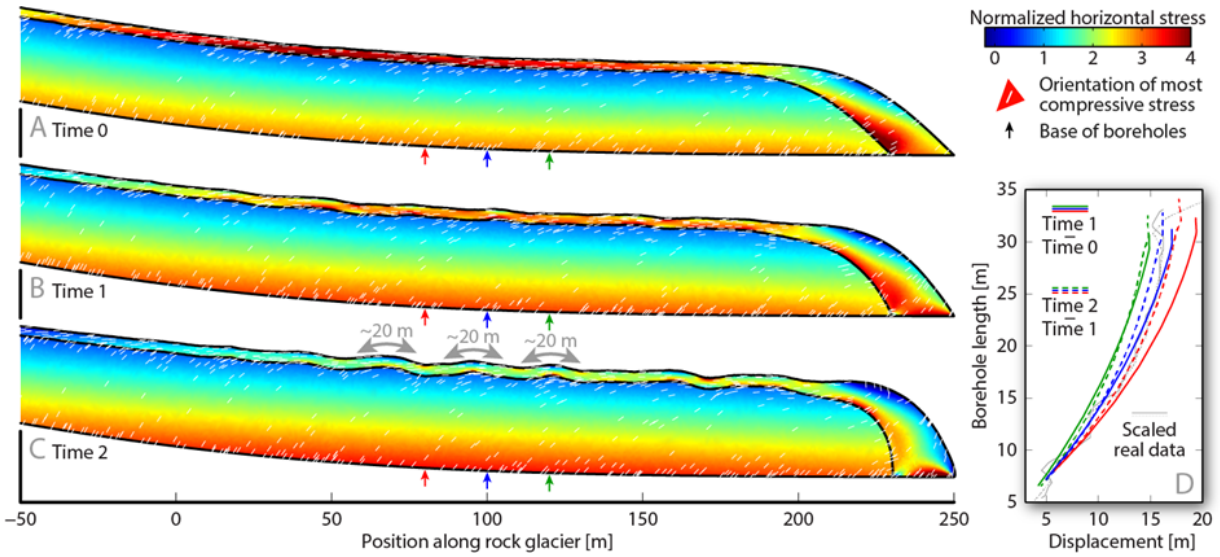

Fig. 4.: Snapshots at three different times (Times 0–2) of the rockglacier toe. D shows the modeled borehole deformation between Times 0 and 1 and between Times 1 and 2 at locations indicated in A–C. The two gray lines correspond to the borehole deformation data of Arenson et al. (2002) measured on the Murtèl rockglacier in a similar location.

duction in such a 3D flow to about 35% compared to our modeled 2D flow. Hence, the estimated time to develop the furrows and ridges extends to 960–1460 years. Time 1 in Figure 4 corresponds to 480–730 years and Time 2 corresponds to 960–1460 years after the initial state (Time 0).

Conclusions

Using the Murtèl rockglacier as an example, we promote gravity-driven viscous buckle folding as the dominant process explaining the furrow-and-ridge morphology characteristic for many rockglaciers. Buckle folding requires two main ingredients: mechanical layering and layer-parallel compression. In rockglaciers, the first is due to a layered ratio between ice and rock fragments. The second is due to the convex curvature of a rockglacier towards it toe. The associated slow-down leads to a compressive flow where curvature is largest. Our dynamical gravity-driven FE-model explains several first-order features of the Murtèl rockglacier: the amplitudes and wavelengths of the furrow-and-ridge morphology, the location of the largest-amplitude structures, and the parabolic flow profiles measured in boreholes. We estimate the time necessary to develop a furrow-and-ridge morphology as observed on the Murtèl rockglacier to be less than 1500 years.

References

Adamuszek, M., Schmid, D.W, and Dabrowski, M., 2011: Fold geometry toolbox – automated determination of fold shape, shortening, and material properties, Journal of Structural Geology, 33, 1406–1416.

Arenson, L., Hoelzle, M., and Springman, S., 2002: Borehole deformation measurements and internal structure of some rock glaciers in Switzerland, Permafrost and Periglacial Processes, 13, 117–135.

Frehner, M., 2011: The neutral lines in buckle folds, Journal of Structural Geology, 33, 1501–1508.

Frehner, M., Reif, D., and Grasemann, B., 2012: Mechanical versus kinematical shortening reconstructions of the Zagros High Folded Zone

(Kurdistan Region of Iraq), Tectonics, 31, TC3002.

Kääb, A., Gudmundsson, G.H., and Hoelzle, M., 1998: Surface deformation of creeping mountain permafrost. Photogrammetric investigations on rock glacier Murtèl, Swiss Alps, Collection Nordicana, 55, 531–537.

Maurer, H. and Hauck, C., 2007: Instruments and methods geophysical imaging of alpine rock glaciers, Journal of Glaciology, 53, 110–120.

Müller, J., Gärtner-Roer, I., Kenner, R., Thee, P., and Marche, D. 2014: Sediment storage and transfer on a periglacial mountain slope (Corvatsch, Switzerland), Geomorphology, in press.

Structural evolution and structural style of South Eastern Kohat deciphered through 3D geoseismic model using MOVE software, Shakardarra area, KP Pakistan

Humaad Ghani[1], Hamid Hussain[1], Muhammad Zafar[1], Irum Khan[1], Aamir Malik[2], Muhammad Abid[1], Ehtisham Javed[1]

[1] *Department of Earth & Environmental Science, Bahria University Islamabad*
[2] *Landmark Resources (LMKR),Jinnah Avenue, Blue area, Islamabad*
e-mail: *humaad.ghani@bahria.edu.pk, hammadtanoli@gmail.com*
session: *Tectonics and Surface Processes*

Abstract: Geologically Shakardarra is evolved through multiple episodes of deformation. In the current research structural evolution of south eastern Kohat is shown through 3D geoseismic model. It is prepared by integrating surface structural geological data and subsurface seismic reflection data. At surface doubly plunging anticlines and synclines are evolved on evaporites as detachment folds truncated by thrust faults along their limbs. In subsurface stratigraphic packages are marked on seismic sections based on regional stratigraphic studies and dominant reflections. The seismic data shows the thrust faults emanates from basal detachment located at sedimentary crystalline interface cutting up section to surface or lose their displacement to splay or back thrusts. At surface Shakardarra fault, Tolabangi fault, Chorlaki fault and axial trend of fold changes their strike from EW to NS which narrates that thrust and axial trend of folds are rotated along vertical axis by influence of Kalabagh strike slip fault. The current research suggests that Shakardarra is sequentially evolved in three episodes of deformation. In the first phase detachment folds developed on Eocene evaporites which are truncated by thrust faults emanating from basal detachment in second phase. In the third phase early formed folds and faults are rotated along vertical axis by the influence of Kalabagh fault.

Keywords: Structural Evolution, Detachment, Thrusting

Introduction

The Kohat Fold and Thrust Belt (KFTB) also known as Kohat Pleatue is an integral part of Himalayan Fold and Thrust System located in the Sub Himalayas. The KFTB extends from Main Boundary Thrust (MBT) in the north (Sarwar et al., 1979, Yeats et al., 1984, Coward et al., 1985) to Surghar range in the south (Ahmed et al., 1999). It is separated from its eastern counterpart Potwar Fold and Thrust Belt (PFTB) by Indus River and its western boundary is marked by Kurram Fault (Kazmi and Rana 1982). The KFTB and PFTB in their evolution are genetically related to Himalayan induced deformation (Ahmed, 1995 Ali, 1995 McDougal &Hussain, 1991 Abbasi and McElroy, 1991) in general and transpressional tectonics (Pivnik & Sercombe.,1994) in particular. However, Structural complexity is more pronounced in KFTB and the difference in structural style is attributed to the nature of decollment at base and secondary levels and role of strike slip faulting (Ahmed, 1995 Ahmed 2003 Ali, 1995 Dougal &Hussain, 1991 Abbasi and McElroy, 1991 Pivnik & Sercombe, Chen and Khan, 2010 Khan et al, 2012). Shakardarra is present at boundary of KFTB and PFTB with

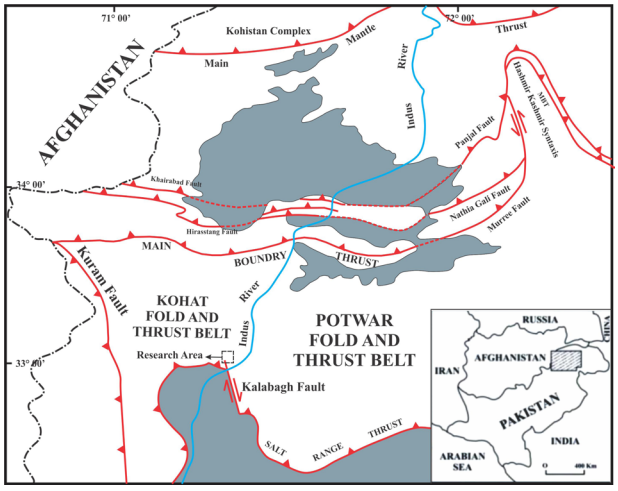

Fig. 1.: stratigraphic column of the study area

active Kalabagh strike slip present in south of it (figure 1). In the north of Shakardarra east-west trending structures change their orientation to north –south. The previous models (Abbasi., 1991, McDougall and Hussain., 1991) showed the lateral ramp in the subsurface causing the surface structures to change their orientation across it. Recent published work of (Khan et al 2012) on the nature and kinematics of Kalabagh fault shows its active nature and its presence as a lateral ramp in the northern part (Figure 1). The previous models developed had not taken the role of strike slip faulting in the deformational history as its presence in the near vicinity with still active nature cannot be avoided. The exposed structures at Shakardarra don't comply completely to the concept of lateral ramp. As the west vergence of thrust at the Hukni and continuation of these structures in north of Shakardarra with east-west trend are raising questions about the sole presence of lateral ramps in subsurface effecting the structures above.

Aim and Objectives

The aim of research is to understand structural evolution of the area in relation to fold and thrust kinematics and role of active strike slip faulting in reshaping the structures at surface and subsurface. The objectives are to prepare a 3 dimensional geoseismic model of the area to understand the genetic relationship between structures at surface and subsurface.

Methodology

Revised geological mapping of area at RF 1:50,000 by integrating published maps and field data. Seismic reflection data of 865-NK-02,05,08,11,15 are used for interpretation of subsurface structures, stratigraphy and depth to basement. Deformed geoseismic cross section are prepared by integrating surface geological, and seismic data in 2D move. 3D model is prepared in 3D move by integrating 2d cross sections, generating surfaces, ramps and fault planes to show the 3D structural geometries at surface and subsurface.

Stratigraphy and Tectonics

Kohat plateau is comprised of Eocene and younger sedimentary rocks and is located in the west of Potwar fold and Thrust belt. There are evaporates in the southern part of the plateau. In the northern region there are several thrust faults, synclinal folds and overturned folds. Low angle thrust faults are folded which are forming klippen. Evaporate sequence is missing or reduced in the northern part. Panobashales are present in the cores. There is E-W trending folds and reverse faults which are north and south dipping in the kohat plateau zone. Most of the faults are fault propagation folds. The Eocene sequence present in the Kohat plateau is very thick that is 300-500m. There are evaporates sequence in the central part of the Kohat plateau. The structures in the Shakardarra have an E-W orientation but it abruptly change direction E-W to N-S. Hukni fault which is a large thrust fault present in this area. (Figure 2)

Structural Geology

The structural geology of the research area is comprised of outcropping thrust faults and folds.

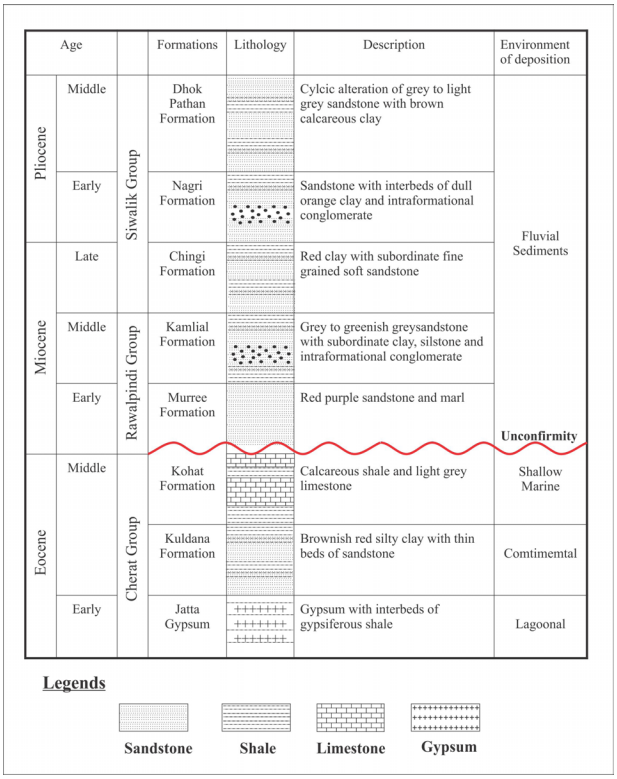

Fig. 2.: Tectonic map of northern Pakistan Showing major structural boundaries. The box shows the location of the project area

The general trend of the structures in the area is ENE-WNW. Fault bounded doubly plunging anticlines and broader synclines are present at the surface. Revised geological map of the area is prepared at 1:50,000 by integrating published geological map (Meissner,1974), and field orientation data (figure 3).

Seismic Interpretation

Seismic data is interpreted by solving velocity windows panels to obtain the average velocity. Time and depth of stratigraphic packages is calculated using these velocities.Eocene, Paleocene, Jurassic, Triassic and Permian Tops reflectors were marked. Basement was marked on 10 km by its presence as a prominent reflector on seismic lines. (Figure 4) It is also evident from previous research work ((Ahmed, 1995 Ahmed 2003 Ali, 1995 Dougal&Hussain, 1991 Abbasi and McElroy, 1991). Some outcropping faults are correlated to seismic shot point locations.

Cross sections

The cross sections are prepared manually by interpolation the surface geological data (contacts and orientations) and subsurface depth domain data of reflectors. The manually prepared reflectors are redrawn on 2D move software to maintain the accuracy for thickness of each horizon. Cross sections are later imported to Move for 3D model generation.

Section AB and CD

Both sections are north south orientated 17.5 km and 18.5 km in length.In north of section AB and CD, Nari banda fault (NRF), Bargazi banda fault (BBF) and Shakardarra fault (SF) are the thrust faults emanates from basal detachment to surface. Bab-e- Shakardarra fault (BSF) and two splay faults emanates at shallow depth in north and south of Shakaradarra fault. Eocene rocks are thrusted over younger rocks by these two thrust faults. In south of SF an open anticlinal and synclinal structure is transected by complex network of faults. In subsurface north facing thrust had uplifted the stratigraphic section toward north at deeper level. Tolabanghi khel fault and Chorlaki fault originates as south facing faults from north facing thrust at deeper level transects the limbs of folds. Triangular zones are formed at depth in between the opposite facing thrusts.

Section EF, GH, IJ & KL

Sections EF, GH and IJ are 27.1, 29.4 and 32.5 long orientated in NE-SW direction. Sections EF, GH, IJ are oriented oblique to the strikes of exposed structures, however section EF is east west oriented perpendicular to the strikes of structures. NRF is present in the EF section thrusting Eocene rocks over the Kamlial formation. SF is present in all sections thrusting Eocene rocks over the Kamlial and Nagri formations. NRF and SF

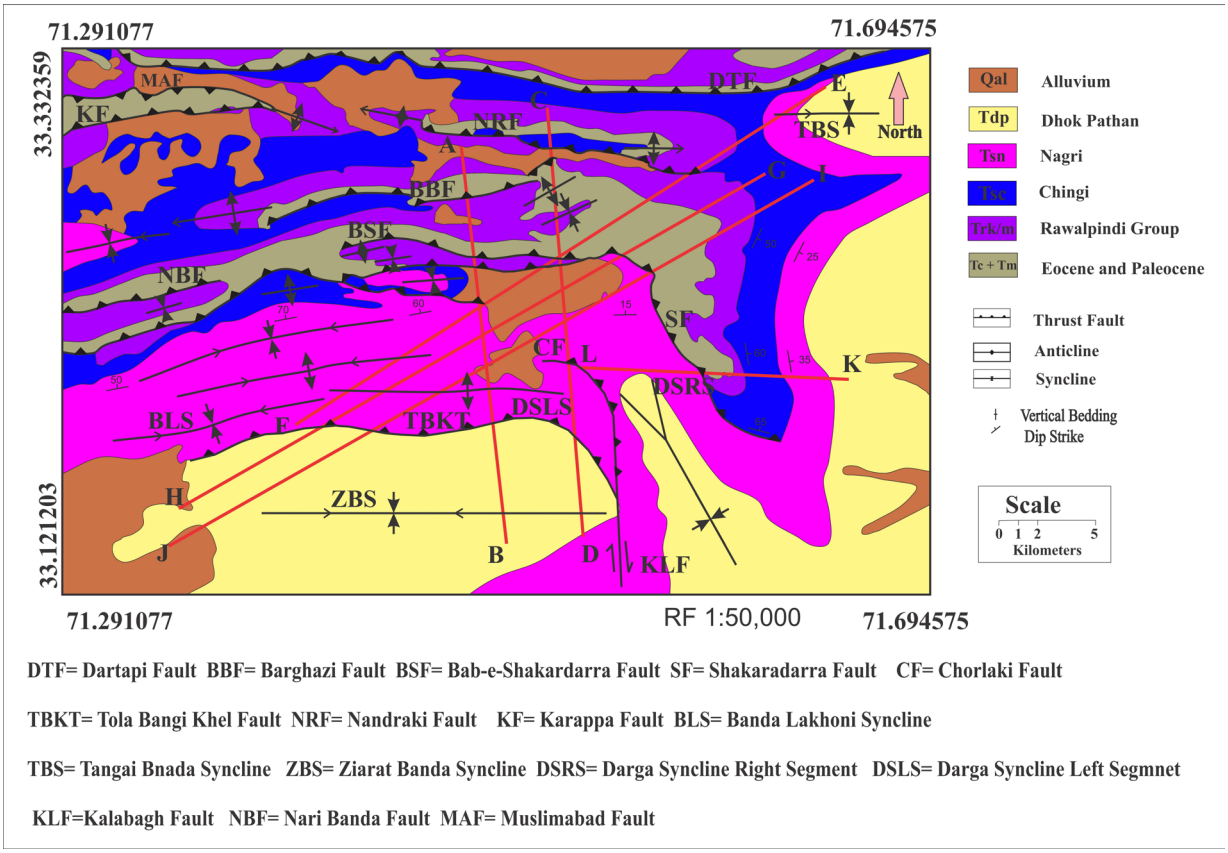

Fig. 3.: Tectonic map of northern Pakistan Showing major structural boundaries. The box shows the location of the project area

are cutting up section from basal detachments to surface. Tolabangi Khel fault in the sections GH and IJ is thrusting Nagri formation in the hanging wall over the Dhok Pathan formation in the foot wall. In subsurface Pop-up and triangle zones are present. In section KL steeply dipping Chorlaki fault (CF) is present with less stratigraphic throw. (Figure 5)

Discussion

Geologically Shakardarra is comprised of complex deformational structures, developed and modified by multiple deformational events. The structural models of area show the distribution of structures in 3 dimensional at surface and subsurface. Area is occupied by tight anticlinal structures in north and broader synclinal structures in south.The presence of Eocene Jatta gypsum in the core of anticlinal structures indicates that folds are formed as result of detachment folding on Eocene evaporites. The truncation of folds at limbs by faults narrates that faults are emplaced later in the deformational history of area than folds. The trends of folds axial traces and strikes of faults are ENE to WSW which indicates there development genetically linked to Himalayan induced deformation. The cross sections show that these faults are developed from basal detachment located at sedimentary crystalline interface. The cross section shows that back thrust are originated from fore-thrust at much shallower depths to achieve critical taper for initiation of fore thrust in south of it In the central portion of area south dipping blind thrust had uplifted the stratigraphic sequence northward in subsurface. TBKF and CF originate from these blind back thrusts cut up section to the surface. The faulting in the

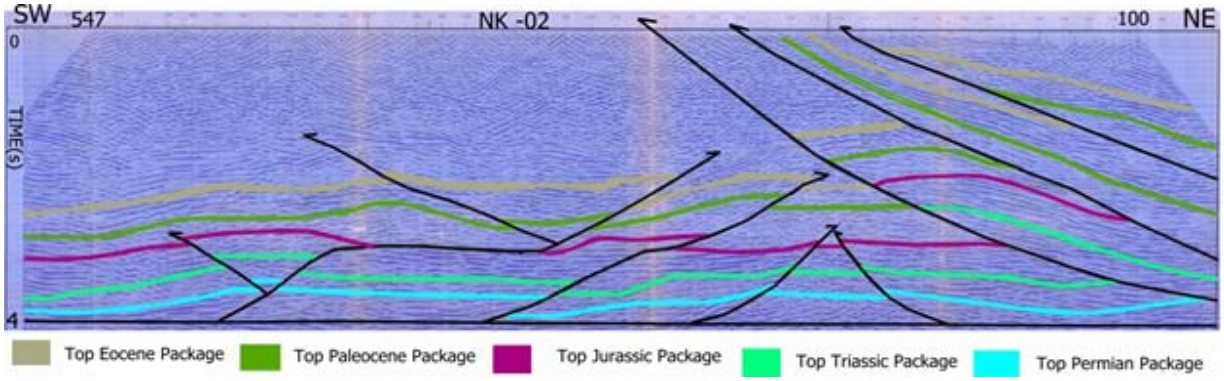

Fig. 4.: Interpreted Seismic Section 865-Nk-02

[!t]

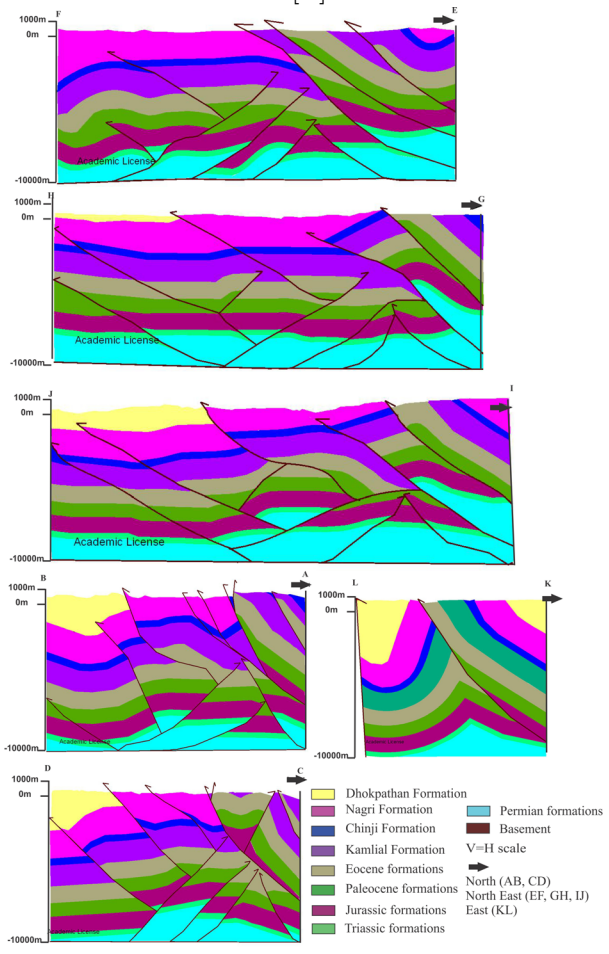

Fig. 5.: Geological Cross sections showing surface and subsurface geometries

central formation of study area is developed to achieve the critical taper for initiation of Surghar range frontal thrust in south of shakardarra. The structural geology of area in central portion is comprised of pop-up and triangle zone geometries in subsurface. The reservoirs formations of Jurassic age are structurally uplifted and transected by these faults forming the structures favorable for exploration of hydrocarbon. The change in orientation of Shakardarra fault, Tola bangi khail fault and Chorlaki fault from E-W to N-S in the eastern portion of area is strongly influenced by right lateral movement of Kalabagh fault present in south east of this area. Dominant flexure/bends in the strikes of Surghar range thrust in west of Kalabagh fault and Shakardarra fault in east represents that the early formed thrusts are rotated along the vertical axis of rotation related to kalabagh strike slip fault. The deformation related to Kalabagh strike slip fault had changed the orientation and dips of Nagri formation to vertical near the rotated fault plane of Chorlaki fault and Tola bangi khail fault. The research suggests that area is evolved sequentially in three episodes of deformation. In first phase of deformation folding is developed on Eocene evaporate horizons as detachment folds. In second phase of deformation thrusting from basal detachment had truncated the folded structures and elevated the whole stratigraphic sequence. In third phase of deformation early formed thrust faults are rotated from EW to NS by the influence of Kalabagh strike slip fault. (Figure 6)

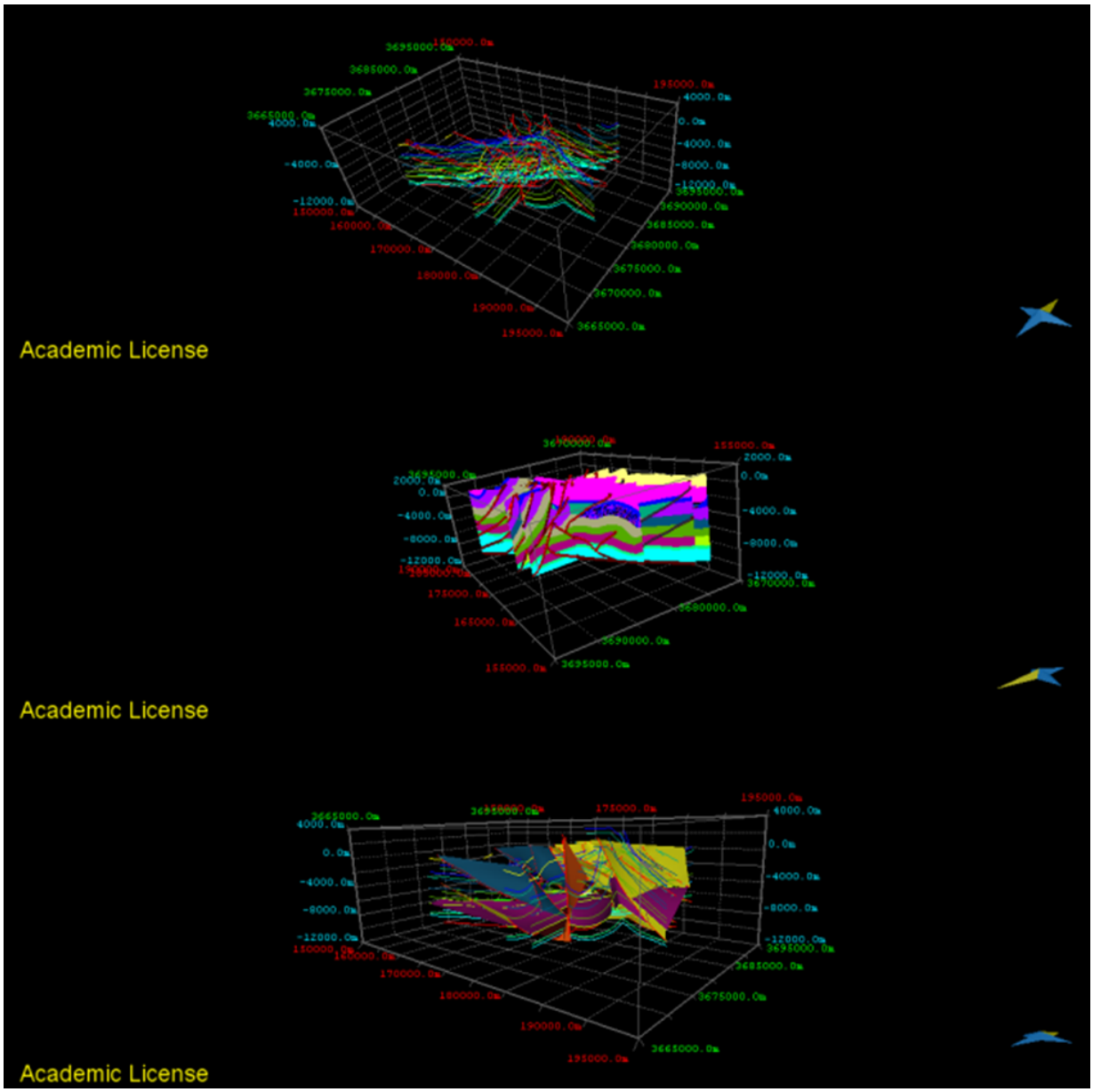

Fig. 6.: 3d models showing complete fault pattern and integration of 2d into 3d

Conclusions

The current research had concluded following points

1. Two distinctive detachment horizons are present in the subsurface at sedimentary crystalline interface and Eocene evaporates sequence.
2. The general trend of faults and folds is ENE-WSW which shows their genetic link to Himalayan induced deformation.
3. The truncations of fold limbs by faults indicate that faults are emplaced later in deformational history of area than folds.
4. The back thrusts in the area are developed to achieve the critical taper for initiation of fore thrust towards south.
5. The change in strikes of shakardarra fault, surghar range thrust, Tola bangikhel fault and chorlaki fault indicates that these early formed thrust are rotated along vertical axis by the influence of Kalabagh strike slip fault.
6. The area is evolved sequentially in three episodes of deformation, detachment folding followed by thrusting superimposed by strikeslip faulting.

References

Abbasi, I.A., and McElroy, R., 1991. Thrust kinematics in the Kohat Plateau, Trans Indus Range, and Pakistan J. Of Struct. Geol, Vol. 13, No. 3, p.319-327.

Ahmad, D., 1995. Tectonic analysis of Southern Kohat plateau, N.W.F.P., Unpublished M Phil thesis, NCEG, University of Peshawar.

Ahmed, S., 2003. A comparative study of structural styles in Kohat plateau, NW Himalayans, NWFP, Pakistan. PH.D thesis, NCEG, University of Peshawar.

Ahmed, S., Ali, F., Sayab, M., Ahmed, I., Hamidullah, S., 1999. Structural geometry of the Himalyan frontal Thrust zone: Surghar range, Pakistan. Geological Bulletin, University of Peshawar 32, 13-23

Ali, F., (1995). Imprints of transpressional deformation on southern Kohat Plateau, Karak area, NW Himalayas, NWFP, Pakistan. Geol. Bull. Univ. Peshawar, Vol.33, pp.87-95

Chen, L., Khan , S.D., 2010. InSAR observations of the strike slip faults in the NW Himalyan frontal Thrust system. Geosphere 6, 731-736.

Coward, M.p., Butler, R.W.H., 1985. Thrust Tectonic and the deep structure of the Pakistan Himalayan. Geology, 13:417-420

Khan, A. A., 1999. Structure and tectonic setup of the area, south and southwest of Kohat, N.W.F.P., Pakistan. Unpublished M.Phil thesis, NCE in Geology, University of Peshawar.92p.

Mc Dougal, J.W., and Hussain, A., 1991. Fold and thrust propagation in the western Himalaya based on a balanced cross section of the Surghar range and Kohat plateau, Pakistan. American association petroleum Geologists, bulletin, 75. 463-478.

Meissner, C. R., Master, J.M., Rashid, M.A. and Hussain M., 1974. Stratigraphy of Kohat quadrangle, Pakistan. United States Geological Survey professional paper, 716 D.

Pivnik, D.A., and Wells, N.A., 1996. The translation from Tethys to the Himalaya as recorded in Northwest Pakistan, Geological Society of America Bulletin, v.108, p.1295- 1311.

Sarwar, G and Dejong, K.A., 1979. Arcs, oroclines, syntaxes- the curvatures of Mountain Belts in Pakistan.

Yeats, R.S and Lawrence, R.d., 1984. Tectonics of the Himalayan thrust belt in northern Pakistan.

Lithospheric scale analogue models of the southern Gulf of California oblique rift

Diego Gracia-Marroquín[1], Rodrigo Portillo-Pineda[2], Mariano Cerca[3], Giacomo Corti[4]

[1]*Posgrado en Ciencias de la Tierra, Centro de Geociencias, Universidad Nacional Autónoma de México, Blvd. Juriquilla, 3001, 76230, Juriquilla, Querétaro, México*
[2]*PEMEX Exploración y Producción, Activo de Exploración de Cuencas del Sureste, Coordinación de Modelado Geológico Regional, Edificio Administrativo, primer piso ala poniente, Región Marina Sureste, Calle 33, 90, Colonia Burócratas, Ciudad del Carmen, Campeche C. P. 24179*
[3]*Laboratorio de Mecánica de Geosistemas, Centro de Geociencias, Universidad Nacional Autónoma de México, Blvd. Juriquilla, 3001, 76230, Juriquilla, Querétaro, México*
[4]*Consiglio Nazionale delle Ricerche (CNR), Istituto di Geoscienze e Georisorse, U.O. Firenze, Via G. La Pira, 4, 50121 Florence, Italy*
e-mail: *diegograciam@geociencias.unam.mx*
session: *Tectonics and Surface Processes*

Introduction

The rift of Gulf of California represents an exceptional case of oblique rifting where incipient seafloor spreading is occurring (Lizarralde et al., 2007; Sutherland et al., 2012). This rift is characterized by a dextral movement which has an angle of ∼20° between the transform zone in the center of the Gulf of California and the Baja California peninsula (Stock & Hodges, 1989; Fletcher et al., 2007). Analogue models reproducing oblique rifting, which is characterized by a relative displacement between two tectonic blocks with an angle with respect to the rift axis of less than 90° (Agostini et al., 2009; Autin et al., 2010), have found that, among other factors, the obliquity might be a consequence of the presence of a pre-existing oblique lithospheric weakness zone both in the crust and in the mantle. The influence of pre-existence weak zone is believed to help to localize the deformation causing rifting.

In order to investigate some aspects of the evolution of deformation of the GoC oblique rifting a series of astenospheric-scale analogue models were carried out. The experiments consider a central zone of weakened rheology. The objectives of this study are to analyze the geometry of fault patterns in the southern Gulf, to reproduce the deformation between Baja California (Baja) and Sierra Madre Occidental (SMO) blocks (figure 1), and finally to remark some similarities between model and the southern part of the Baja California rift.

Experimental Setup

The models were built at the Laboratorio de Modelado Analógico, Centro de Geociencias, UNAM. The suitability of cold lithosphere physical models for studying rifting has previously been tested by Autin et al. (2010). In our experiments, the model lithosphere consist of four layers: a) upper brittle crust, composed by a mixture of hollow and dense glass microspheres; b) lower ductile crust, made by mixing silicone, corundum sand, and plasticine (100:30:10); c) lithosphere mantle, composed by a mixture of silicone, dry quartz sand, and plasticine (80:100:25) and, d) the astenosphere, made by glycerin and gypsum. The materials flow curves and density were properly scaled with respect to natural values. The model lithosphere floats on the astenosphere,

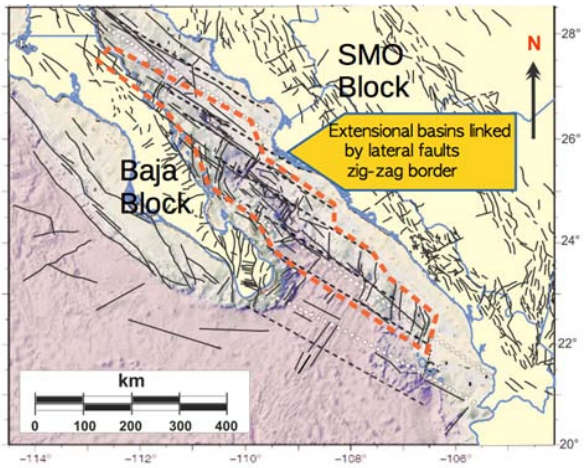

Fig. 1.: Geometry of fault patterns in the southern Gulf of California. The zone located in the central part of the GoC has a "zig-zag" geometry defined by normal and lateral faults, these features might have an influence on the faults observed in the edge of the Baja California and Sierra Madre blocks localizing deformation and forming border faults.

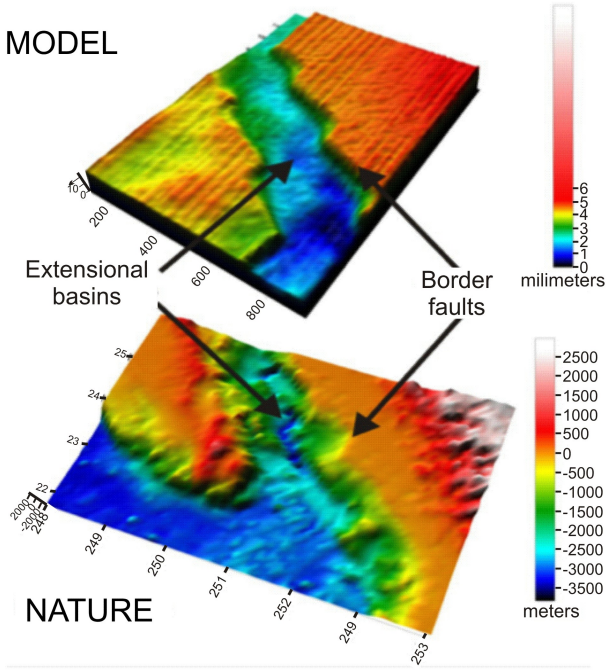

Fig. 2.: Digital elevations models of the experiment and the southern GoC.

which is a high density and high viscosity material. A weakness zone was built as a band in the middle of the model that corresponds to the position of the Gulf of California, reducing the viscous resistance of the lower crust and the lithosphere mantle by adding oleic acid (10%) to the mixtures.

The low resistance band divided the model into a fixed block (Mexico mainland) and a mobile block (Baja California) and they were built in a plexiglass box with dimensions 40x40 cm^2. The angle of the weak zone with respect to the direction of displacement was about 20°, corresponding to the angle among the proposed displacement of the Baja California Block with respect to the mean rift axis (e. g., Fletcher et al., 2007). Deformation of the experiments surface was recorded by plain view images and its digital topography was obtained by using the Zebra software.

Results

The model reproduces the general topographic features of the Gulf of California narrow rifting including the "zig-zag" geometry of the border faults and the individual extensional basins along the rift axis (Figure 2). In the analogue models it is not possible to reproduce the continental rupture and adding of material and thus is pertinent only for the pre-rupture Miocene to Pliocene (∼12 to 3 Ma) history of the rift. However, we consider that the geometry of the transform system in the gulf is a consequence of the progressive previous history and it does not alter the border faults geometry and the discussion about the location and migrations of the depocenters sustains. Our model focus in reproducing the geometry of the rift and does not consider the causes of such geometry. However, it has been suggested that the Gulf of California narrow rift evolution is the continuation of a long history (more than 30 Ma) of widespread extension in the western North American plate (Ferrari et al., 2013). A probable cause of the "zig-zag" geometry of the border faults and the presence of a weaker lithosphere localizing deformation is the rift segmentation that occurred in previous extension episodes (Axen, 1995). The conclusion is that the initial geometry of the bor-

der faults has an important influence leading to the geometry of the transform system after the continental rupture.

In Figure 3 we present the evolution of three topographic profiles with an orientation perpendicular to the experimental rift axis to visualize differences in the evolution of the rifting with extension. In the three cases, the model reproduces the observation of a westward migration of the extensional basins activity (Aragon-Arreola and Martin-Barajas, 2007).

The width of the extension zone confined within the weaker band is prescribed by the model set up but there are significative variations in the depocenter depths along the rift axis. Greater asymmetry is observed at the northern part of the model. Extension localizes initially at the SMO block and progressively migrates to be closer to the Baja block. Modeling reproduces suitably the migration of depocenters.

References

Agostini, A., Corti, G., Zeoli, A., Mulugeta, G., 2009, Evolution, pattern and partitioning of deformation during oblique continental rifting: Inferences from lithospheric-scale centrifuge models: Geochemistry Geophysics Geosystems, v. 10, Q11015, doi:10.1029 /2009GC002676.

Aragón-Arreola, M., Martín-Barajas A., 2007, Westward migration of extension in the northern Gulf of California: Geology, v. 35(6), p. 571–574. Autin, J., Bellahsen, N., Husson, L., Beslier, M. O., Leroy, S., d'Acremont, E., 2010, Analogue models of oblique rifting in a cold lithosphere: Tectonics, 29, TC6016, doi:10.1029/2010TC002671.

Axen, G., 1995, Extensional segmentation of the Main Gulf Escarpment, Mexico and United States: Geology, v. 23, p. 515–518.

Ferrari, L., López-Martínez, M., Orozco-Esquivel, T., Bryan, S. E, Duque-Trujillo, J., Lonsdale, P.F., 2013, Late Oligocene to middle Miocene rifting and syn-extensional magmatism in the southwestern Sierra Madre Occidental, Mexico: the beginning of the Gulf of California rift: Geosphere, v. 9, n. 5, p. 1161-1200

Fletcher, J. M., Grove, M., Kimbtrough, D., Lovera, O., Gehirels, G., 2007, Ridge-trench interactions and the Neogene tectonic evolution of the Magdalena shelf and southern Gulf of California: Insights from detrital zircon U-Pb ages from the Magdalena fan and adjacent areas: Geological Society of America Bulletin, v. 119, p.1313–1336.

Lizarralde, D., Axen, G. J., Brown, H., E., Fletcher, J. M., Gonzales-Fernandez, A., Harding. A., J., Holbrook, W, S., Kent, G, M., Paramo, P., Sutherland, F., Umhoefer, P, J., 2007, Variation in styles of rifting in the Gulf of California: Nature, v. 448, p. 466-469.

Stock, J. M., & Hodges, K. V., 1989, Pre-Pliocene extension around the Gulf of California and the transfer of Baja California to the Pacific Plate: Tectonics, v. 8, p. 99–115.

Sutherland, F. H., Kent, G. M., Harding, A. J., Umhoefer P. J., Driscoll, N. W., Lizarralde, D., Fletcher J. M., Axen G. J., Holbrook, W. S., González-Fernández A., Lonsdale P., 2012, Middle Miocene to early Pliocene oblique extension in the southern Gulf of California: Geosphere 2012;8;752-770 doi: 10.1130/GES00770.1

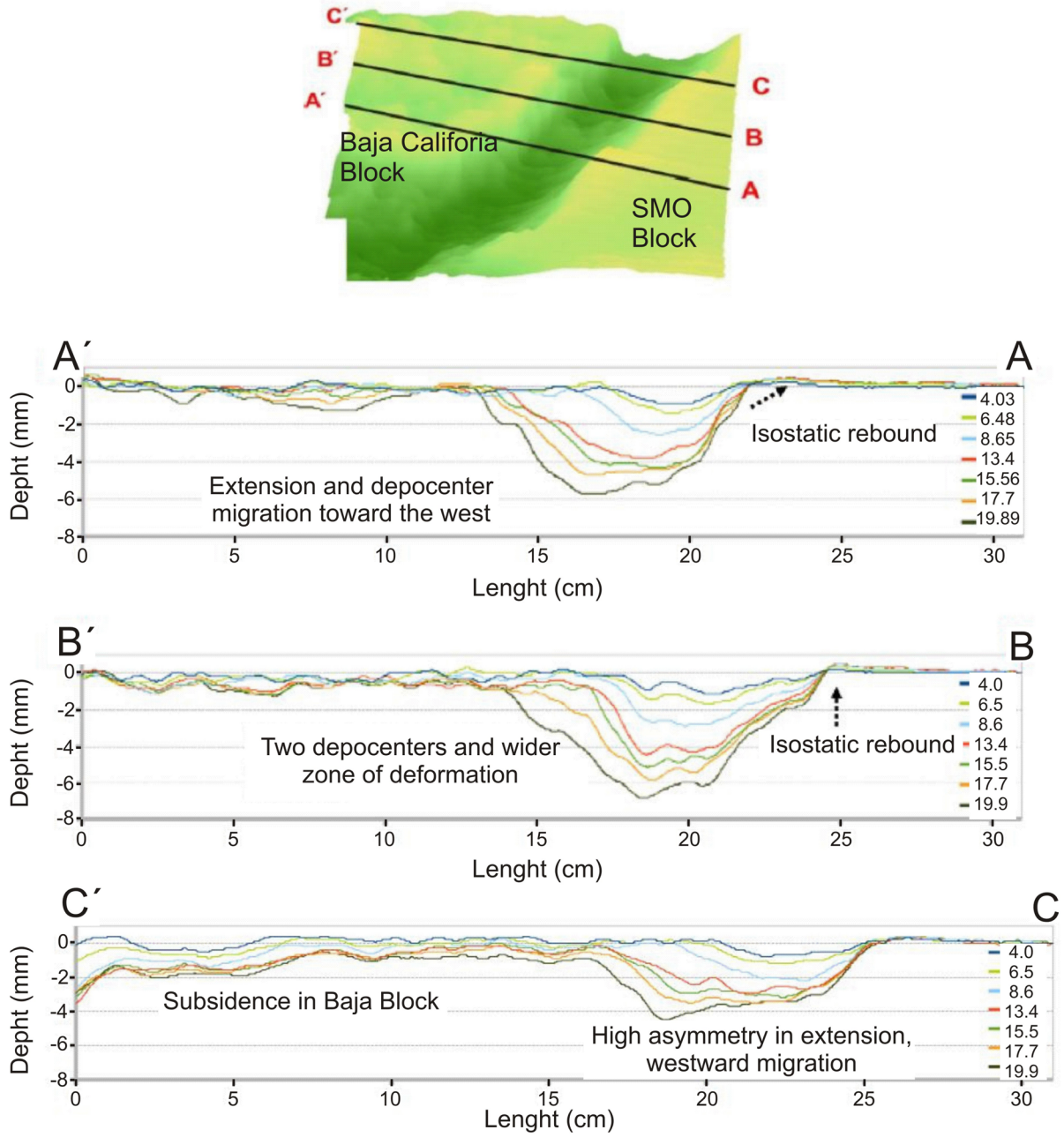

Fig. 3.: Topographic sections of the model showing the differences in depocenter evolution along the rift axis. In the three cases presented the depocenter migrates westward with differences in the symmetry of the rift. The depocenter locates closet to the moving block.

The negative inversion of thrust faults and related basin geometries: insight from analogue modelling experiments

Fabien Graveleau[1], Olivier Averbuch[1], Bruno Vendeville[1], Aimie Quinion[1], Mustapha Ouzgaït[1]

[1] *Université Lille 1, CNRS UMR 8217, Géosystèmes, Avenue Paul Langevin, F59655 Villeneuve d'Ascq, France*
e-mail: *Fabien.Graveleau@univ-lille1.fr*
session: *Tectonics and Surface Processes*

The extensional reactivation of thrusts (i.e. the negative tectonic inversion process) has often been suggested as a major deformational mechanism in post-orogenic sedimentary basins and rifted margins. The recognition of this negative tectonic inversion process is generally based on combined structural features including the collapse of major thrust-related structural relief, the collapse of the backlimb of thrust-related folds, the development of post-orogenic syn-rift deposits upon the crest of previously developed ramp-related anticlines and the general parallelism of extensional and compressional structures in map view. The direct relationships between normal faults and the underlying thrusts are however rarely exposed due to the general burial of these structures below a sedimentary cover controlled by the tectonic subsidence. Seismic profiles across post-orogenic basins generally does not allow providing, at depth, a precise image of such relationships due to the overall structural complexity.

To give further insight into this mechanism, and provide a guide for structural and seismic interpretation at depth in basins controlled by the extensional reactivation of basement thrust faults, a set of analogue modelling experiments have been conducted. Modelling of the negative tectonic inversion process has been rarely considered conversely to the positive inversion that has been the object of numerous studies. Basically, our models involve a brittle, cohesionless, dry, porous 3 cm-thick sand unit overlying a basal 1 cm-thick silicone layer designed to localize the basal décollement of the deformed structures. All models, initially 110 cm long and 49 cm large, were built above a flat, horizontal, rigid base. The entire model was first subjected to a phase of shortening by moving progressively at a constant speed (0.5 cm/hour) the left-hand wall until a value of about 39% bulk shortening was reached (87 hours of shortening). An orogenic wedge formed against the moving wall, then propagated progressively rightward by formation of new forethrusts and by bulk thickening of the wedge itself. At the end of compression episode, a post-tectonic sand layer was deposited to bury completely the structural relief and generate a horizontal datum for the next extensional phase Experiments were then tilted hinterlandward to simulate a flexural response of the lithosphere to orogenic loading. For the extensional phase of the experiment, two different basal slopes were tested (2.5° and 5°) to investigate the influence of internal thrust dips on the extensional dynamics. Models were extended by moving backwards the mobile sidewall at a speed of 1 cm/hour. As extension proceeded, the horizontal post-compression datum subsided locally along fault-bounded grabens that were incrementally filled-up with sand layers simulating the syn-rift deposits. At the end of each experiment, models were cut along equidistant vertical cross-sections and integrated as a 3D structural model using Move®. geomodelling software (Mid-

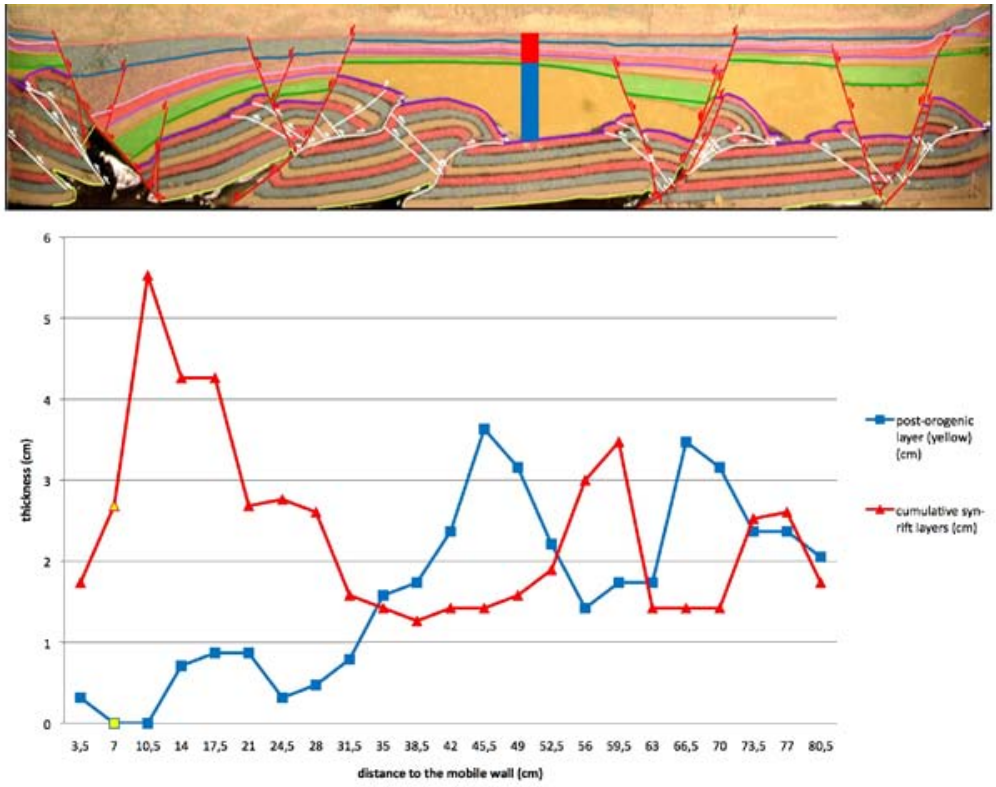

Fig. 1.: Cross-sections across the centre of the models illustrating the relationships between the basin geometry, the normal faults and the underlying thrust structures.

land Valley Ltd). Some representative sections were restored at the main steps of the basin development to provide a progressive view of the structural evolution of the basin.

Results of modelling experiments (Fig. 1) give a new insight into the geometries and kinematics of the negative tectonic inversion process, and allow further discussion on the main parameters controlling the reactivation of basement thrusts during a subsequent extension. They particularly emphasize the characteristic geometric and kinematic features of post-orogenic basin development, and especially, argue for the ramps of fore- and backthrusts to localize at depth respectively the master normal faults controlling depocenters and some antithetic secondary faults accommodating the adjustment of the hangingwall over the basal thrust surface.

Experimental modelling of deformation-erosion-sedimentation interactions in compressional, extensional and strike-slip settings

Fabien Graveleau[1,5], Vincent Strak[2], Stéphane Dominguez[3,5], Jacques Malavieille[3,5], Marina Chatton[3], Isabelle Manighetti[4], Carole Petit[4]

[1] *Université Lille 1, CNRS UMR 8217, Géosystèmes, Avenue Paul Langevin, F59655 Villeneuve d'Ascq, France*
[2] *School of Geosciences, Monash University, Melbourne, Victoria, Australia*
[3] *Université Montpellier 2 – CNRS UMR 5243, Géosciences Montpellier, CC 60, Place Eugène Bataillon, F34095 Montpellier, France*
[4] *Université de Nice Sophia-Antipolis, CNRS UMR 7329, Géoazur, Observatoire de la Côte d'Azur, La Darse, BP 48, 06235 Villefranche-sur-mer, France*
[5] *International Associated Laboratory ADEPT, CNRS- NSC, France-Taiwan*
e-mail: *Fabien.Graveleau@univ-lille1.fr*
session: *Tectonics and Surface Processes*

Tectonically controlled landforms develop morphologic features that provide useful markers to investigate rates of tectonic deformation and mechanisms of relief growth. In this work, we review results of morphotectonic experiments obtained with an innovative approach combining tectonic deformation and surface processes, coupled with accurate measurement techniques. This allows for a qualitative and quantitative analysis of landscape evolution associated with active deformation achieved through compressional, extensional and strike-slip tectonic settings (Fig. 1).

Major results indicate first that experimental morphologies evolve significantly at a short time scale (several seconds to tens of minutes, which scales about to 1 – 500 kyr), suggesting that morphogenetic processes have a short time response to tectonic and climatic forcing. For compressional settings, the formation of alluvial terraces above an active thrust is controlled by regular incision of the main channel through the uplifting hanging wall and by avulsion of deposits on fan-like bodies. Deformation of terraces well records the growth of the structure. For extensional settings, the dynamics of hanging-wall sedimentary filling controls the position of the base level, which in turn controls footwall erosion. Two phases of relief evolution are recognized: the first is a phase of relief growth and the second is a phase of upstream propagation of topographic equilibrium reached primarily in the sedimentary basin. During the phase of relief growth, the formation of triangular facets occurs by degradation of the fault scarp and their geometry (height) becomes stationary during the phase of topographic equilibrium propagation. For strike-slip settings, the complex geometry of the wrench zone, composed of several interacting fault segments, enhances the interactions with the drainage network. Consequently, numerous morphologic markers form continuously, but their lifetime is generally short due to erosion. A significant amount of distributed deformation is also observed along the fault zone. Locally, less than a quarter of the far field displacement can be measured using fault offsets, leading to a systematic underestimation of the real fault slip rate.

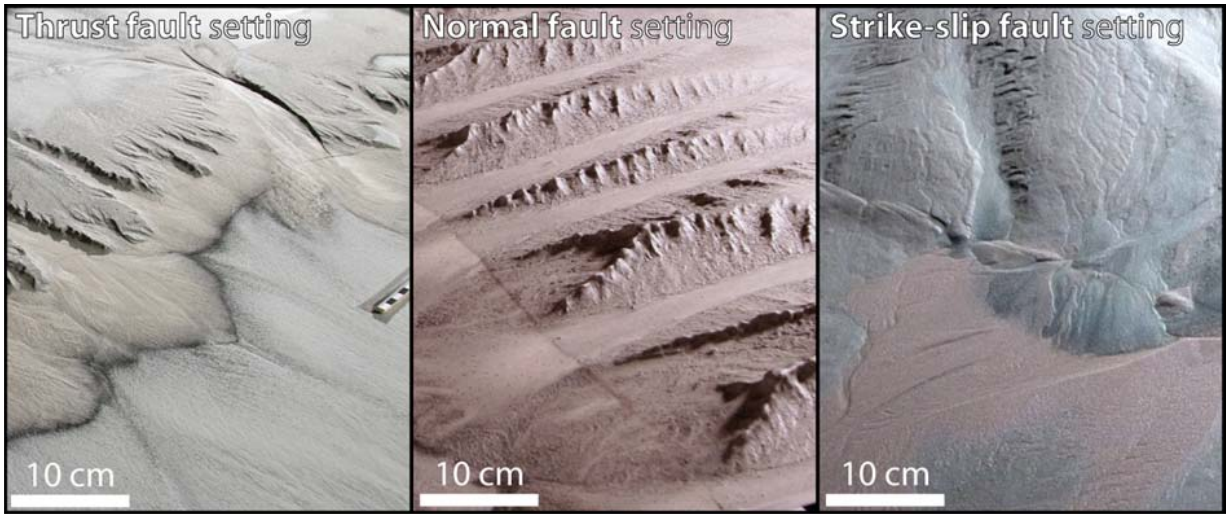

Fig. 1.: Experimental modelling results of landscape dynamics along an active A) thrust fault, B) normal fault, and C) Strike-slip fault. Note the modelling of morphotectonic markers such as fault scarps, faceted spurs, alluvial terraces, restraining bends and pressure ridges.

The experimental approach coupling deformation mechanisms and erosion-transport-sedimentation processes is well adapted to study the morphologic evolution of diverse tectonically controlled landforms.

Linking lithosphere deformation and sedimentary basin formation over multiple scales

Ritske .S. Huismans[1]

[1]*Department of Earth Science, University of Bergen, Allégaten 41, N-5007 Bergen, Norway*
e-mail: *ritske.huismans@geo.uib.no*
session: *Tectonics and Surface Processes*

Here we focus on the relationships between tectonic deformation and sedimentary basin formation. Resolving the interaction and feedback between tectonic crust-lithosphere scale deformation and surface processes through erosion of elevated areas and formation of sedimentary basins over multiple scales has been a long-standing challenge. While forward process based models have been successful at showing that a feedback is expected between tectonic deformation and redistribution of mass at the earth's surface by erosion, transport, and deposition, demonstrating this coupling for natural systems has been an even greater challenge and is strongly debated. Observational constraints on crust-lithosphere deformation and surface processes are typically collected at highly varying spatial and temporal scales, while forward process based models are typically run at either very large lithosphere-mantle scale, or at the scale of the sedimentary basin making it difficult to investigate and explore the detailed interaction and feedback between these systems. Here I will report on recent advances in forward modelling linking crust-lithosphere deformation with surface processes over a large range of scales resolving tectonic plate scale deformation and sedimentary basin formation at stratigraphic scales. The forward numerical models indicate a linkage and interaction between the structural style of thick-skinned large-scale mountain belt and rift-passive margin formation, erosion-transport-deposition processes operating at the surface, and the thin-skinned deformation occurring in the associated sedimentary basins.

3D Analogue Modelling of the Effect of Fan Sedimentation on Accretionary Wedge Dynamics – the Magdalena Fan case, South Caribbean Margin, Colombia

Karen Leever[1], Elisabeth Johansen[2]

[1] *Deutsches GeoForschungsZentrum GFZ Potsdam, Germany*
[2] *Department of Petroleum Engineering, University of Stavanger, Norway*
e-mail: *karen.leever@gfz-potsdam.de*
session: *Tectonics and Surface Processes*

Introduction

Surface processes are well known to influence deformation in mountain belts and accretionary wedges. Erosion and sedimentation influence vertical motions (exhumation) and wedge geometry (number of faults and total strain accumulated on them) by redistribution of material. Critical taper theory has been successful in explaining the interaction between tectonics and surface processes in brittle wedges.

In terms of this interaction, the Magdalena Fan on the active South Caribbean margin in Colombia is a feature of particular interest. The Caribbean plate has subducted beneath north western South America since at least Eocene times and as a result, a long and wide accretionary prism has developed. One of the world's most sediment rich rivers, the Magdalena River has deposited its sediments on top of this accretionary wedge since the Middle Miocene. The resulting Magdalena Fan is a very prominent feature in the bathymetry of the continental slope. Thrusts in the wedge curve into the fan on both sides, creating a convex-outward shape in map view. Moreover, while thrusts are easily recognized on seismic sections in the wedge, no deformation is obvious on seismic sections inside the fan.

In previous studies, the curvature of the accretionary wedge has been explained both as a primary feature, due to curvature of the margin, and as a secondary feature, caused by loading by the Magdalena Fan. In this study, we test the latter hypothesis and investigate the role of strong syn-tectonic sedimentation from a point source. Could localized sedimentation lead to curvature of the accretionary wedge? How is deformation partitioned between the accretionary wedge and the fan and, in particular, how and where is deformation accommodated inside the fan? We address these questions by means of coupled 3D analogue modelling, in which we vary the sediment flux from a point source while tectonic accretion occurs at a constant rate.

Modeling strategy and setup

In a series of 3D scaled analogue models (1:10^5), we varied the sediment flux S while the tectonic accretion rate A was kept constant (Table 1), resulting in different S/A ratios.

We used a box of 80cm wide and 100cm length, with a high friction conveyor belt at the base, glass side walls and a vertical back wall. A 2cm thick layer of quartz sand was sieved onto the conveyor belt, representing the sediments on the incoming plate. An initial sand wedge was sieved against the back wall. Syn-tectonic sedimentation at different rates was achieved by pouring glass beads through a funnel connected to a gutter suspended above the deforming wedge in the middle of the back wall at regular time intervals (Table 1). Total shortening was 40cm.

Model	Model ID	Tot. displ. (mm)	Sedimentation rate	S (mm^3/s)	H (mm)	V (mm/s)	A (mm^3/s)	S/A
A	3D_50_4c	400	10 ml / 20 s	500	20	0.25	1000	1/2
B1	3D_50_4d	400	20 ml / 20 s	1000	20	0.25	1000	1
B2	3D_50_3e	500	20 ml / 10 s	2000	20	0.5	2000	1
C	3D_50_4b	400	40 ml / 20 s	2000	20	0.25	1000	2
D	3D_50_4e	400	90 ml / 20 s	4500	20	0.25	1000	4.5
–	3D_50_4a	400	45 ml / 20 s	2250	10	0.25	500	4.5

Tab. 1.: Model parameters. S is sediment flux; H thickness of the incoming layer, V displacement rate of conveyor belt. Tectonic accretion rate A was calculated by integrating the cross sectional material flux H*V over a domain of 20 cm width.

Materials were chosen such that the angle of repose of the sediment (given by its coefficient of internal friction) is similar to the slope angle of the critically tapered wedge (a function of basal and internal friction). Thus we used quartz sand ≤ 0.3 mm ($\mu = 0.75$) for the deforming sediment on the incoming plate and glass beads of 0.2-0.3 mm ($\mu = 0.5$) mixed with 10%vol colored sand for the fan sediment. The high friction base leads to $\mu b = \mu$ in the deforming wedge.

The experiments were monitored at short time intervals with high resolution digital cameras. At the end of each experiment, the model was covered and moisturized and cross sections were sliced at 2-5cm intervals.

Preliminary results

1. Loading by fan sediments forces the frontal thrust forward, such that it breaks the surface in front of (around) the fan (Figure 1).

2. Different modes of fault formation and slip partitioning occur depending on the sediment flux (Figure 1):
   - for low S/A ratios (S/A = 0.5), the new frontal thrust forms as a single fault along the wedge and curved around the fan;
   - in the intermediate case (S/A = 1) there is a small delay between the formation of a new thrust in front of the wedge (initially curving into the fan) and the one around the fan;
   - high S/A ratios (S/A >= 1) lead to prolonged lifetime of faults (and thus fewer faults) below the fan: underthrusting continues below the fan even as a new fault is formed in front of the wedge. This phenomenon may be enhanced by the lubricating effect of the (low friction) fan sediments. The newly formed faults in front of the wedge do not run straight but curve into the fan.

3. The structural evolution of the wedge proves to be sensitive also to the position of the sediment load (Figure 2): sediments deposited in a more distal /frontal position (prograding system, model B2) lead to duplex formation and associated uplift in the rear of the wedge below the fan and prolonged activity of the faults below the fan. For an aggrading or retrograding system a higher sediment flux (S/A ratio) is required to obtain the same effect (model B1, C)

4. Tectonics in return influences sedimentation: hanging wall uplift leads to backward tilt of fan, restricting sedimentation to the hanging wall of the active fault for some time and

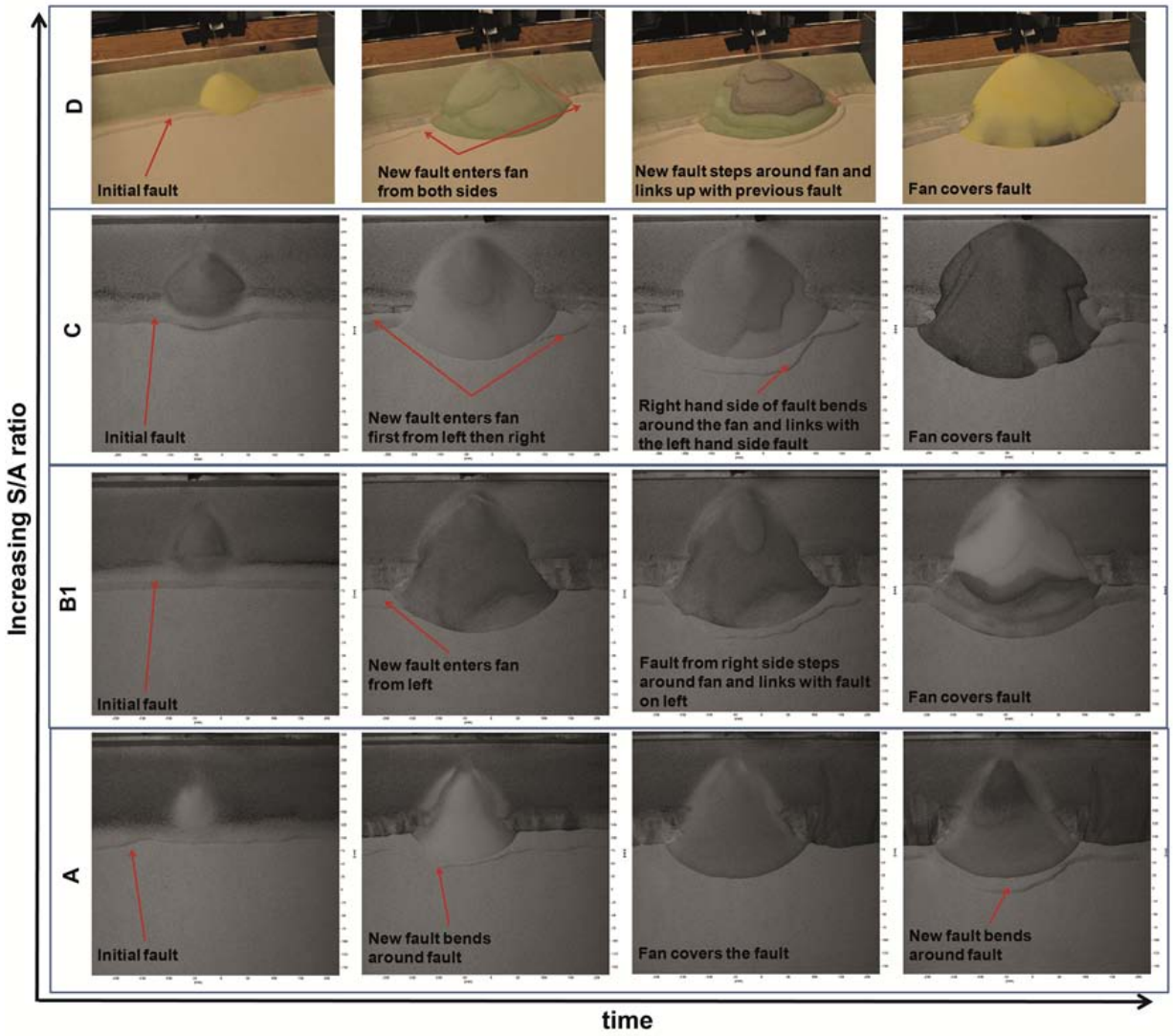

Fig. 1.: Differences in structural evolution in Model A-D (top view) as a function of increasing S/A ratio (Table 1). Horizontal time axis shows increase of time, but not the same time for the different models.

leading to locally higher sedimentation rates (Figure 1D, 2D). Aggradation and progradation are thus tectonically controlled in our subaerial models.

5. Fan sediments are strongly deformed by fault-bend folding in front of the active thrusts, but undeformed on the tectonically inactive part of the wedge (upper slope, Figure 2).

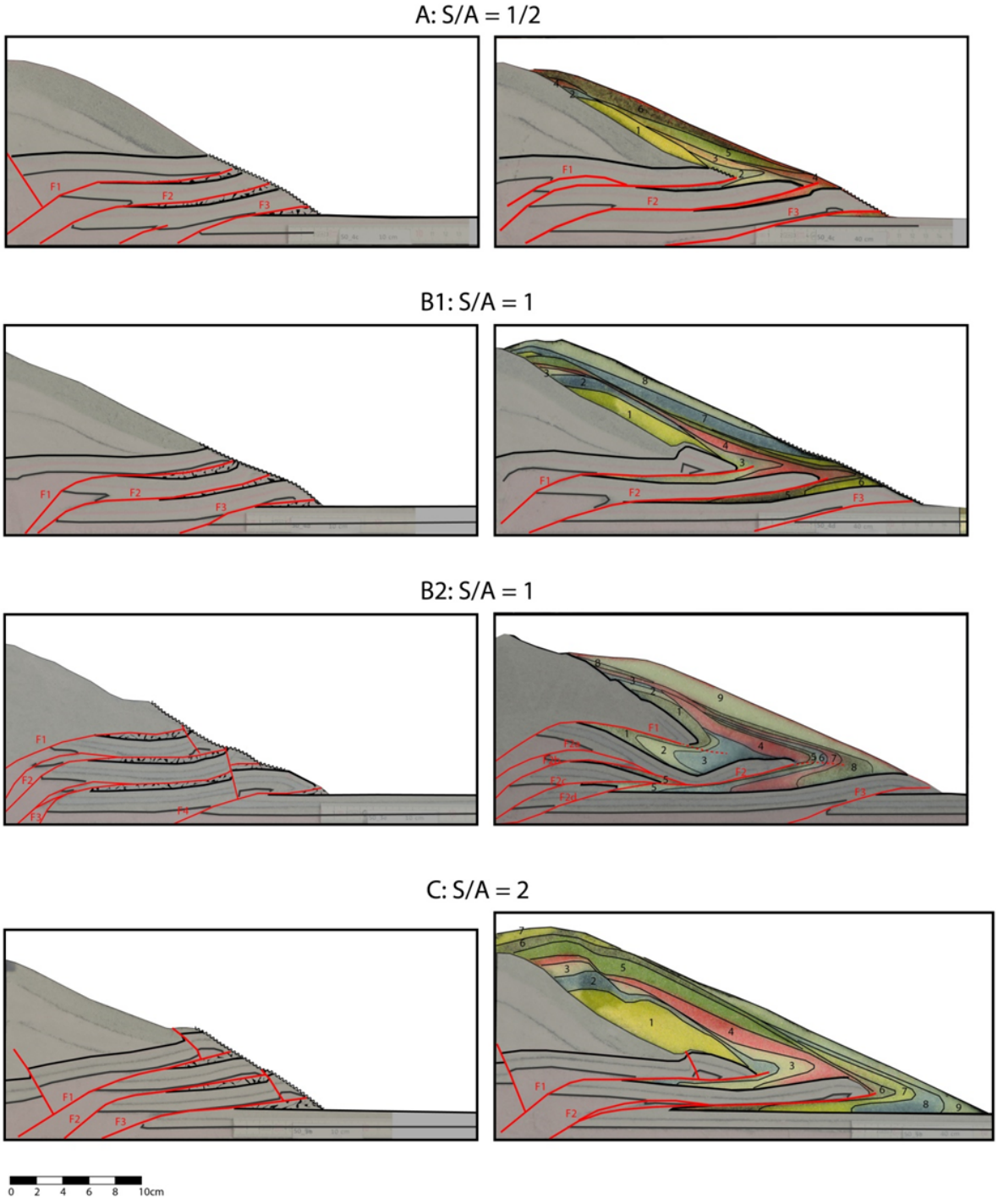

Fig. 2.: Cross sections at the end of the model run for four models with different S/A ratios. Left panels: outside the fan (10 cm from side wall), right panels: in the middle of the fan (40cm from side wall). The fan sediments are distinctly deformed by fault propagation folding. For high S/A ratios (B2, C), fewer thrusts with larger displacement have developed inside the fan than outside..

From continental rifting to seafloor spreading: Insight from 3D thermo-mechanical modeling

Jie Liao[1], Taras Gerya[1]

[1] *Geophysical Fluid Dynamics, Institute of Geophysics, ETH Zurich, Sonneggstrasse 5, CH-8092, Zurich, Switzerland*
e-mail: *jie.liao@erdw.ethz.ch*
session: *Tectonics and Surface Processes*

Introduction

The continuous process from continental rifting to seafloor spreading is a key step in Wilson's cycle (Wilson, 1966), but the complete process is hardly simulated. Continental rifting history influences oceanic spreading. Understanding the inheritance of continental rifting in seafloor spreading is crucial to study the incipient oceanic ridge evolution and remains a big challenge (Lister et al., 1986; Ebinger and Casey, 2001; Nielsen and Hopper, 2004; Taylor et al., 1999, 2009; Gerya, 2012). Compared to the continental rifting process, which has been widely studied by numerical and analogue modelings, few studies have been done on the complete rifting-spreading process due to several diffculties. One is that the long extension process requires large strain to reach the final steady state of seafloor spreading from the initial intact continental lithosphere, and it includes many complex geodynamic processes, such as magma formation, hydrothermal circulation, and crystalization (Gerya, 2010, 2013). Another diffculty is that oceanic spreading in nature is a 3D problem, as large heterogeneities are present along oceanic ridges. Ultra-slow spreading ridges are mostly oblique to spreading directions and consist of alternating magmatic-amagmatic segments (Dick et al., 2003). Symmetric and asymmetric accretion is alternatively distributed along slow spreading ridges (Escartin et al., 2008). Overlapping and transform faults are two common ways that oceanic segments interact (Gerya, 2012) (and reference therein). These 3D features of oceanic ridge require 3D models. Furthermore, the lack of natural observations make the rifting-spreading transition enigmatic. Unlike the widely distributed examples of continental rift and oceanic ridge, very few natural examples record the rifting-spreading transition informations, and some good examples are theWoodlark Basin in the southwestern Pacific ocean (Taylor et al., 1999, 2009), the Laptev Sea margin in the Arctic ocean (Franke D., 2001; Engen O., 2003) and the Red Sea-Gulf of Aden system (d'Acremont et al., 2010; Ligi et al., 2012; Brune and Autin, 2013).

The early-stage formed rift can be a template for the future rift development and continental breakup. However, numerous heterogeneities are generated during continental rifting, and rift propagation may divert from the initial rift trend (the trend of the pre-existing weakness), such as people proposed for the Main Ethiopian Rift (Keranen and Klemperer, 2008). To what extend does rifting history influence continental breakup and seafloor spreading is hardly constrained. Moreover, the importance of rifting history on continental breakup and seafloor spreading is addressed by the formation of transform faults. One possible formation of transform faults which is widely proposed is related with the inheritance of pre-existing weakness. Transform faults my initiate and develop along pre-existing fracture zones that perpendicular to oceanic ridges, such as the long transform fault in the equatorial Atlantic ridge between South America and Africa

(Wilson, 1965). The correspondence between the passive margins and the transform faults in the Gulf of Aden also suggests the possibility of inheritance of pre-existing weakness in transform faults formation (d'Acremont et al., 2010).

In this study, we aim to investigate the inheritance of continental rifting on incipient seafloor spreading by modeling the complete rifting-spreading process, with particular attention paid on the two accretion modes (symmetric and asymmetric accretion). The Initial rheological structure of continental lithosphere and the geometry of a pre-existing weak zone are the two key parameters that we study.

Modeling results

We investigate the effect of rheological coupling and decoupling on continental rifting and seafloor spreading using 3D numerical models (Fig. 1a). Two different rheological coupling structures in terms of the absence/presence of a strong lower crust are used in our models, named decoupled (DCP) rheology (i.e. weak lower crust) and coupled (CP) rheology (i.e. strong lower crust) (Fig. 1b). Two different idealized model setups in terms of the geometry of the weak zone are employed, named 2D-like and 3D-like setups (Figs. 1c and 1d). Our preliminary modeling results show that the asymmetric accretion involved with active detachments is favored by DCP models, while CP models most likely generate symmetric accretion. Initiation, development and termination of detachment faults, and curved geometry of oceanic detachment faults are discussed.

2D-like model setup

2D-like model setups (Fig. 1c) are used in this section. The decoupled (DCP) models generate numerous heterogeneities along the continental rifting direction which lead to significant 3D features, and promote asymmetric oceanic accretion (Figs. 2a and 2b). Deformation is more distributed (for instance the widespread molten asthenosphere), and longer extension time is required for the models to reach the steady state of seafloor spreading. Breakup of the lithospheric mantle occurs earlier than that of the crust. The volume of magma chamber is pressure and temperature dependent. Large magma chamber is generated in the DCP models (Fig. 2e), such as in Model 1. Growth rate of the oceanic crust becomes constant once the seafloor spreading reaches the steady state (Fig. 2f). The coupled (CP) models (with a strong lower crust) generate a roughly straight oceanic ridge developing from a straight continental rift (Figs. 2c and 2d), promoting symmetric oceanic accretion. A small amount of mantle rock is exhumed along the ocean-continental transition zones. In a relatively short time period, both models reach steady state of seafloor spreading, and the oceanic ridges are featured by symmetric accretion. Oceanic detachments are not formed in the CP models.

3D-like model setup

3D-like model setups (Fig. 1d) are used in this section. Instead of extending throughout the whole model box, the crustal or mantle weak zone has a length of 24.5 km along z direction (perpendicular to extension). Similar like the results with 2D-like setups, DCP models promote asymmetric oceanic accretion, while CP models favor symmetric accretion (Fig. 3). In the DCP models, seafloor spreading develops in a propagation way, and curved oceanic ridges form. The oceanic ridges are featured by asymmetric accretion involving active oceanic detachment faults which are established in the late continental rifting stage. The CP models generate relatively straight and symmetric oceanic ridges in a short time period. Molten asthenosphere occurs in a small area beneath the oceanic ridge, and a pair of narrow conjugate passive margins is formed. Along the passive margins, exhumed lithospheric mantle is observed, since high angle normal faults are rotated to low angle detachment faults.

Detachment fault formation

Two types of detachment fault termed continental and oceanic detachment fault are generated in

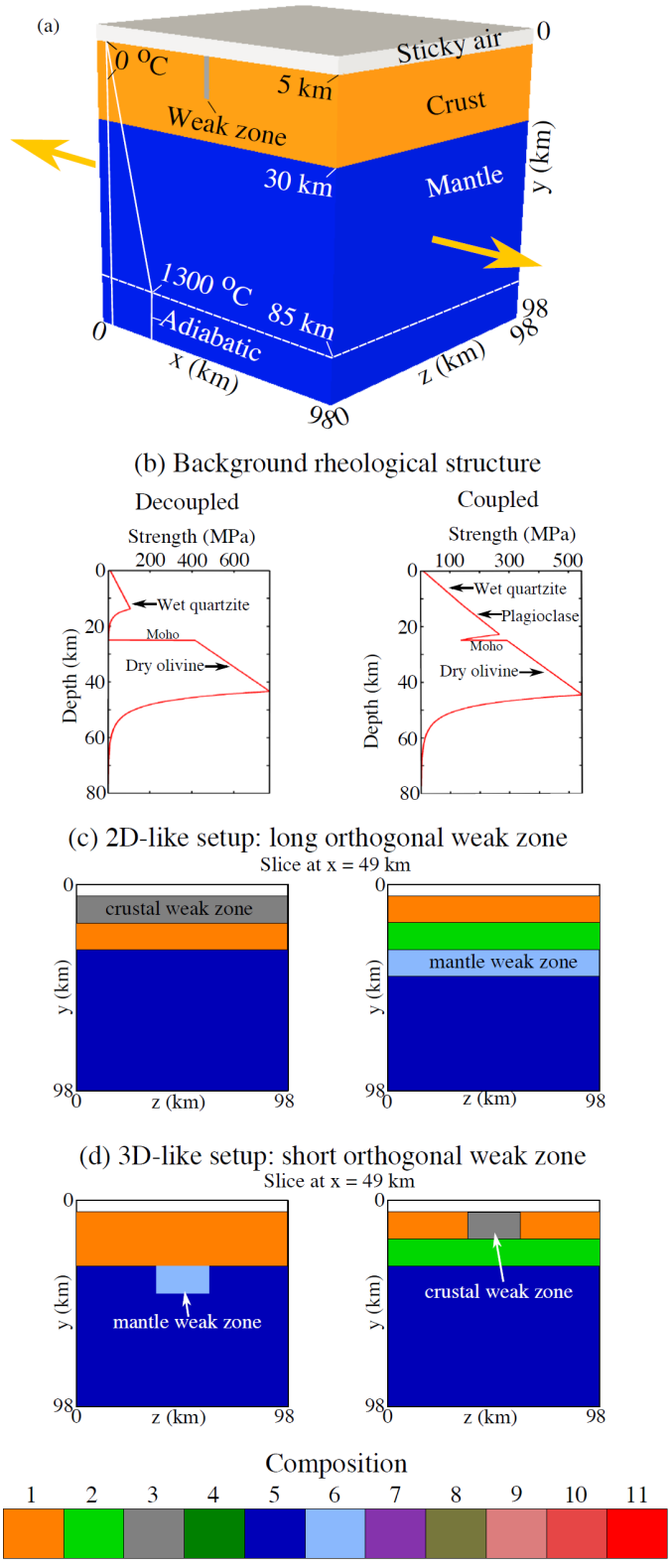

Fig. 1.: Initial model configuration. (a) An example setup of 3D model (corresponds to decoupled rheology with a 2D-like weak zone). (b) Two different rheological structures of the background (without the influence of weak zone) are used in this study, named decoupled and coupled rheology. Coupled rheology is implemented by imposing a strong lower crust. (c) 2D-like model setups for decoupled (left panel) and coupled (right panel) rheology. The slices are taken along y-z plane at x = 49 km. (d) 3D-like model setups for decoupled (left panel) and coupled (right panel) rheology. Normal extension velocity is prescribed on the whole left and right surfaces (half extension rate is 1.5 cm/yr). Based on mass conservation, the constant normal velocities on the top and bottom surfaces are calculated and prescribed (Gerya, 2013). The front and back surfaces are free slip. A free surface condition for the crustal surface is approximated by adding the sticky air layer on the top.

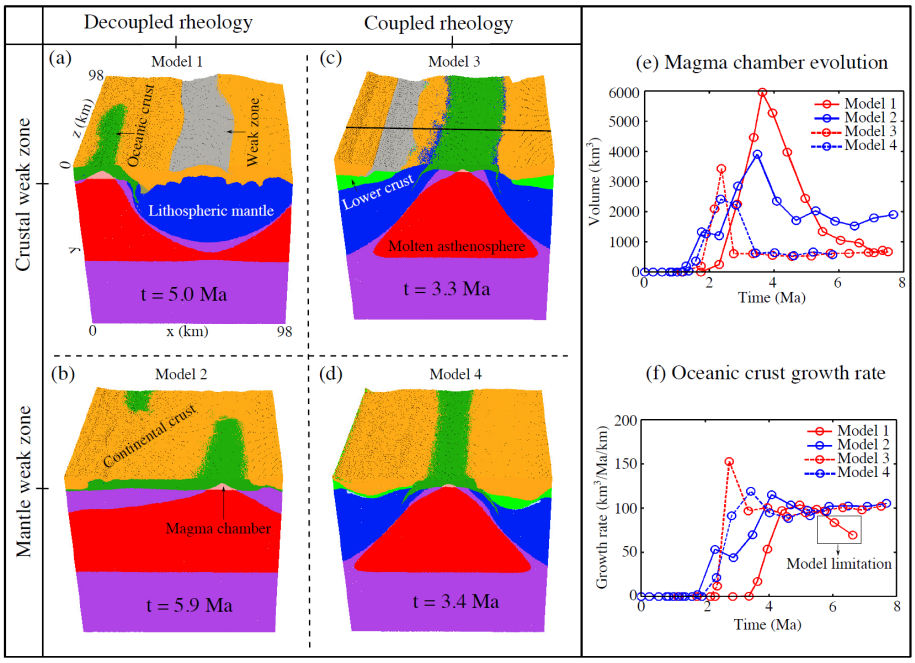

Fig. 2.: Comparison of modeling results with 2D-like setups. Rheological coupling/decoupling and weak zone location are varied in different models. Color shows composition (a-d), also see Fig. 1 for the colormap. (e) Dynamic evolution of magma chamber volume and (f) growth rate of oceanic crust are compared for each model. The black line in c shows the location of slices used in the Figs. 4 and 5. Note that the decoupled rheology promotes asymmetric accretion, while the symmetric accretion is favored by coupled rheology

the CP and DCP models, respectively. In the CP models, the continental detachment faults are generated through fast rotation of the high angle normal faults (Fig. 4). Due to the localized lithospheric extension and thinning, one branch of the major conjugate faults is rotated to low angle by the fast upwelling asthenosphere. Macleod et al. (2009) demonstrated that core complex detachment faults initiate from high angle ($60° \pm 10°$) normal faults and rapidly rotate to low angles ($\sim 30°$). The detachment faults initiated and developed in the continental rifting stage gradually become inactive in the late rifting and early spreading stages. This may caused by the rapid asthenosphere upwelling and intense magmatism which cut off the detachment faults and accommodate extension space (Lister et al., 1986; Ebinger and Casey, 2001; Macleod et al., 2009).

In contrast, in the DCP models, the oceanic detachments establish during the late continental rifting and early seafloor spreading (Fig. 5), accompanied by oceanic crust growth. Following the location of the initial weak zone, two conjugate normal faults form along the magma walls in the late rifting stage (t=3.4 Ma in Fig. 5a). One branch of the conjugate normal faults gradually develops into a detachment fault (t=4.6 Ma in Fig. 5a), as strain weakening and shear heating amplify perturbations along the normal faults and break up the symmetry. From the middle to the edges along z direction, the formation time of the detachment fault delays (t=6.4 Ma in Fig. 5a). Therefore, similar like the oceanic ridge propagation, the detachment fault forms first in a certain location and then propagates to two directions along the ridge. As a consequence, a curved geometry of the detachment fault forms on a map view (Fig. 5b). This 3D curved geometry of detachment faults can be in comparable with natural observations (left panel in Fig. 5d). Thus, our modeling results may provide a possible dynamic formation of curved detachment faults formation.

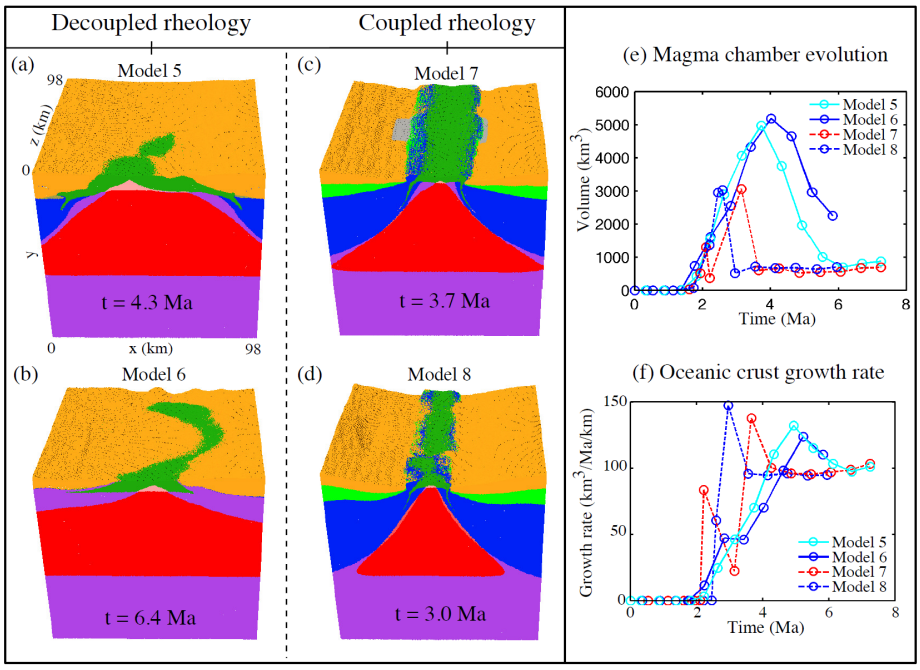

Fig. 3.: Comparison of modeling results with decoupled and coupled rheologies using 3D-like setups. (a-d) Comparison of composition (see Figs. 1 and 2 for the color notation). (e) Dynamic evolution of magma chamber volume and (f) growth rate of oceanic crust are compared for each model. Model 7 has a crustal weak zone, and Model 8 has a mantle weak zone, both of which are seating in the middle of the model domain. Note that the decoupled rheology promotes asymmetric accretion, while the symmetric accretion is favored by coupled rheology.

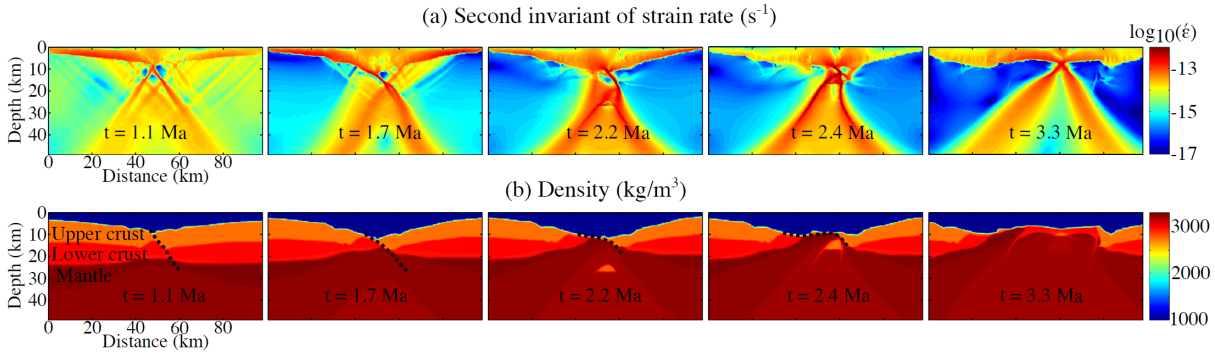

Fig. 4.: Evolution of the continental detachment fault generated in Model 3. Location of the slices is shown in Fig. 2c by the black line (z = 38 km). (a) Second invariant of strain rate and (b) density show the rotation of the high angle normal fault (black dotted line).

In the life cycle of OCCs (Macleod et al., 2009), detachment faults are terminated by intense magma that delivered to the footwall. This feature is observed in our modeling results (Figs. 4 and 5). Suffcient magma cuts through the detachment fault (compare the snapshot at t=6.4 Ma to the one at t=5.8 Ma in Fig. 5c), changing the accretion pattern from asymmetric to symmetric. And as a consequence, abandoned axial volcanic ridge (AVR) is generated on the conjugate plate (the hanging wall, Figs. 5b-5c, t = 6.4 Ma). The formation of abandoned AVR is evidenced by the natural example on the MAR at 5°S (Reston et al., 2002), where the extinct axial volcanic ridge and abandoned detachment faults are observed on the conjugate plate (Fig. 5d). The reconstruction (Fig. 5d) based on the bathymetry data (matching the fault scarps on the two flanks of the active ridge) indicates that the two core complexes (numbered 1 and 2 in the Fig. 5d) used to belong together. Thus, the abandonment of AVR may occur together with the abandonment of detachment faults.

Conclusion

Based on our modeling results, oceanic spreading has a strong dependence on continental rifting which is influenced by the initial rheological coupling/decoupling of continental lithosphere. Rheological coupling/decoupling generates two types of incipient oceanic ridge development: (1) coupled lithospheric rheology promotes symmetric oceanic accretion, while (2) decoupled lithospheric rheology favors the formation of asymmetric oceanic accretion involving development of active detachment faults. In the models with coupled rheology, lithospheric scale shear zones are generated and lithosphere thins rapidly. Decoupled models extend in a depth-dependent way. Two types of detachment fault establish in terms of their formation time. Continental detachment faults establish in the models with coupled rheology and mainly develop during rifting stage. Intense magmatism terminates the continental detachment faults in the late rifting stage. Oceanic detachment faults form in the oceanic crust, dominating ridge accretion asymmetrically. Magmatism can also terminates oceanic detachment faults, switching oceanic accretion from asymmetric to symmetric. Curved oceanic detachment faults can be simulated with 3D models.

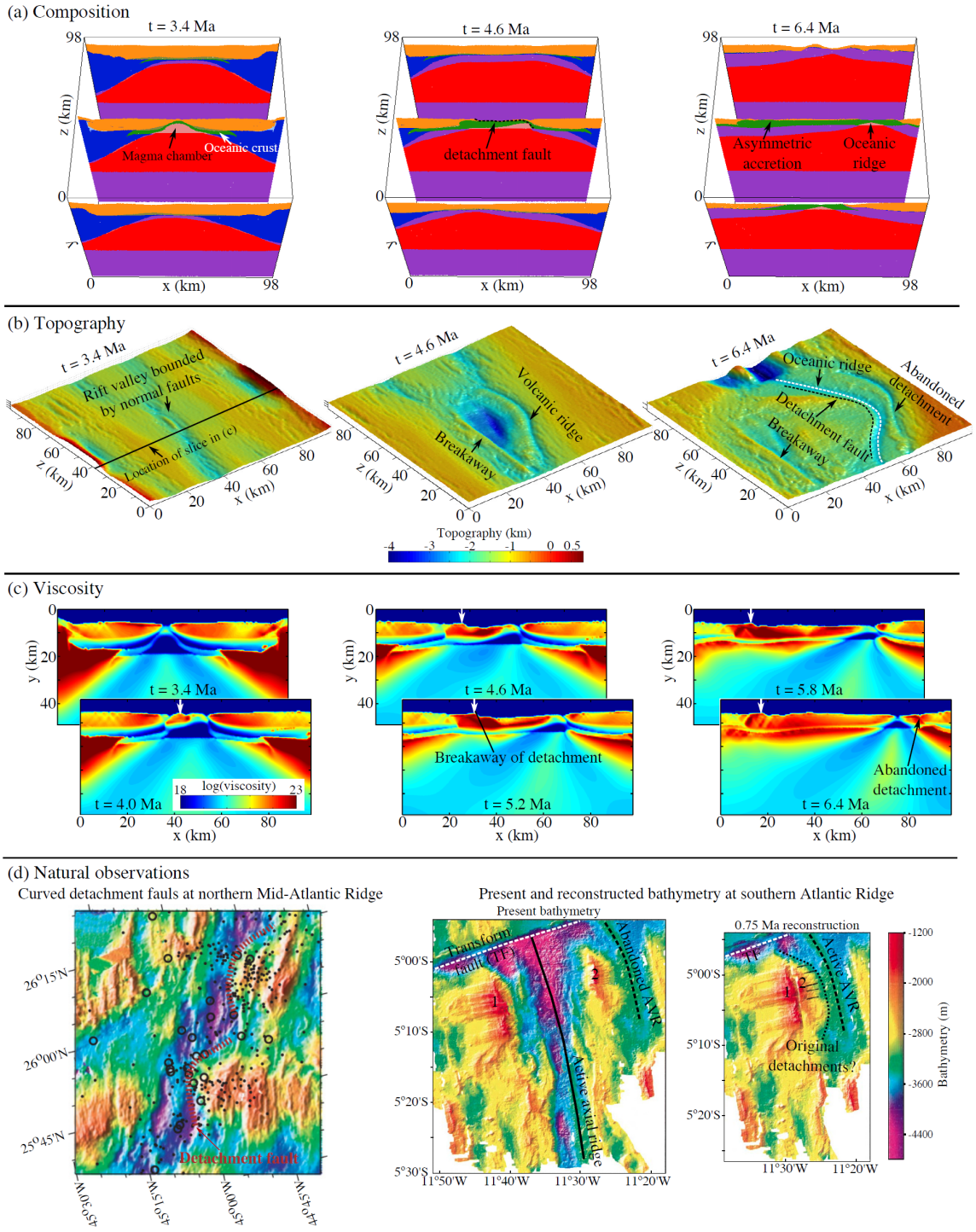

Fig. 5.: Evolution of the detachment fault generated in Model 6 and comparison with natural examples. (a) Composition, (b) topography and (c) viscosity snapshots of model results are shown for different times. The black line (z = 38 km) in (b) shows the location of viscosity slices in (c). White arrows in viscosity slices (c) show the positions of detachment breakaway. (d) Natural examples of curved detachment faults at northern Mid-Atlantic Ridge (modified after Escartin et al. (2008)) and ridge abandonment at 5°S Atlantic ridge (modified after Reston et al. (2002)).

References

Afonso, J.C., Ranalli, G., 2004. Crustal and mantle strengths in continental lithosphere: is the jelly sandwich model obsolete? Tectonophysics 394, 221–232. doi:10.1016/j.tecto.2004.08.006.

Allken, V., Huismans, R.S., 2012. Factors controlling the mode of rift interaction in brittle-ductile coupled systems: A 3d numerical study. Geochem. Geophys. Geosyst. 13, 1–18. doi:10.1029/2012GC004077.

Allken, V., Huismans, R.S., Thieulot, C., 2011. Three-dimensional numerical modeling of upper crustal extensional system. J. Geophys. Res. 116, 1–15. doi:10.1029/2011JB008319.

Armitage, J.J., Collier, J.S., Minshull, T.A., 2010. The importance of rift history for volcanic margin formation. Nature 465, 913–917. doi:10.1038/nature09063.

Brace, W.F., Kohlstedt, D.L., 1980. Limits on lithospheric stress imposed by laboratory experiment. J. Geophys. Res. 85, 6248–6252.

Brune, S., Autin, J.a., 2013. The rift to break-up evolution of the gulf of aden: Insights from 3d numerical lithospheric-scale modelling. Tectonophysics 607, 65–79. doi:10.1016/j.tecto.2013.06.029.

Brune, S., Popov, A.A., Sobolev, S.V., 2012. Modeling suggests that oblique extension facilitates rifting and continental break-up. J. Geophys. Res. 117, 1–16. doi:10.1029/2011JB008860.

Buck, W.R., 2006. The role of magma in the development of the afro-arabian rift system. Geological Society, London, Special Publications 259, 43–54. doi:10.1144/GSL.SP.2006.259.01.05.

Buck, W.R., Lavier, L.L., Pollakov, A.N.B., 2005. Models of faulting at mid-ocean ridges. Nature 434, 719–723. doi:10.1038/nature03358.

Burgmann, R., Dresen, G., 2008. Rheology of the lower crust and upper mantle: Evidence from rock mechanics, geodesy, and field observations. Annu. Rev. Earth Planet. Sci. 36, 531–567. doi:10.1146/annurev.earth.36.031207.124326.

Burov, E.B., 2010. The equivalent elastic thickness (te), seismicity and the long-term rheology of continental lithosphere: Time to burn-out "crème brûlée"? insights from large-scale geodynamic modeling. Tectonophysics 484, 4–26. doi:10.1016/j.tecto.2009.06.013.

Burov, E.B., Watts, A.B., 2006. The long-term strength of continental lithosphere: "jelly sandwich" or "crème brûlée"? GSA Today 16.

Byerlee, J., 1978. Friction of rocks. Pure Applied Geophysics 116, 615–626.

Chemenda, A., Deverchere, J., Calais, E., 2002. Three-dimensional laboratory modelling of rifting: Application to the baikal rift, russia. Tectonophysics 356, 253–273.

Choi, E., Lavier, L., Gurnis, M., 2008. Thermomechanics of mid-ocean ridge segmentation. Phys. Earth Planet. Inter. 171, 374–386. doi:10.1016/j.pepi.2008.08.010.

Corti, G., Van Wijk, J.W., Cloetingh, S., Morley, K., 2007. Tectonic inheritance and continental rift architecture: Numerical and analogue models of the east african rift system. Tectonics 26, 1–13. doi:10.1029/2006TC002086.

d'Acremont, E., Leroy, S., Maia, M., Gente, P., Autin, J., 2010. Volcanism, jump and propagation on the sheba ridge, eastern gulf of aden: segmentation evolution and implications for oceanic accretion processes. Geophys. J. Int. 180, 535–551. doi:10.1111/j.1365-246X.2009.04448.x.

Dick, H.J.B., Lin, J., Schouten, H., 2003. An ultraslow-spreading class of ocean ridge. Nature 426, 405–412.

Dunbar, J.A., Sawyer, D.S., 1988. Continental rifting at pre-existing lithospheric weaknesses. Nature 333, 450–452.

Ebinger, C.J., Casey, M., 2001. Continental breakup in magmatic provinces: An ethiopian example. Geology 29, 527–530.

Engen O., Eldholm O., B.H., 2003. The arctic plate boundary. J. Geophys. Res. 108, 2075–2092. doi:10.1029/2002JB001809.

Escartin, J., Smith, D.K., Cann, J., Schouten, H., Langmuir, C.H., Escrig, S., 2008. Central role of detachment faults in accretion of slow-spreading oceanic lithosphere. Nature 455, 792–794. doi:10.1038/nature07333.

Franke D., Hinz K., O.O., 2001. The laptev sea rift. Mar. Pet. Geol. 18, 1083–1127.

Gerya, T., 2010. Dynamics instability produces transform faults at mid-ocean ridges. Science 329, 1047–1050. doi:10.1126/science.1191349.

Gerya, T., 2012. Origin and models of oceanic transform faults. Tectonophysics 522-523, 34–54. doi:10.1016/j.tecto.2011.07.006.

Gerya, T.V., 2013. Three-dimensional thermomechanical modeling of oceanic spreading initiation and evolution. Phys. Earth Planet. Inter. 214, 35–52. doi:10.1016/j.pepi.2012.10.007.

Gregg, P.M., Behn, M.D., Lin, J., Grove, T.L., 2009. Melt generation, crystallization, and extraction beneath segmented oceanic transform faults. J. Geophys. Res. 114, 1–16. doi:10.1029/2008JB006100.

Huismans, R., Beaumont, C., 2011. Depth-dependent extension, two-stage breakup and cratonic underplating at rifted margins. Nature 473, 74–79.

Jackson, J., 2002. Strength of the continental lithosphere: Time to abandon the jelly sandwich? GSA Today 12, 4–10. doi:10.1130/1052-5173(2002)012¡0004:SoTCIT¿2.0.Co;2.

Keranen, K., Klemperer, S.L., 2008. Discontinuous and diachronous evolution of the main ethiopian rift: Implications for development of continental rifts. Earth Planet. Sci. Lett. 265, 96–111.

Ligi, M., Bonatti, E., Bortoluzzi, G., Cipriani, A., Cocchi, L., Tontini, F.C., 2012. Birth of an ocean in the red sea: Initial pangs. Geochem. Geophys. Geosyst. 13, 1–29. doi:10.1029/2012GC004155.

Lister, G.S., Etheridge, M.A., Symonds, P.A., 1986. Detachment faulting and the evolution of passive continental margins. Geology 14, 246–250. doi:10.1130/0091-7613(1986)14¡246:DFATEO¿2.0.CO;2.

Macleod, C.J., C., S.R., Murton, B.J., Casey, J.F., Mallows, C., Unsworth, S.C., Achenbach, K.L., Harris, M., 2009. Life cycle of oceanic core complexes. Earth Planet. Sci. Lett. 287, 333–344. doi:10.1016/j.epsl.2009.08.016.

Maggi, A., Jackson, J.A., Priestley, K., Baker, C., 2000. A re-assessment of focal depth distributions in southern iran, the tien shan and northern india: do earthquakes really occur in the continental mantle? Geophys. J. Int. 143, 629–661.

Nielsen, T.K., Hopper, J.R., 2004. From rift to drift: Mantle melting during continental breakup. Geochem. Geophys. Geosyst. 5, 1–24. doi:10.1029/2003GC000662.

Nyblade, A.A., Brazier, R.A., 2002. Precambrian lithospheric controls on the development of the east african rift system. Geology 30, 755–758.

Puthe, C., Gerya, T., 2014. Dependence of mid-ocean ridge morphology on spreading rate in numerical 3-d models. Gondwana Res. 25, 270–283. doi:10.1016/j.gr.2013.04.005.

Reston, T.J., Weinrebe, W., Grevemeyer, I., Flueh, E.R., Mitchell, N.C., Kirstein, L., Kopp, C., Kopp, H., participant of Meteror 47/2, 2002. A rifted inside corner massif on the mid-atlantic ridge at 5s. Earth Planet. Sci. Lett. 200, 255–269.

Smith, D.K., Cann, J.R., Escartin, J., 2006. Widespread active detachment faulting and core complex formation near 138 n on the mid-atlantic ridge. Nature 442. doi:10.1038/nature04950.

Taylor, B., Goodliffe, A.M., Martinez, F., 1999. How continents break up: Insights from papua new guinea. J. Geophys. Res. 104, 7497–7512.

Taylor, B., Goodliffe, A.M., Martinez, F., 2009. Initiation of tranform faults at rifted continental margins. C, R. Geoscience , 341.

Tucholke, B.E., Behn, M.D., Buck, W.R., Lin, J., 2008. Role of melt supply in oceanic detachment faulting and formation of megamullions. Geology 36, 455–458. doi:10.1130/G24639A.1.

Van Wijk, J., 2005. Role of weak zone orientation in continental lithosphere extension. Geophys. Res. Lett. 32, 1–4. doi:10.1029/2004GL022192.

Van Wijk, J.W., Blackman, D.K., 2005. Dynamics of continental rift propagation: the end-menber modes. Earth Planet. Sci. Lett. 229, 247–258.

Wilson, J.T., 1965. A new class of faults and their bearing on continental drift. Nature 207, 343–347.

Wilson, J.T., 1966. Did the atlantic close and then re-open? Nature 211, 676–681.

Wood, C.A., 1983. Continental rift jumps. Tectonophysics 94, 529–540.

Yamasaki, T., Gernigon, L., 2010. Redistribution of the lithosphere deformation by the emplacement of underplated mafic bodies: implications for microcontinent formation. Journal of the Geological Society, London 167, 961–971. doi:10.1144/0016-76492010-027. 5

Dynamic Modelling of Accretionary Prisms and Stratigraphy of Forearc basins

Utsav Mannu[1], Kosuke Ueda[1], Sean D. Willett[1], Taras Gerya[2], Michael Strasser[1]

[1] *Geological Institute, ETH Zürich, 8092 Zürich, Switzerland*
[2] *Institute of Geophysics, ETH Zürich, 8092 Zürich, Switzerland*
e-mail: *utsav.mannu@erdw.ethz.ch*
session: *Tectonics and Surface Processes*

Introduction

Subduction zones are often accompanied by a landward accumulation of sediments scraped off the subducting oceanic plate into the accretionary prism. Accretionary prisms are considered analogous to wedges of snow or soil in front of a moving rigid indenter and deform to attain a critical taper (Davis et al., 1983; Dahlen, 1984). However, contemporary analogue and theoretical models for accretionary prisms (Wang and Hu, 2006) and inferences from high-resolution seismic imaging (Park et al., 2002; Bangs et al., 2004; Moore et al. 2007) have lead to a change in our understanding of wedge dynamics. External factors such as sedimentation on the wedge top have the potential to stabilize the wedge and to reduce the extent of internal deformation (Storti and McClay, 1995). Amount and spatial variability of sedimentation (Simpson, 2010) can lead to different wedge architectures. As sedimentation rates can change in time and space, the overall feedback provided by sedimentation to wedge dynamics and vice-versa becomes important in understanding the evolution of accretionary wedges. We investigate the effects of sedimentation with a dynamic 2D thermo mechanical model incorporating surface processes, strain weakening and sediment subduction. The model includes high-resolution particle tracking of sediment layers in order to visualize the developing stratigraphy of the wedge-top basins. Stratigraphic features such as unconformities are easily observable in the model. Wedge top basin stratigraphy revealed by high-resolution seismic acquisitions and borehole data has proved to be an invaluable repository of past tectonic movements within accretionary prisms (Beaudry and Moore, 1985; Strasser et al. 2009). Numerical modeling presents an opportunity to test interpretations of seismic records for dynamic consistency. In this study, we present a new numerical model for: a) the architecture of the wedge; and b) the stratigraphy of wedge-top basins to understand the physics of wedge evolution.

Method

We use a modified version of the thermo-mechanical code I2VIS (Gerya and Yuen, 2003, 2007). It is based on the conservative fully staggered finite difference scheme with visco-brittle/plastic rheology, and a non-diffusive marker- in-cell technique. The modelling domain spans *3500 km* × *200 km* (Figure 1) on an irregular grid of 1284 x 300 nodes. The initial model setup mimics very broad features of a passive margin. Subduction initiation is achieved by the initial geometry and a prescribed weak zone (light blue in Figure 1). The weak zone also ensures decoupling between oceanic and continental crust during subduction initiation. The lower boundary of the model is permeable with an infinity-like external slip condition ensuring a free slip condition at an external prescribed boundary (Δz_{ext} = 2000 km). The adjoining 10 km

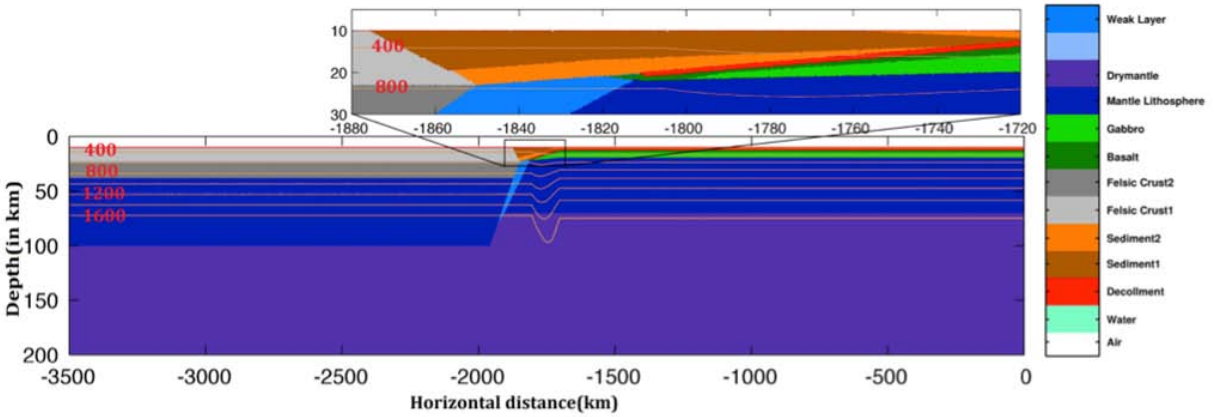

Fig. 1.: Initial model setup. The oceanic crust is overlain by two types of rheologically identical sediments (light and deep brown), for 2.5 km and another 1 km of weak layer prescribed to become the décollement (red). The oceanic crust is 7 km thick and consists of 2 km of basaltic (deep green) and another 5 km of gabbroic rocks (light green). The continental crust is 28 km thick having two equally thick layers for upper (light grey) and lower crust (dark grey) that differ in density and rheology.

zone is allocated maximum viscosity of 10^{19} Pa s to minimize the mechanical interactions along this boundary (Gorczyk et al., 2007a). A free slip condition is imposed on all other boundaries. The convergence velocity is implemented by imparting horizontal velocities to the distal oceanic and continental plates.

The basin isochronal surfaces are tracked by addition of a line of Lagrangian markers in time along the upper surface of the model, which subsequently are buried, transported, and deformed according to the velocity field generated in the model (Figure 2). The sedimentation is implemented in two ways: (i) focused deposition of sediments in the basin (i.e. simulating ponding geometries resulting presumably by gravity flows (e.g. turbidites) into closed basins, and (ii) continuous draping along the submerged wedge surface thus simulating hemi-pelagic sedimentation.

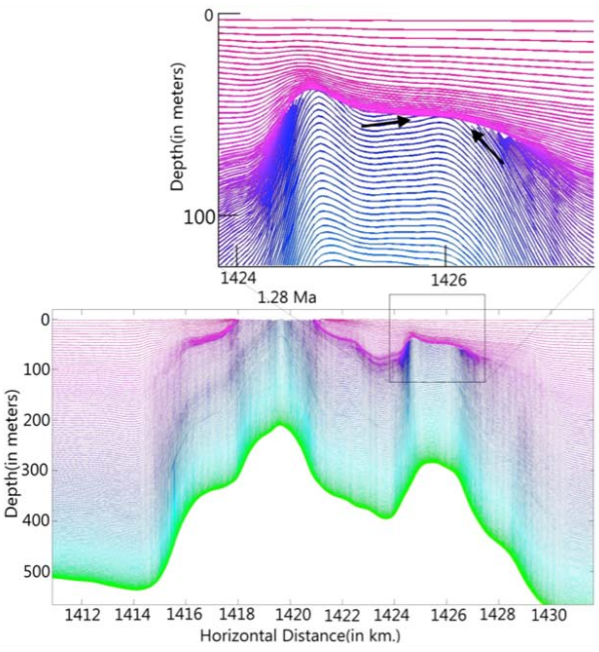

Fig. 2.: A typical result for basin stratigraphy illustrating an unconformity in the forearc basin (marked with black arrows). The unconformity illustrates the erosional surface during the subsequent thrust faults. The color from green to purple signifies the time when the marker line was placed on the surface, green being the oldest and purple youngest.

Preliminary Results

A reference model is illustrated in Figure 3 after 13.4 Myr of model run. Based on the observations of time frames from the reference model, a retro-forearc basin forms that remains passive for most

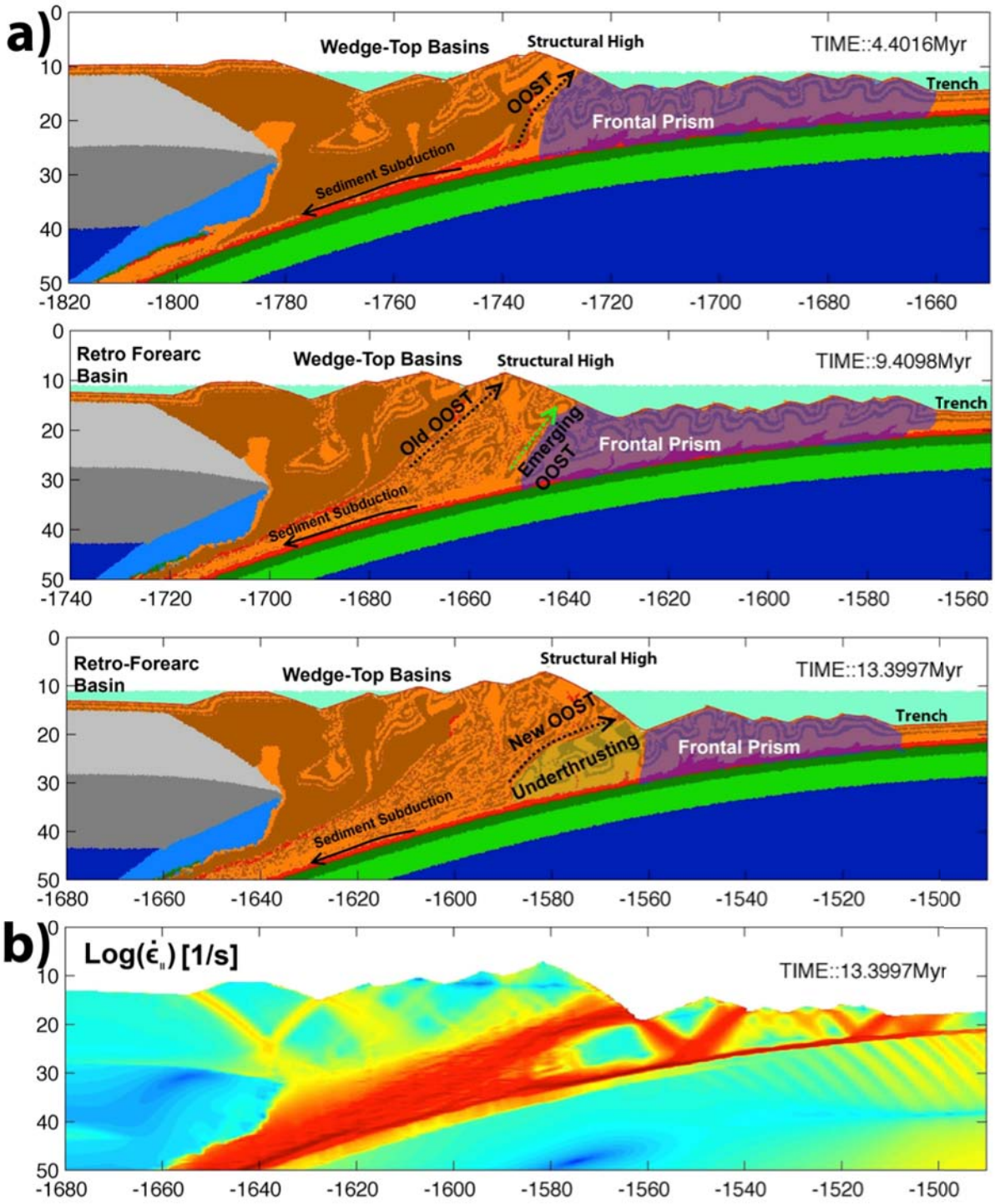

Fig. 3.: Accretionary prism formed in reference model with internal angle of friction for décollement $\tan(\phi_D) = 0.08$ and internal angle of friction for sediments $\tan(\phi) = 0.4$. The convergence velocity is 5cm/yr, distributed between the continental and oceanic plates in a ratio of 1:2. There is no sedimentation or strain weakening in this model. a) Plot of material types at ∼4.4Myr, ∼9.4 Myr and 13.4My. b) Plot of second invariant of strain rate tensor at ∼13.4Myr.

part of the model run. Other smaller wedge-top basins are formed on the top of the wedge, which is separated from the frontal prism by a structural high. The structural high is uplifted due to displacement along an Out-Of-Sequence Thrust (OOST) and subsequent back accretion. Figure 3 illustrates that episodic OOSTs form prior to back accretion of the frontal prism, and keeps on stepping forward with time. A deep slope basin is formed at the transition between the frontal prism and the uplifted part of the prism due to back accretion. This uplifted part of the prism is relatively stable and undergoes little deformation with time hence is referred to as the stable wedge. When a new OOST emerges, it rapidly overthrusts the frontal prism and slope basin. This causes the uplift of the material lying between the old OOST and the emerging one. Sediment subduction occurs throughout the model evolution. The volume of sediment subduction decreases around 5 Ma; thereafter, it fluctuates within a fixed range. The frontal prism undergoes perpetual in-sequence thrusting, accreting material off the trench. However, the effective length of the frontal prism decreases after initiation of back-accretion. When that the back-accretion halts, there is a rapid increase in frontal prism length. Based on various model run we observe amount of back-accretion is controlled by the strength of the décollement and of the sediments.

Discussion & Outlook

Building upon the work illustrated here, the study will present various coupled wedge- and sedimentation scenarios to discuss effects of spatio-temporal variation in sedimentation on wedge dynamics and vice versa. Preliminary results indicate that deformation style variations correlate with sedimentation regime along a trench to forearc basin transect. The synthetic stratigraphy of forearc basin and slope basin resulting from the newly developed isochronal surface tracking approach (Figure 2) illustrates distinct stratigraphic features including unconformities and truncation in the basin. The study will explore and discuss these generic stratigraphic signatures with respect to different structural and mechanical evolution paths of the accretionary prism.

References

Bangs, N. L., Shipley, T. H., Gulick, S. P., Moore, G. F., Kuromoto, S., & Nakamura, Y. (2004). Evolution of the Nankai Trough décollement from the trench into the seismogenic zone: Inferences from three-dimensional seismic reflection imaging. Geology, 32(4), 273-276.

Beaudry, D., & Moore, G. F. (1985). Seismic stratigraphy and Cenozoic evolution of West Sumatra forearc basin. AAPG Bulletin, 69(5), 742-759.

Dahlen, F. A. (1984). Noncohesive critical Coulomb wedges: An exact solution. Journal of Geophysical Research: Solid Earth (1978–2012), 89(B12), 10125-10133.

Davis, D., Suppe, J., & Dahlen, F. A. (1983). Mechanics of fold-and-thrust belts and accretionary wedges. Journal of Geophysical Research: Solid Earth (1978–2012), 88(B2), 1153-1172.

Gerya, T. V., & Yuen, D. A. (2007). Robust characteristics method for modelling multiphase visco-elasto-plastic thermo-mechanical problems. Physics of the Earth and Planetary Interiors, 163(1), 83-105.

Gerya, Taras V., and David A. Yuen. "Characteristics-based marker-in-cell method with conservative finite-differences schemes for modeling geological flows with strongly variable transport properties." Physics of the Earth and Planetary Interiors 140.4 (2003): 293-318.

Gorczyk, W., Willner, A.P., Gerya, T.V., Connolly, J.A.D., Burg, J.P. (2007): Physical controls of magmatic productivity at Pacific-type convergent margins: new insights from numerical modeling. Phys. Earth Planet. In., 163, 209–232

Moore, G. F., Bangs, N. L., Taira, A., Kuramoto, S., Pangborn, E., & Tobin, H. J. (2007). Three-dimensional splay fault geometry and implications for tsunami generation. Science, 318(5853), 1128-1131.

Park, J. O., Tsuru, T., Kodaira, S., Cummins, P. R., & Kaneda, Y. (2002). Splay fault branching along the Nankai subduction zone. Science, 297(5584), 1157-1160.

Simpson, G. D. (2010). Formation of accretionary prisms influenced by sediment subduction and supplied by sediments from adjacent continents. Geology, 38(2), 131-134.

Storti, F., & McClay, K. (1995). Influence of syntectonic sedimentation on thrust wedges in analogue models. Geology, 23(11), 999-1002.

Strasser, M., Moore, G. F., Kimura, G., Kitamura, Y., Kopf, A. J., Lallemant, S., ... & Zhao, X. (2009). Origin and evolution of a splay fault in the Nankai accretionary wedge. Nature Geoscience, 2(9), 648-652.

Wang, K., & Hu, Y. (2006). Accretionary prisms in subduction earthquake cycles: The theory of dynamic Coulomb wedge. Journal of Geophysical Research: Solid Earth (1978–2012), 111(B6).

Evolution of topography of post-Devonian Scandinavia: Effects and rates of erosion

Sergei Medvedev[1], Ebbe H. Hartz[1,2]

[1] *Centre for Earth Evolution and Dynamics, Oslo University, Norway*
[2] *Det norske oljeselskap, Oslo, Norway*
e-mail: *sergei.medvedev@fys.uio.no*
session: *Tectonics and Surface Processes*

Abstract The mechanisms and timing of regional uplift in Scandinavia remain enigmatic given that the region has been relatively tectonically inactive after the NE Atlantic breakup. In this study we combine analysis of the vertical motions of the region caused by the (dominantly) glacial erosion during the Quaternary with AFT analysis of rocks from the area. Using numerical models we first quantify how glacial erosion reshapes the topography. Glacial erosion carved out the fjords and valleys to a depth of 2 km below the palaeo-surfaces. This erosional event represents a major local weight loss and results in a up to 0.8 km uplift of rocks and up to 0.5 km rise of local topography. These estimates only marginally depend on the effective elastic thickness of the lithosphere and thus are robust. We show then that there is no correlation between sample altitude and published AFT data, but that there is a correlation between AFT age and the depth below our constructed pre-glacial summit surface. This correlation demonstrates the robustness of the numerical erosional model, quantifies average erosion rates during Carboniferous-Cretaceous at < 0.01 mm/yr, and outlines the regions of western Scandinavia (Lofoten and Bergen areas and Møre-Trøndelag fault complex) with atypical Mesozoic-Cenozoic evolution probably related to late restructuring.

Numerical model of Quaternary erosion

We use a simple quantitative approach by numerically filling the eroded places with crustal material and calculating the additional load. The resultant modelled surface is thus an approximation of the pre-erosional topography and is not tied to a specific time. This allows us to estimate the elastic response and potential vertical movements of surface topography backward in time (Figs. 1D-F). The numerical model utilizes Matlab-based numerical suite ProShell (Medvedev et al., 2008; Medvedev et al., 2013).

Figures 1 and 2 present results of the numerical model

Combined analysis of AFT data and erosional model

We assign the amount of exhumation calculated in the erosional model (Figs. 1,2) to all of the AFT data points (Hendriks et al., 2007; Ksienzyk et al., 2014). This way we assume that the modelled pre-glacial topography (1B) was the dominant shape of the topography during post-Devonian evolution of Scandinavia and thus the age of rocks is constant on such surfaces.We also introduced the general trend between exhumation and AFT ages (Fig 3.)

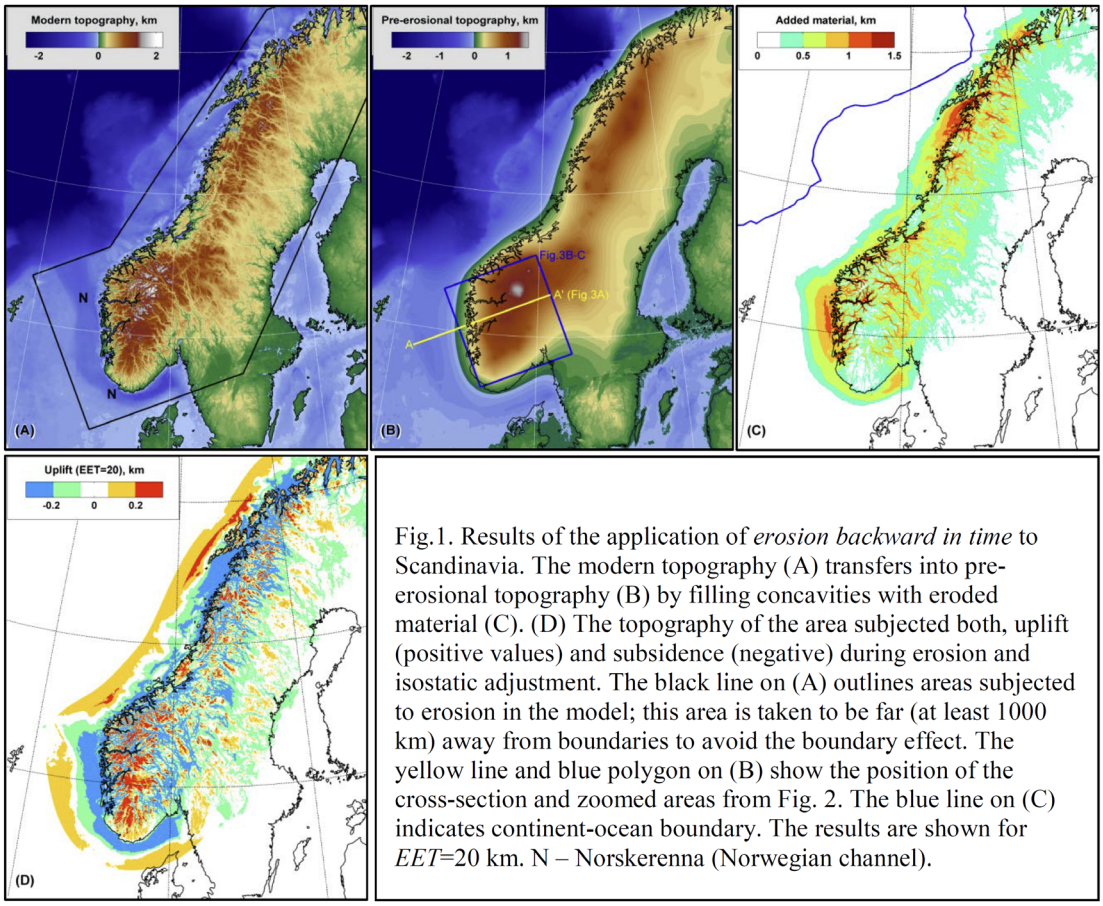

Fig.1. Results of the application of *erosion backward in time* to Scandinavia. The modern topography (A) transfers into pre-erosional topography (B) by filling concavities with eroded material (C). (D) The topography of the area subjected both, uplift (positive values) and subsidence (negative) during erosion and isostatic adjustment. The black line on (A) outlines areas subjected to erosion in the model; this area is taken to be far (at least 1000 km) away from boundaries to avoid the boundary effect. The yellow line and blue polygon on (B) show the position of the cross-section and zoomed areas from Fig. 2. The blue line on (C) indicates continent-ocean boundary. The results are shown for *EET*=20 km. N – Norskerenna (Norwegian channel).

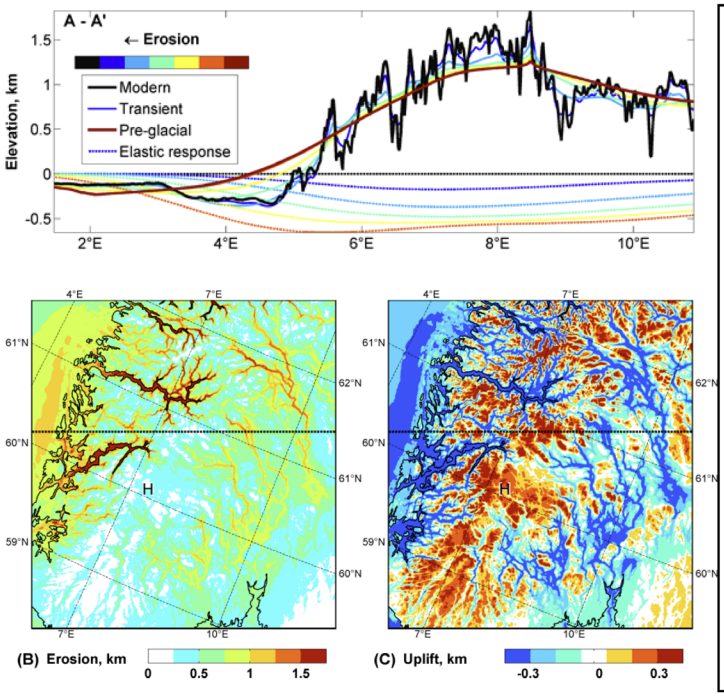

Fig. 2(A) Evolution of topography and the elastic response for profile A-A' Modern topography and modeled transient and pre-glacial topography displayed using colors that correspond to the degree of erosional evolution. The elastic response is 0 at modern time and increases in absolute value with increase of the weight of less eroded upper surface in the *backward-in-time* erosional model. Of note is the summit around 8 ºE which was uplifted by more than 0.4 km. (B) The amount of erosion and (C) erosion-driven elevation changes predicted by the model within a blue box from Fig. 1B. The results are shown for *EET*=20 km H – Hardangervidda (average elevation 1.0-1.1 km)

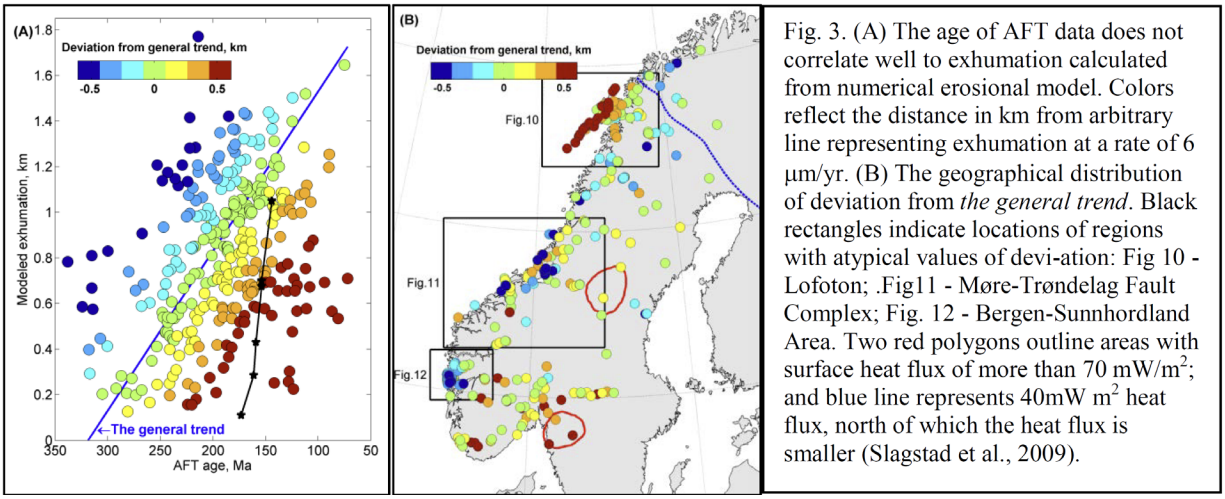

Fig. 3. (A) The age of AFT data does not correlate well to exhumation calculated from numerical erosional model. Colors reflect the distance in km from arbitrary line representing exhumation at a rate of 6 μm/yr. (B) The geographical distribution of deviation from *the general trend*. Black rectangles indicate locations of regions with atypical values of devi-ation: Fig 10 - Lofoton; .Fig11 - Møre-Trøndelag Fault Complex; Fig. 12 - Bergen-Sunnhordland Area. Two red polygons outline areas with surface heat flux of more than 70 mW/m^2; and blue line represents 40mW m^2 heat flux, north of which the heat flux is smaller (Slagstad et al., 2009).

Analysis of the distributions show:

1. The MTFC does not fit to our initial assumption of no tectonic activity. The Lofoton area has erosion of greater scale than one which can be explained by our simple erosional model. The Bergen-Sunnhordland area exhibits relative vertical motion postdating the AFT ages. Thus, we should exclude these areas from consideration.

2. Shallower closure conditions in the South correlate with higher surface heat flux measured in present day conditions and with heat from the Oslo plume during Late Paleozoic (Torsvik et al., 2008). Thus, we introduce an iteratively derived coefficient of 40 m per degree of latitude correction. This approximately corresponds to the 400 m difference in a closure depth over the entire domain, to a maximum of 4 °C/km difference in geothermal gradients.

Conclusions

The combined analysis of erosion model and AFT ages allows us to conclude:

1. The erosion model is robust and reasonable as a first order regional approximation for the reconstruction of pre-glacial topography of Scandinavia.

2. The vertical motion of topography due to glacial carving is a significant contributor to uplift of the Scandinavian mountains (up to 0.4-0.5 km). This result is almost independent from uncertain parameters such as EET.

3. The average thickness of the material eroded during active glacial carving is 430 m. This would correspond to an erosion rate of 0.1 mm/yr (if the glacial carving was active 4.3 My). Locally, however, the rate may exceed 1 mm/yr as a consequence of the localized nature of glacial erosion.

4. The erosion rate during the Mesozoic is less than 1 km per 100 My which corresponds to a rate of <0.01 mm/yr. This rate is low and thus topographic variations of Scandinavia were limited.

5. Our simple model allows the identification of anomalous regions within Scandinavia (non-standard evolution or active tectonic): Lofoton, Bergen-Sunnhordland area, and the Møre-Trøndelag fault complex.

References

Hendriks, B., Andriessen, P., Huigen, Y., Leighton, C., Redfield, T., Murrell, G., Gallagher, K., Nielsen, S.B., 2007. A fission track

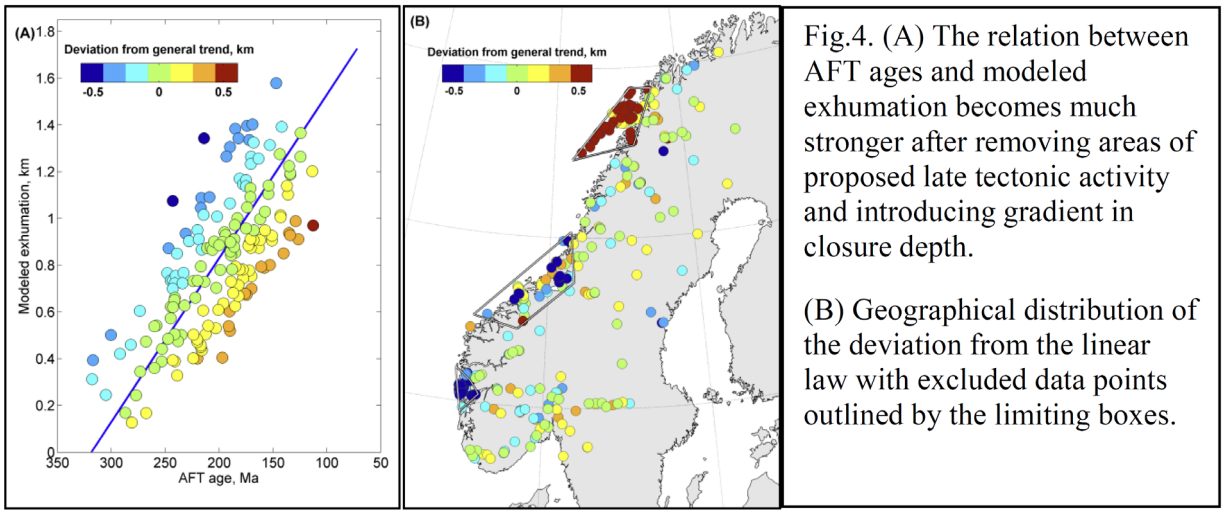

Fig.4. (A) The relation between AFT ages and modeled exhumation becomes much stronger after removing areas of proposed late tectonic activity and introducing gradient in closure depth.

(B) Geographical distribution of the deviation from the linear law with excluded data points outlined by the limiting boxes.

data compilation for Fennoscandia. Norw J Geol 87(1-2), 143-155.

Ksienzyk, A.K., Dunkl, I., Jacobs, D., Fossen, H., Kohlmann, F., 2014. From orogen to passive margin: constraints from fission track and (U–Th)/He analyses on Mesozoic uplift and fault reactivation in SW Norway Geological Society, London, Special Publications 390, 689-702.

Medvedev, S., Hartz, E.H., Podladchikov, Y.Y., 2008. Vertical motions of the fjord regions of central East Greenland: Impact of glacial erosion, deposition, and isostasy. Geology 36(7), 539-542.

Medvedev, S., Souche, A., Hartz, E.H., 2013. Influence of ice sheet and glacial erosion on passive margins of Greenland. Geomorphology 193, 34-46.

Slagstad, T., Balling, N., Elvebakk, H., Midttomme, K., Olesen, O., Olsen, L., Pascal, C., 2009. Heat-flow measurements in Late Palaeoproterozoic to Permian geological provinces in south and central Norway and a new heat-flow map of Fennoscandia and the Norwegian-Greenland Sea. Tectonophysics 473(3-4), 341-361.

Torsvik, T.H., Smethurst, M.A., Burke, K., Steinberger, B., 2008. Long term stability in deep mantle structure: Evidence from the similar to 300 Ma Skagerrak-Centered Large Igneous Province (the SCLIP). Earth Planet. Sci. Lett. 267(3-4), 444-452.

Numerical modeling of main inverted structures in the Western Barents Sea.

Muhammad Armaghan Faisal Miraj[1], Christophe Pascal[1], Roy H. Gabrielsen[2], Jan Inge Faleide[2]

[1]*Institut für Geologie, Mineralogie und Geophysik, Ruhr-Universität Bochum, Bochum, Germany.*
[2]*Department of Geoscience, University of Oslo, Norway*
e-mail: *Muhammad.FaisalMiraj@ruhr-uni-bochum.de*
session: *Tectonics and Surface Processes*

Introduction

A number of fault complexes in the western Barents Sea, preciously formed in response to different Paleozoic to Cenozoic tectonic events, were inverted between Late Triassic to Miocene. Tectonic inversion is evidenced by reactivation of normal faults. The aim of the study is to investigate by numerical modelling the origin of stresses responsible for the different inversion events. A secondary goal is to simulate slip on major faults as a result of tectonic inversion of the western Barents Sea. To these aims, we use a finite-element numerical code Code-Aster (Jean 2013) to simulate stresses and displacements in the study area and plan to use the SORTAN analytical method (Pascal 2004) to predict the sense of slip along major fault planes.

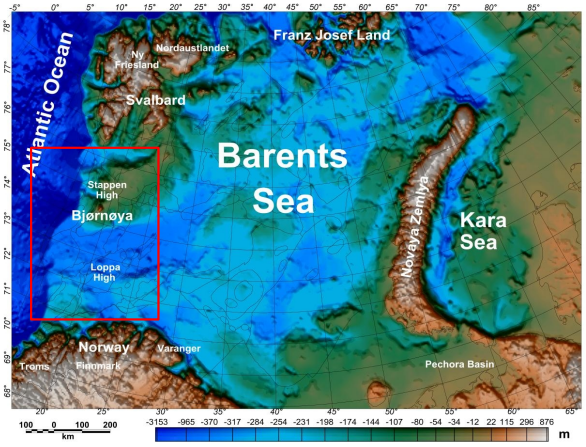

Fig. 1.: Regional setting and location of the study area (Modified from Barrère et al., 2009)

Geological setting

The study area is part of the western Barents Sea and extends from 15 - 25° E and 70 - 74° N (Figure 1 & 2). A lot of research work has already been done in the Barents Sea (Gabrielsen et al., 1990; Doré 1991; Ritzmann and Faleide, 2007; Tsikalas et al., 2012; Gernigon et al. 2014).

The major tectonic phases responsible for the development of the geological framework of the western Barents Sea includes the collision of Baltica and Laurentia in mid-Paleozoic time followed by Mesozoic rifting events and Cenozoic breakup (Gabrielsen et al., 1990; The first main tectonic event, the Timanian Orogeny, resulted in a fold-and-thrust belt along the northeastern passive margin of Baltica and the southwestern Barents Sea during (Ediacarian) times (Roberts and Olovyanishnikov, 2004; Gernigon et al. 2014). The Caledonian Orogeny resulted in the closure of the Iapetus Ocean due to the convergence of the Laurentian and Baltic plates at $\sim$ 400 Ma (Roberts, 2003).

The Late Mesozoic-Cenozoic tectonic evolution of the southwestern Barents Sea is influenced by several stages of extension and transtension. In Early Triassic, the western Barents Sea was af-

fected by rifting and this rift phase is also recorded in many parts of the Arctic and North Atlantic regions (Tsikalas et al., 2012 and Gernigon et al. 2014). Middle-Late Triassic was the postrift thermal subsidence time in the North Atlantic and Arctic basins (Gernigon et al. 2014) but in contrast, the Barents shelf area experienced the initiation of progressive uplift of the northern, eastern, and southern Barents Sea regions (Worsley et al., 2008).

The Middle Jurassic to Early Cretaceous Atlantic rifting affected the western margin of the Barents Sea Shelf (Faleide et al., 2008). These continuous rifting phases during the Jurassic are responsible for the development of major deep basins in the western Barents Sea (Gernigon et al. 2014). In the Late Cretaceous to Paleocene times strike-slip movements took place in the western Barents Sea which resulted in to the formation of pull-apart basins (Faleide et al., 1996).

During and after the Early Tertiary rifting and breakup of the northern North Atlantic, the western margin of the Barents Sea was subject to tectonic inversion, apparently involving elements of shortening in NE-SW and NW-SE directions (Leever et al., 2008). Several mechanisms responsible for the inversion have been suggested, including secondary effects of the uplift of Iceland and local transpression associated with the geometry and configuration of the plate boundary itself.

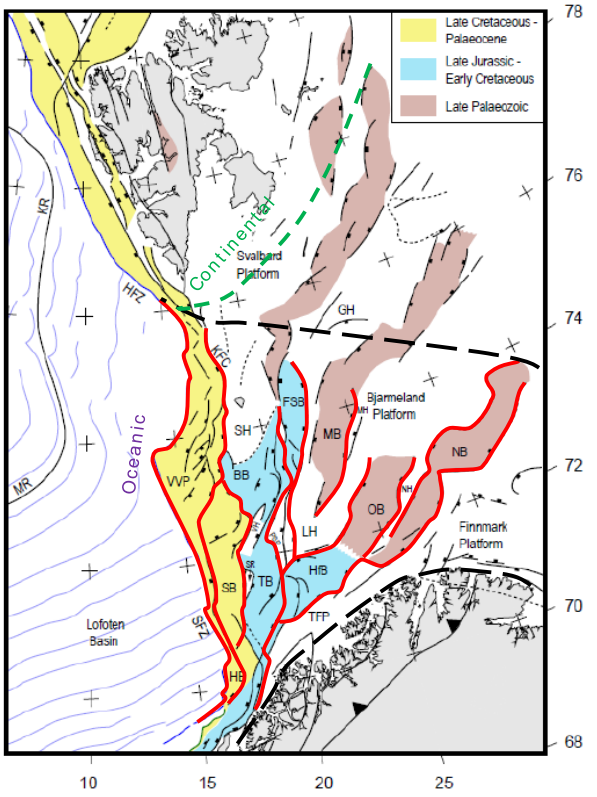

Fig. 2.: Major structural elements of the western Barents Sea and bordering areas (after Gabrielsen et al., 2010).

Numerical tools and modelling approaches

The numerical tools used for this study are Finite-Element Method Code-Aster & Salome Meca to simulate the stresses and displacement in the study area and the SORTAN to predict the sense of potential slip along the major fault planes.

CODE_ASTER

Code-Aster is a Finite Element Analysis code used for the study of the mechanical behavior of different structures. It can handle mechanical, thermal and associated phenomena in all sort of analysis. The code is capable to solve the problems related to all type of linear and non-linear statics e.g. 3D, 2D, beams, pipes, multi fibers, discrets, shells and plates etc. It produces a set of result files after given the appropriate data files set but without any colorful post processing images.

SALOME is open-source software that provides a generic platform for pre- and post-Processing for numerical simulation and is the integration of the Code-Aster solver in Salome platform. In figure 3 the deformation energy of a rock volume is minimized, assuming displacement constraints on some parts. Rocks follow linear elasticity and displacement constraints are used to input geological constraints. Finally finite element meshes are used to discretize the equations and Code-Aster is used to perform computations.

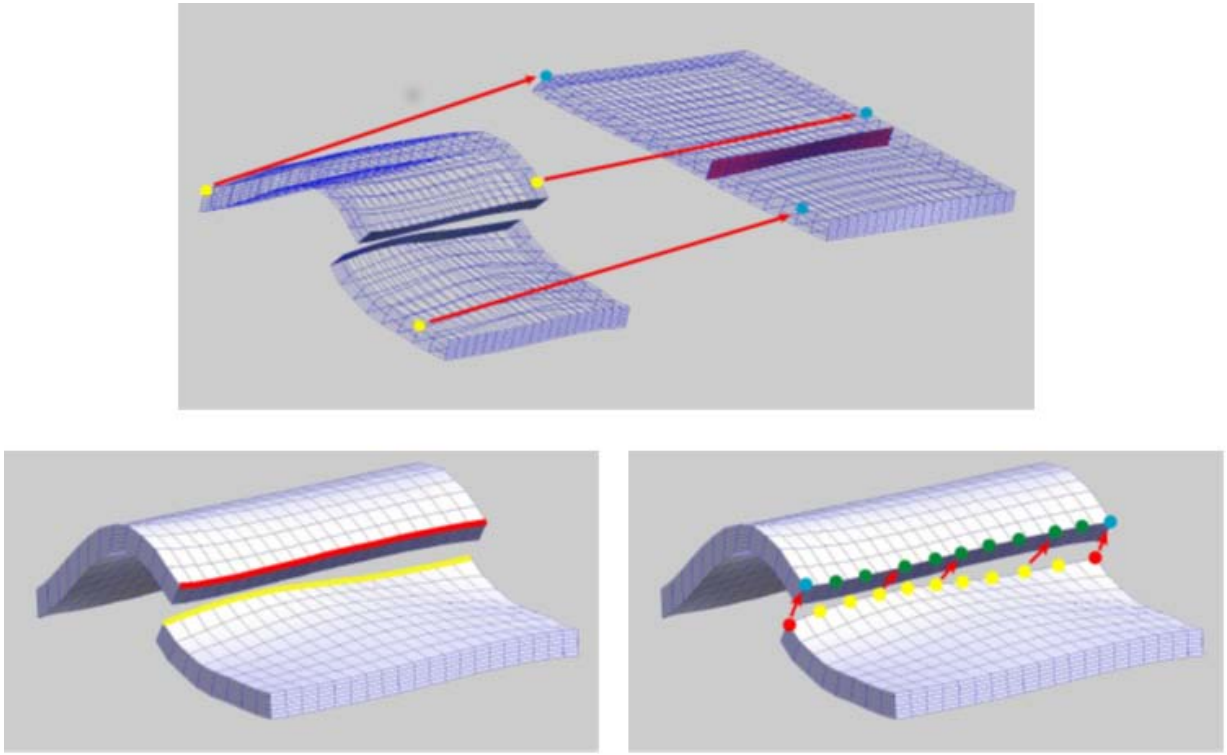

Fig. 3.: Expected results of the research showing inverted fault closure (after Rudkiewicz et al., 2009)

The SORTAN Method

SORTAN is used to calculate the sense of slip which is induced by stresses along fault planes (Pascal 2004). The method is based on the "Wallace-Bott" assumptions: that the slip on fault surfaces occurs parallel to the applied shear stress, faults are planar, blocks are rigid along the fault surfaces neither stress perturbations nor block rotations occur and applied stress state is stable for all tectonic events.

The input numerical parameters required for SORTAN are the azimuth θ and the shape ratio ϕ to describe the applied stress state and dip direction d and the dip angle p to describe the geometry of the fault.

Different fault complexes according to their respective ages of activation and reactivation have been selected (Figure 2). The selection of these fault systems is based on their orientations, structural style (basement involved, hard/soft-linked, salt influence, etc.), timings and evolution with respect to local and regional tectonic events.

References

Barrère, C., J. Ebbing, and L. Gernigon (2009), Offshore prolongation of Caledonian structures and basement characterization in the western Barents Sea from geophysical modelling, Tectonophysics, 470(1–2), 71–88.

Christophe Pascal and Roy H. Gabrielsen (2001) Numerical modeling of Cenozoic stress patterns mid-Norwegian margin and the northern North Sea. Tectonics, Vol. 20, No. 4, Pages 585-599.

Doré, A. G. (1991), The structural foundation and evolution of Mesozoic seaways between Europe and the Arctic, Palaeogeogr. Palaeoclimatol. Palaeoecol., 87(1–4), 441–492.

Faleide, J. I., A. Solheim, A. Fiedler, B. O. Hjelstuen, E. S. Andersen, and K. Vanneste (1996), Late Cenozoic evolution of the western Barents Sea-Svalbard continental margin: Impact of glaciations on basin evolution, data and models from the Norwegian margin and adjacent

areas, Global Planet. Change, 12, 53–74.

Gabrielsen, R.H., Jensen, L.N., Kalheim, J.E. and Riss, F., 1990. Structural Elements of the Norwegian Continental Shelf–Part 1: The Barents Sea Region Norwegian Petroleum Directorate Bulletin, 6, 47.

Gernigon, L., M. Brönner, D. Roberts, O. Olesen, A. Nasuti, and T. Yamasaki (2014), Crustal and basin evolution of the southwestern Barents Sea: From Caledonian orogeny to continental breakup, Tectonics, 33, doi:10.1002 / 2013TC003439.

Jean-Pierre Aubry 2013. Beginning with Code_Aster, A practical introduction to finite element method using Code_Aster Gmsh and Salom. Version 1.1.1 LAL 1.3, GNU FDL 1.3 et CC By-SA 3.0e.

Pascal, C., 2004. SORTAN: a UNIX program for calculation and graphical presentation of fault slip as induced by stresses. Computers & Geosciences 30 (2004) 259–265 pp. 163–195, Geol. Soc., London.

Exploratory analog modeling of the effects of a morpho-rheological obstacle across a wrench fault system: the example of the Gloria Fault – Tore Madeira Rise intersection in NE Atlantic

F. M. Rosas[1,2], J. Almeida[2], F. Barata[2], B. Carvalho[2], P. Terrinha[3], J. Duarte[4], C. Kullberg[2], R. Tomás[2]

[1]*Instituto Dom Luiz, Campo Grande, Ed. C1, Piso 2, 1749-016 Lisboa, Portugal*
[2]*Universidade de Lisboa, Faculdade de Ciências, Departamento de Geologia, Campo Grande, Ed. C6, Piso 4, 1749-016 Lisboa, Portugal*
[3]*Instituto Português do Mar e da Atmosfera, 1749-077 Lisbon, Portugal*
[4]*School of Geosciences, Monash University, Melbourne, VIC 3800, Australia*
e-mail: *frosas@fc.ul.pt*
session: *Tectonics and Surface Processes*

Tectonic setting

Recent tectonic mapping of the intersection between the Gloria Fault (GF) and the Tore Madeira Rise (TMR) in NE Atlantic (Fig. 1A) revealed a newly unveiled pattern of conspicuous morphotectonic features (Fig. 1B). In the present work we use analog modeling to preview the type of structural pattern expected from such an interference, testing different assumptions regarding the geometry and rheology of the main features at stake.

The GF is a major active (dextral strike-slip) fault corresponding to the eastwards continuation of the Atlantic transform fault that marks the Eurasia-Africa (Nubia) plate boundary in NE Atlantic, also known as the Azores-Gibraltar Fracture Zone (AGFZ, e.g., Jiménez-Munt et al., 2001). A dominant overall right-lateral strike-slip kinematics has been ascribed to the GF, confirmed namely by historical and instrumental seismicity data including high magnitude earthquakes (e.g. M=7.1 and M=8.4 of 08/05/1939 and 25/11/1941 respectively, implying surface ruptures of the order of 250-300 km, Buforn et al., 1988) with complying focal mechanisms attesting the present day active tectonic nature of this fault.

The TMR is a ∼1000km long NE-SW elongated submarine ridge, extending between the Madeira archipelago (to the southeast) and the submarine Tore seamount (to the northwest), which age and origin remain debatable and yet not fully understand. Nevertheless, numerous diachronic manifestations of volcanism have been reported by several authors, comprising ages ranging from late Cretaceous to middle-late Miocene to Present day (Geldmacher et al., 2006; Grange et al., 2010). Wide-angle refraction studies suggest a rheological structure in compliance with thickened oceanic crust in isostatic equilibrium, formed as a result of a possible phase of anomalous high accretion in the Mid-Atlantic Ridge (Peirce and Barton, 1991).

The key area targeted for modelling in the present work (Fig. 1) corresponds to the site of intersection and tectono-magmatic interference between these two major features. Our primary motivation was the newly obtained morphotectonic mapping of this area (outlined in Fig. 1B), which prompted the need to better understand the apparent control exerted by the revealed specific tectonic setting and the spatial-

time distribution of the volcanic manifestations in the area.

Analogue modeling and discussion of preliminary results

The main question addressed by the preformed scaled analog modeling was to preview the type of structural pattern (fault distribution and morphological variation) that is expected to be developed as the result of the intersection of a right-lateral strike-slip fault (accounting for the Gloria Fault system), and a morpho-rheological anomaly (accounting for the TMR). In our models it is assumed that this TMR anomaly corresponds to a softer crustal domain (e.g. with a mean viscosity closer to the one generally ascribed to the asthenosphere), and that the GF strike-slip propagates across such an anomaly from a brittle (crustal oceanic) medium.

We used the Perspex apparatus and the experimental initial configuration depicted in figure 2, using sand as a Coulomb-Mohr brittle analogous of the (oceanic) upper crustal behavior, and a scaled mixture of silicone putty (PDMS) and Wolframite powder to mimic the mechanical behavior hypothetically assumed for the TMR.

Top view photographs of the accommodation to successive wrenching increments are shown in figure 3. The main results reveal a monoclinic-like symmetry in the distribution of the main compressive and extensional structures (thrusts or graben-like/pull apart basins, respectively), which is broadly comparable to what happens in the natural example. Although a detailed geometrical correspondence is not always observed, a mechanical similitude concerning the bulk kinematics (and dynamics) at stake is possible to envisage. This is essentially manifested by the observation that the sites of silicone vertical extrusion, accounting for the volcanic highs and plugs in the natural example, are consistently coincident with the areas of intersection/confluence between the main faults and the main rheological boundaries.

Future work

Ongoing further upgrade of the experiments comprises varying the geometric and rheological configuration, considering: a) a more realistic angle of intersection ($\sim 115^{\circ}$) between the GF and the TMR; b) performing an experiment (strictly for benchmark comparative purposes) in which the considered TMR anomaly corresponds merely to a morphological anomaly, i.e. without any viscosity contrast; c) considering the existence of smaller rheological anomalies (working as localized seeds) aligned on top of the basement (GF) fault trace, embedded in the brittle medium represented by the sand.

Acknowledgements

This work was sponsored by the Fundação para a Ciência e a Tecnologia (FCT) through project MODELINK EXPL/GEO-GEO/0714/2013.

References

Buforn, E., Udias, A., and Colombas, M.A., 1988. Seismicity, source mechanisms and tectonics of the Azores-Gibraltar plate boundary. Tectonophys, 152(1-2), 89-118.

Geldmacher, J., Hoernle, K., Klugel, A., Bogaard, P. Wombacher, F., and Berning, B., 2006. Origin and geochemical evolution of the Madeira-Tore Rise (eastern North Atlantic). Journal of Geophysical Research 111, B09206, doi: 10.1029/2005JB003931.

Grange, M., Scharer, U., Merle, R., Girardeau, J. and Cornen, G., 2010. Plume Lithosphere Interaction during Migration of Cretaceous Alkaline Magmatism in SW Portugal: Evidence from U-Pb Ages and Pb-Sr-Hf Isotopes, 51(5), 1143-1170.

Jiménez-Munt, I., M. Fernandez, M. Torne, and Bird, P., 2001. The transition from linear to diffuse plate boundary in the Azores-Gibraltar region: Results from a thin-sheet model, Earth Planet. Sci. Lett., 192, 175– 189.

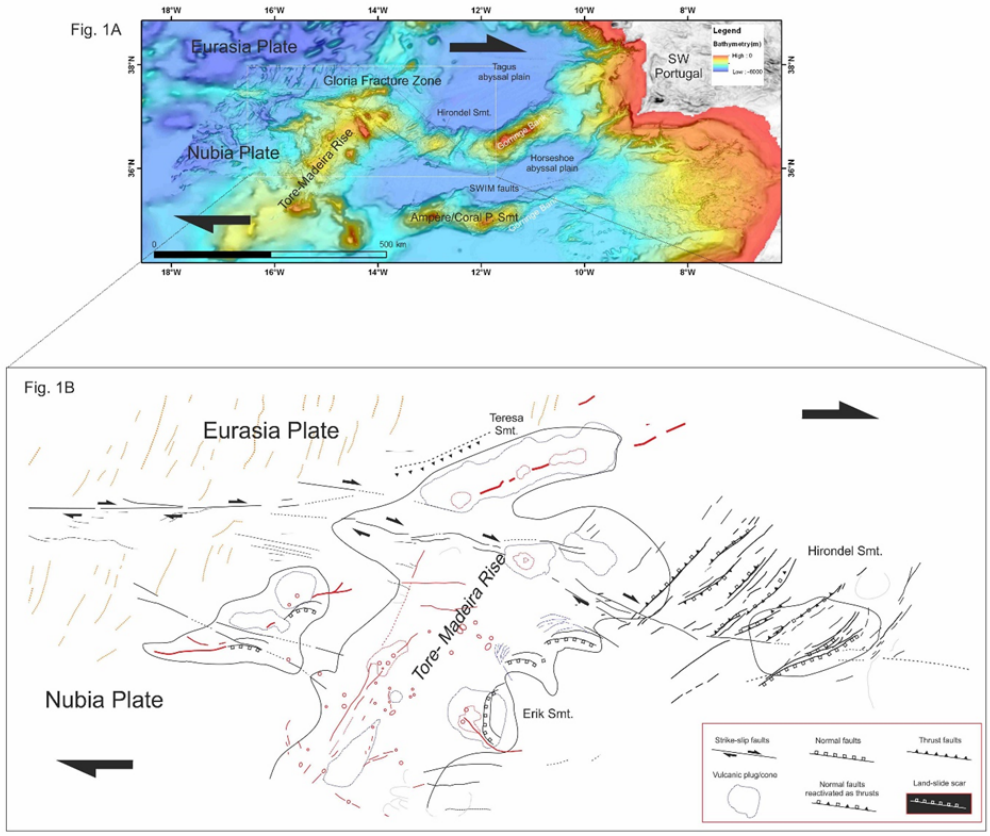

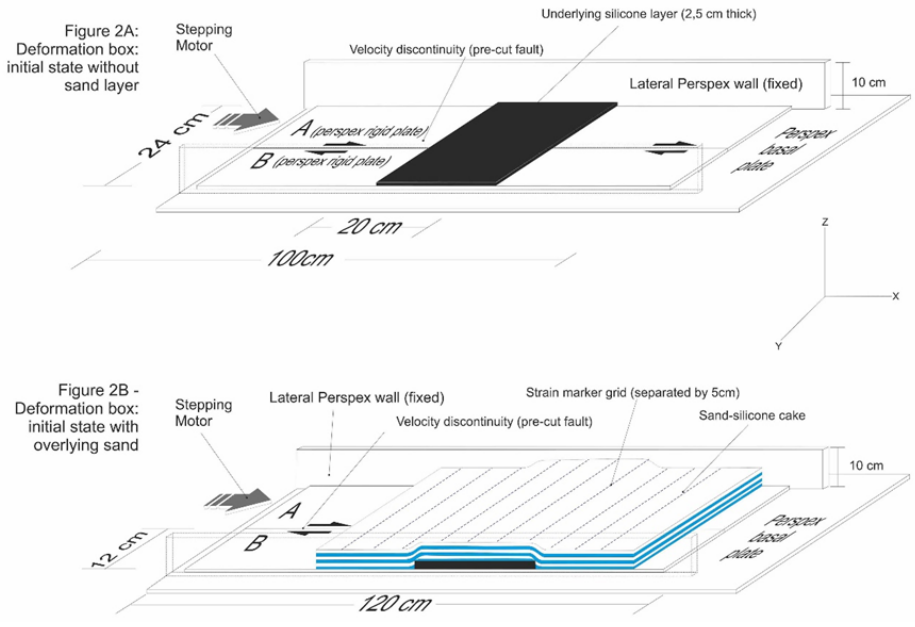

Fig. 1.: (top) A) General morpho-tectonic map of the study area; B) Detailed tectonic map (structural outline) of the key area targeted in the carried out modeling. **Fig. 2:** (bottom) Used Perspex deformation apparatus and experimental initial stage.

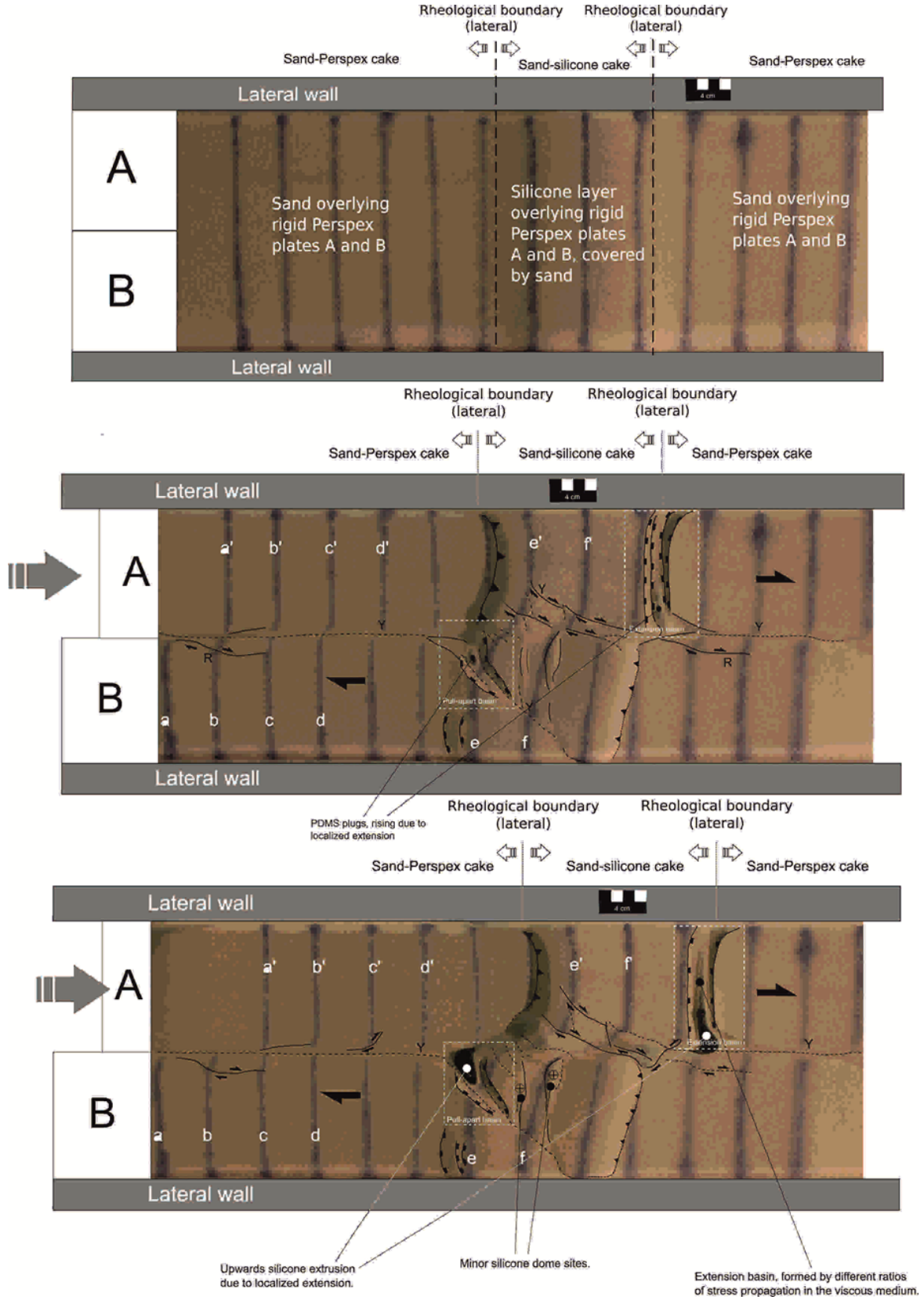

Fig. 3.: Experimental results for different incremental stages of deformation

Peirce, C., and Barton, P.J., 1991. Crustal structure of the Madeira-Tore rise, eastern North Atlantic - results of a DOBS wide-angle and normal incidence seismic experiment in the Josephine Seamount region, Geophys. J. Int., 106(2), 357-378.

DANSER: an open source surface evolution code beyond coupling with tectonic models

Sarah Schroeder[1], Richard Gloaguen[2], Jens Tympel[1], Andrey Babeyko[1], Stephan V. Sobolev[1]

[1] *GFZ Potsdam, Germany*
[2] *Bergakademie Freiberg, Germany*
e-mail: *sarah.schroeder@gfz-potsdam.de*
session: *Tectonics and Surface Processes*

Summary

We introduce the open source 2D Surface Evolution Code DANSER (Detachment limited lateral Abrasion Nonlinear diffusion Surface Evolution Routine). The code is intended to be coupled to any lithospheric scale (thermo-)mechanical code, and also to be applied to real Digital Elevation Models (DEM). Selected examples with analytically imposed uplift demonstrate that the code is able to simulate river capturing, induced by fault-bounded block rotations. In presented work, we highlight challenges and advances of the coupling to (thermo-)mechanical codes.

Introduction

First coupled lithospheric scale (thermo-)mechanical and Surface Evolution Models (SEM) were developed in the nineties (Beaumont et al., 1992, Willett, 1999). 2D thermo-mechanical codes were coupled with 1D (Willett, 1999) or 2D (Beaumont et al., 1992) surface evolution. Nevertheless, 3D (thermo-)mechanical codes are required to study more complex processes like continental collision. Since the influence of surface erosion on tectonics is not well understood, a coupled model of 2D surface evolution and 3D lithospheric scale (thermo-)mechanics (e.g. CASQUS, Kurfeß and Heidbach, 2009) could illuminate this topic.

DeLong et al. (2007) makes first attempts to adapt SEM to DEM. He applies the bifurcation method (Freeman, 1991; Pelletier, 2004) with different erosion parameters to a simulated plane. Further, he compares landslide threshold slope, drainage densitiy, relief and other topographic characteristics of the resulting topographies to a DEM of a field site in southern California. Accordingly, he chooses the input parameters of the best fit model as scaling values. The mentioned scaling parameters are used for surface evolution studies on the DEM.

It is of major importance for the scaling that the SEM is able to simulate flexible river networks. The bifurcation method makes this possible for small slopes (e.g. fans), but is not able to reflect this behaviour for steeper ones. E.g. in the Pamir orogen, the valley of the main river Panj is much broader than the stream. Nevertheless, the Panj laterally abrades the whole valley.

Simulations of river capturing events are widely studied. Approaches range from simple incision models (Garcia-Castellanos, 2002) without channel initiation function (Willgoose et al., 1991; O'Callagan and Marc, 1984) to finite-element models that compute the location of the drainage divide between every two neighbouring nodes (Castelltort et al., 2012). The challenge for every modeler is to find a balance between simple and fast algorithms on one hand, yet include complicated algorithms that capture processes that reflect the observations on the other hand.

Computational algorithm

DANSER is a Surface Evolution Code (SEC) that becomes open source available by the end of the year. It is designed for coupling with any lithospheric scale (thermo-)mechanical code. Furthermore, it can be applied to Digital Elevation Models (DEM).

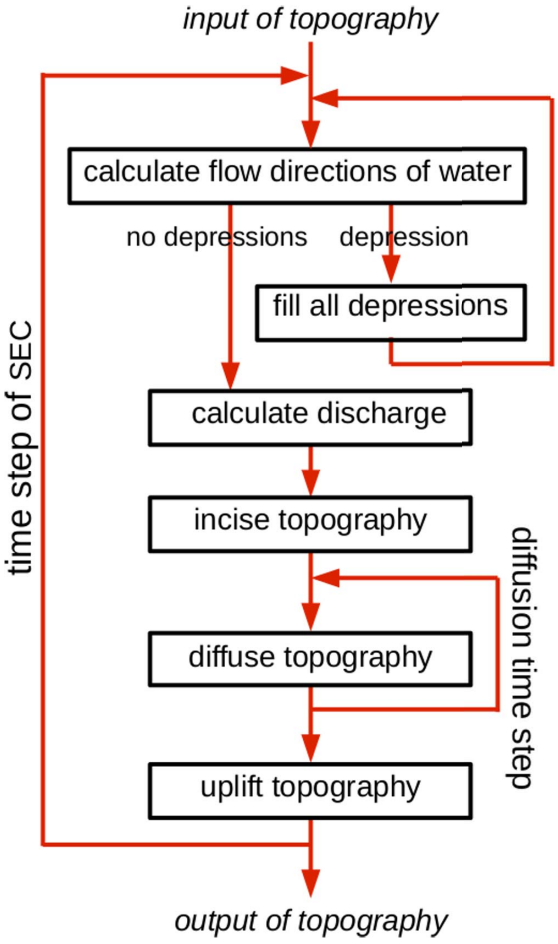

Fig. 1.: Flowchart of the 2D surface evolution algorithm DANSER. The red arrow on the left symbolizes the surface evolution time steps, the short one on the right the diffusion steps. The algorithm performs the filling cycle (arrow in the upper right corner) maximal once, if it is needed.

The routine follows the concept of the cellular automaton (Beaumont et al., 1992), implemented on a regular Eulerian grid. Fig.1 presents a flowchart of the routine. It comprises the D8 algorithm (O'Callaghan and Marc, 1984) for computation of flow directions and a new and fast filling algorithm (Planchon and Darboux, 2001), to get rid of topographic depressions. The new accumulation routine for water discharges works without time consuming sorting algorithm. It is a slightly transformed and faster version of O'Callaghan and Marks (1984) drainage accumulation algorithm. The supply limited incision code is based on the accepted stream power law. It includes a new algorithm to spread the water discharge over several cells, dependent on the distance, the height difference and the water discharge. This method leads to lateral abrasive rivers and may substitute the bifurcation method. Furthermore, we extend Beaumont's implementation (Beaumont et al., 1992) of the diffusion equation to nonlinear diffusion. We decouple incision from diffusion with the benefit of a simpler calibration and a reduction of filling.

The code automatically adjusts incision and diffusion time steps in order to stabilize the algorithms. Since one incision time step, including computation of flow directions and water discharges, is more time consuming than the computation of a diffusion step, we refine each incision step into multiple diffusion steps.

Special features, including the new lateral abrasion routine and the immediate removal of diffused material from the river bed, can be switched on and off in order to adapt DANSER to given challenges.

Coupling to lithospheric scale (thermo-)mechanical codes

To execute one time step of a tectonic code consumes remarkably more time than running a step of a SEC. Beside that fact, a SEM, especially riverbed incision, needs a finer resolution than a tectonic model to reflect surface processes sufficiently. As a consequence, a refinement of time steps and resolution should be implemented in a modern SEC, made for coupling to any tectonic code.

Fig. 2 presents the coupling of DANSER to tectonic codes. Before the initial tectonic time step,

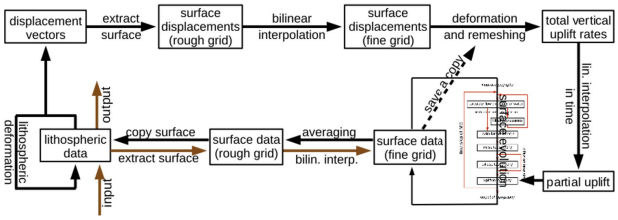

Fig. 2.: Coupling of DANSER to any tectonic code. Boxes indicate diverse data matrices and arrows illustrate methods of data computation. The dashed arrows symbolize data storage for the next time step. The brown arrows mark methods that are just performed in the first tectonic step.

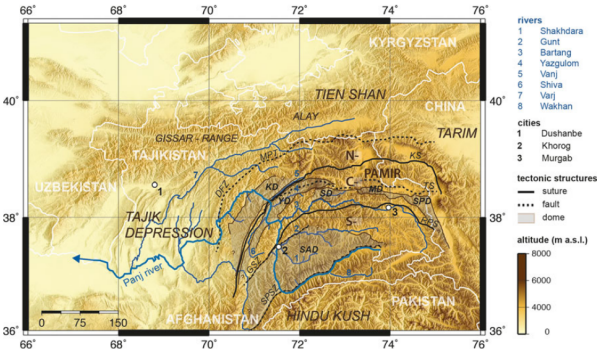

Fig. 3.: Topographic map of the Pamir orogen. Rivers are drawn in blue and faults in black. (Fuchs et al., 2013)

the surface elevations are extracted and bilinearly interpolated to a finer resolution. This fine resolution grid with elevation data gets stored for the first surface evolution time step. In every following tectonic step, three dimensional displacement vectors pass the surface deformation data from the tectonic code to the SEC. These vectors serve, interpolated to the fine resolution surface grid, for evaluation of the uplift rates. DANSER continues with alternating uplift and erosion in finer time steps. Subsequently, the resulting fine resolution elevation data get stored in a static array for the next time step. Finally, averaged to the deformed tectonic mesh, the elevation data modify the surface coordinates of the underlying model. Accordingly, the tectonic code performs the next time step.

Application 1: River capturing in the Pamir

The highly active Pamir orogen is penetrated by sub-parallel faults. The main rivers of the Pamir flow from east to west, following the fault system (fig. 3). They join the river Panj, that abruptly turns at 71.5° longitude from east-west direction to the north. An old river bed in direction to south-west can be observed at the sudden turn. It is unknown, how strong such a fault system influences a river network. Might the Panj river have changed its direction due to a river capturing event, induced by a recently forming fault?

This numerical study aims to clarify if and how a system of faults may influence the development of a river network. We simulate the effect of varying angles between riverbed and faults on river flow direction, and study for which configuration a deflection of the river is possible. We also compare the influence of uplift and high erodibility zones on the deviation of the river networks.

We simulate an inclined plane with white noise and five faults, arranged from east to west. The direction of inclination defines the main flow direction of the arising rivers. We study fault-bounded block rotations that are modelled as regions of increased erodibility and analytically imposed uplift. Fig. 4 shows a river capturing event, enabled by the new lateral abrasion routine.

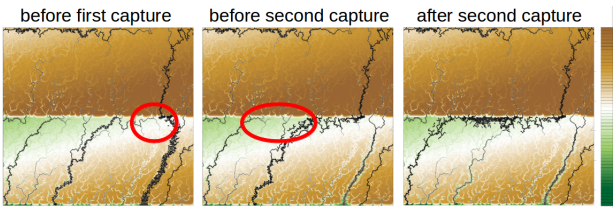

Fig. 4.: Simulation of a river capturing event. Three time steps illustrate the rapidity of two capturing events in a row. Colours illustrate the topographic relief (brown: high, green: low). The main streams are marked in black.

Application 2: Coupling to Slim3D

SLIM3D is a three-dimensional lithospheric-scale thermo-mechanical C++ based code (Popov and Sobolev, 2008). It allows modelling of lithospheric deformation with an elasto-visco-plastic rheology with diffusion, dislocation, Peierls creep mechanisms and Mohr–Coulomb plasticity. The code incorporates an arbitrary Lagrangian Eulerian formulation with free surface and Winkler boundary conditions.

We couple DANSER to Slim3D and present a coupled model of plateau growth. Challenges and advantages of the coupling method are discussed.

References

Beaumont, C., Fullsack, P., Hamilton, J. (1992), Erosional control of active compressional orogens, in McClay, K. R., ed, Thrust tectonics: New York, chapman and Hall, 1-18

Castelltort, S., Goren, L. , Willett, S. D., Champagnac, J. D., Herman, F. and Braun, J. (2012), River drainage patterns in the New Zealand Alps primarily controlled by plate tectonic strain, Nature Geosciences, 5, 744-748

DeLong, S. B., Pelletier, J. D., Arnold, L. (2007), Bedrock landscape development modeling: Calibration using field study, geochronology, and digital elevation model analysis, GSA Bulletin, 119, 157–173, doi: 10.1130/B25866.1

Freeman, T. G. (1991), Calculating catchment area with divergent flow based on a regular grid, Computers and Geosciences, 17, 413-422

Fuchs, M. C., Gloaguen, R., Pohl, E. (2013), Tectonic and climatic forcing on the Panj river system during the Quaternary, Int J Earth Sci, doi: 10.1007/s00531-013-0916-2

Garcia-Castellanos, D. (2002), Interplay between lithospheric flexure and river transport in foreland basins, Basin Research, 14, 89-104

O'Callagan, j. F. and Mark, D. M. (1984), The Extraction of Drainage Networks from Digital Elevation Data, Computer vision, graphics, and image processing, 28, 323-344

Pelletier, J. D. (2004), Persistent drainage migration in a numerical landscape evolution model, Geophysical Research Letters, 31, L20501, doi:10.1029/2004GL020802

Planchon, O. and Darboux, F. (2001), A fast, simple and versatile algorithm to fill the depressions of digital elevation models, Catena, 46, 159–176

Popov A. A. and Sobolev, S. V. (2008), SLIM3D: A tool for three-dimensional thermomechanical modeling of lithospheric deformation with elasto-visco-plastic rheology, Physics of the Earth and Planetary Interiors, 171, 55–75

Willett, S. D. (1999), Orogeny and orography: The effects of erosion on a structure of mountain belts, Journal of Geophysical Research, 104, 28,957-28,981

Willgoose, G, Bras, R. L. and Rodriguez-Iturbe, I. (1991), A Coupled Channel Network Growth and Hillslope Evolution Model, Water Resources Research, 27, 1671-1684

Kinematic reconstruction of the hastings block, southern New England Orogen, Australia

Yan, Jie[1], Lennox, Paul[1], Kelly, Bryce F.J.[1], Offler, Robin[2]

[1]*School of BEES, The University of New South Wales, Sydney 2052, NSW, Australia*
[2]*New South Wales Institute of Frontiers Geoscience, University of Newcastle, NSW 2308*
e-mail: *z3371716@student.unsw.edu.au*
session: *Tectonics and Surface Processes*

This research project uses 3D geological modeling software to build a 3D structural surface model of the Permo-Carboniferous rocks in the northern Hastings Block (NHB) [1] (Figure 1). The model is being built using comprehensive strike and dip structural data and a digital elevation model. It is designed to unravel a comprehensively mapped, complexly folded, extensively faulted geological sequence where there are no well-log data. It is believed that this new workflow will be widely applicable in the oil, gas, mining, and groundwater sectors.

Several tectonic models have been proposed to explain the structural and tectonic development of the Hastings Block which is outboard of similar Carboniferous fore-arc basin sequences in the Tamworth Belt, Australia. Mechanisms of development include emplacement either by faulting with or without rotation [2,3], or rotation during folding of the southern section of the Tamworth Belt [4,5,6]. The new 3D model will enable testing of the validity of these existing tectonic models. It will assist in constraining the relative timing of fault development, testing fault emplacement of the block, and verification of the number and orientation of folding events in the NHB.

The NHB is dominated by an open, $\sim$ 40 x 30 km NW-trending dome with the dominant fold axis plunging gently northwest [1]. It has been extensively faulted and possibly rotated after some fault developments (Figure 2). Construction of the 3D model fault-block by fault-block (Figures 3, 4 and 5) has highlighted shortcomings with the existing geological map of the NHB [7]. These include the variability in the orientation of bedding within some fault blocks, between adjacent fault blocks, and around significant sections of the dome. This is clearly illustrated in the Birdwood Fault Block (Figure 5), a fault-bounded block of Devonian-Carboniferous sequences on the SW limb of the dome that contains sequences facing northwest. In contrast, the surrounding rock sequences face northeast (Leitch E.C. pers.comm.) or possibly southwest [7] suggesting at least 90° rotation during emplacement.

Resolution of these challenges requires the reappraisal of the simple dome model for the NHB. Each fault in the NHB is being analyzed systematically to determine the duration of faulting, apparent sense of movement, and the relationship to other faults and the folds (Figure 2). The fault history plays an important role in building backward and forward models. Comparison between the cross-sections constructed from the 3D model (Figure 4) and those from the existing fieldwork provide better constraints on the validity of the 3D model.

References

[1] Lennox P.G., Roberts J. & Offler R., 1999, Structural analysis of the Hastings Terrane. In Flood, P.G. ed. New England Orogen, Eastern Australia: Regional Geology, Tectonics and Metallogenesis 115-124.

[2] Cawood P. A. & Leitch E. C., 1985, Accretion and dispersal tectonics of the southern New England Fold Belt, eastern Australia, Tectonostratigraphic Terranes of the Circum-Pacific Region, 1, 481-492.

[3] Schmidt P.W., Aubourg C., Lennox P.G. & Roberts J., 1994, Palaeomagnetism and tectonic rotation of the Hastings Terrane, eastern Australia, Australian Journal of Earth Sciences, 41, 547-560.

[4] Cawood P. A., Pisarevsky S. A and Leitch E. C., 2011a, Unraveling the New England orocline, east Gondwana accretionary margin, Tectonics, 30, TC5002, doi:10.1029/2011TC002864.

[5] Rosenbaum G., Li P. and Rubatto D., 2012, The contorted New England Orogen (eastern Australia): new evidence from U–Pb geochronology of early Permian granitoids, Tectonics, 31, http://dx.doi.org/10.1029/2011tc002960 (TC1006).

[6] Korsch R. J. & Harrington H. J., 1987, Oroclinal bending, fragmentation and deformation of terranes in the New England Orogen, eastern Australia, Terrane Accretion and Orogenic Belts, American Geophysical Union Geodynamic Series, 19, 129-140.

[7] Roberts J.R., Leitch E.C., Lennox P.G. & Offler R., 1995, Devonian - Carboniferous Stratigraphy of the Southern Hastings Block, eastern Australia, Australian Journal of Earth Sciences 42, 609-634.

[8] Glen R.A., Roberts, J., 2012, Formation of oroclines in the New England Orogen, Eastern Australia, J. Virtual Explor, 43 (Paper 3), http://dx.doi.org/10.3809/jvirtex.2012.00305.

[9] Crowell J.C., 1984, Notes to accompany lectures on tectonics, sedimentation and structural analysis of basins, Petroleum Exploration Society of Australia, 138-142.

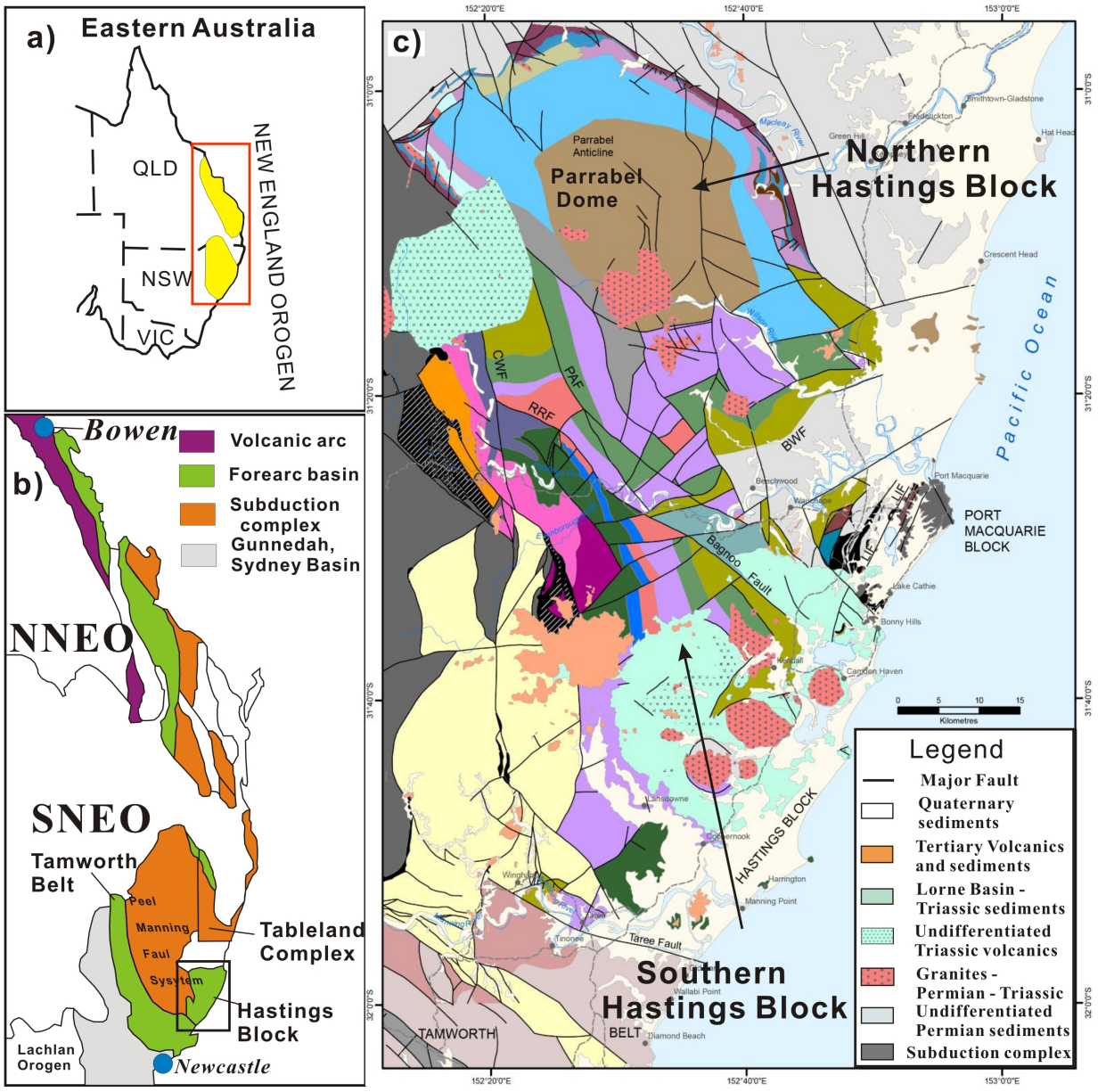

Fig. 1.: Location and tectonic setting of the Hastings Block (from Cawood et al. 2011 and Glen et al. 2012): (a) within eastern Australia, (b) within the southern New England Orogen. (c) major tectonic units and faults within and adjacent to the Hastings Block. (NNEO – Northern New England Orogen; SNEO - Southern New England Orogen).

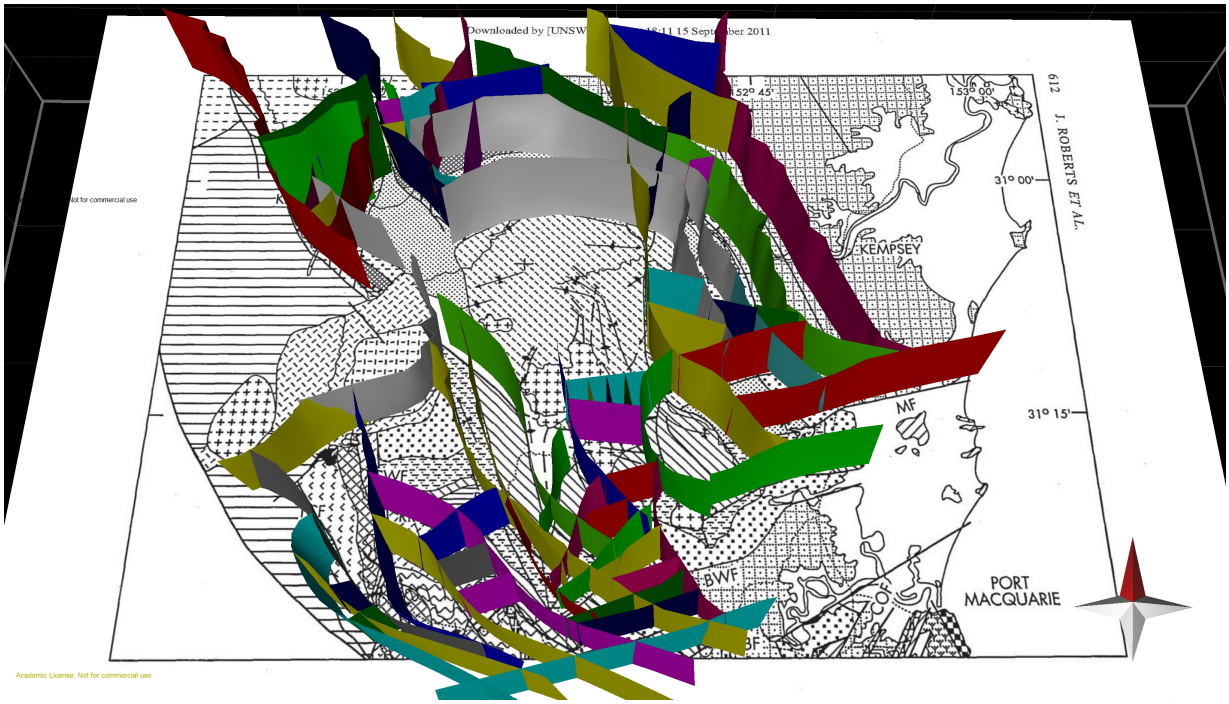

Fig. 2.: The preliminary 3D fault network model for the northern Hastings Block. This model was constructed using Leapfrog (www.leapfrog3d.com) and 3D MOVE (www.mve.com). At present all fault surfaces are vertical. The inclination of the fault surfaces will be adjusted to be consistent with both the geological information available from field studies and the literature, and the need to balance geological processes over the region.

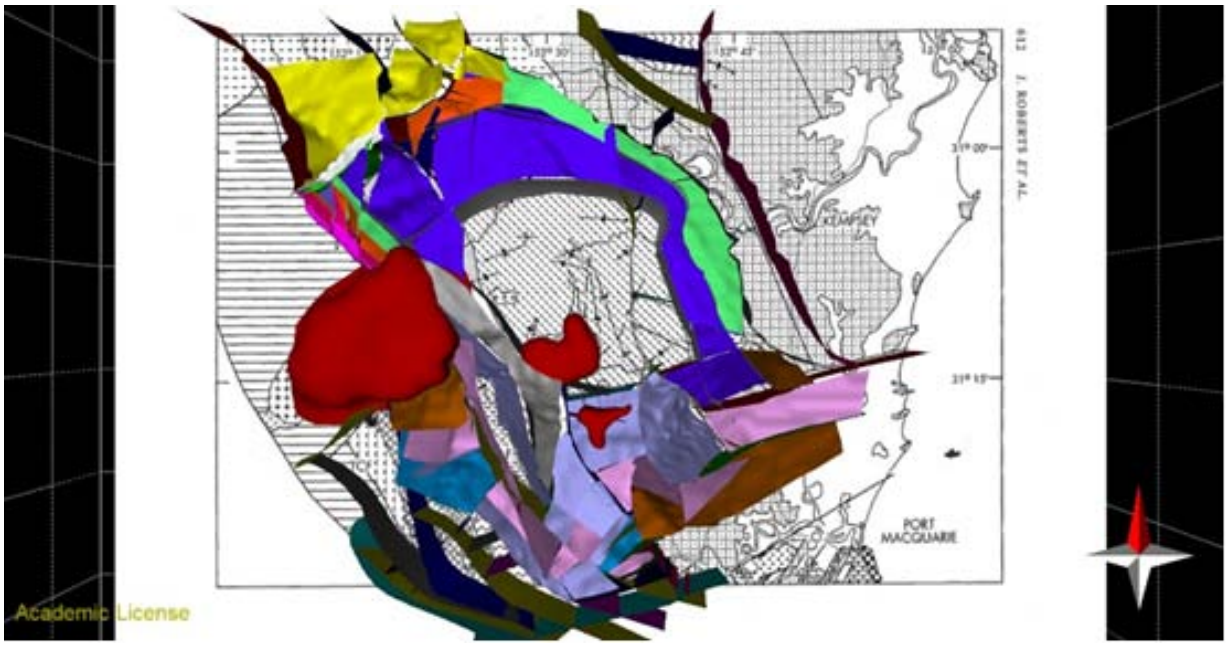

Fig. 3.: The 3D geological model of the northern Hastings Block showing selected geological horizons. Horizons are being constructed within each individual fault-block using a combination of field mapping data and the consideration of the requirements of balanced geological sections.

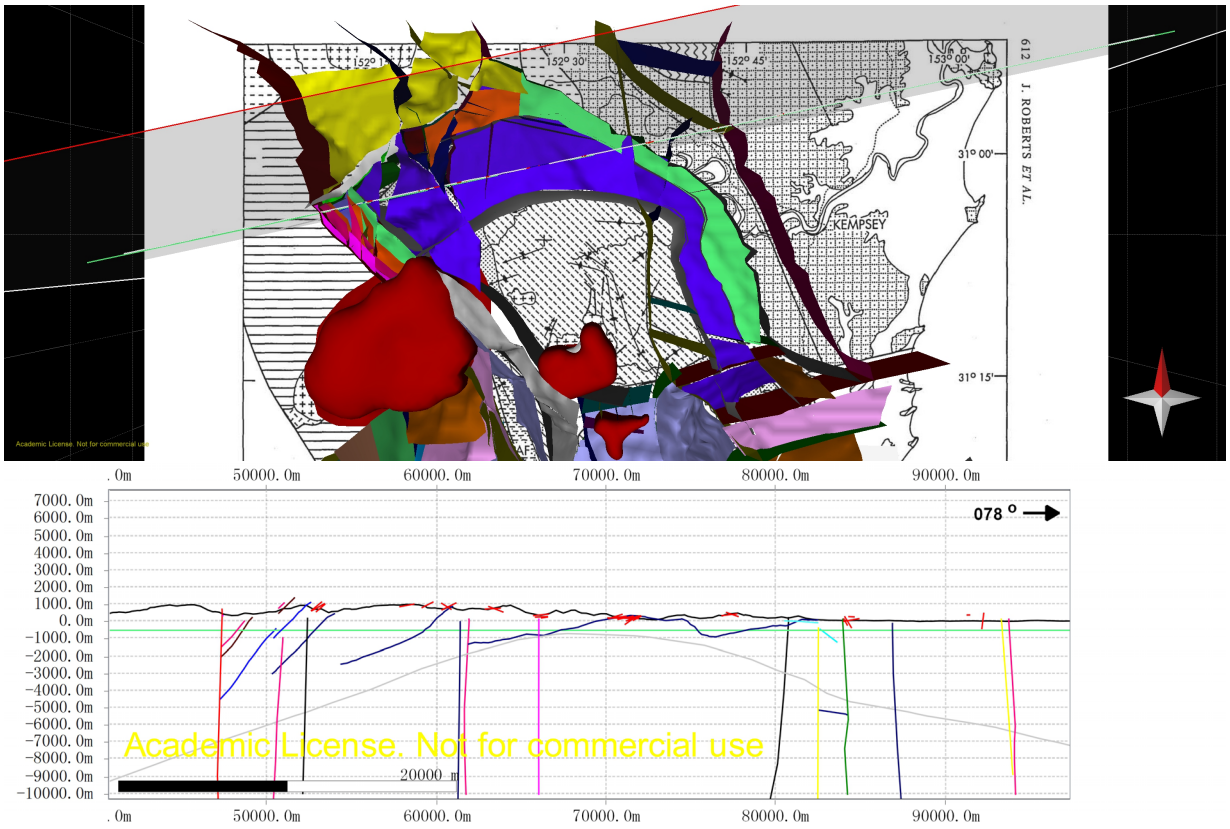

Fig. 4.: A preliminary cross-section extracted from the 3D geological model across the northern section of the Parrabel Dome. Such cross-sections highlight inconsistencies with the present fault and horizon interpretation. Through iterative interpretations, the goal is to develop a 3D geological model that is consistent with the field mapping data and known geological processes that occurred in the area.

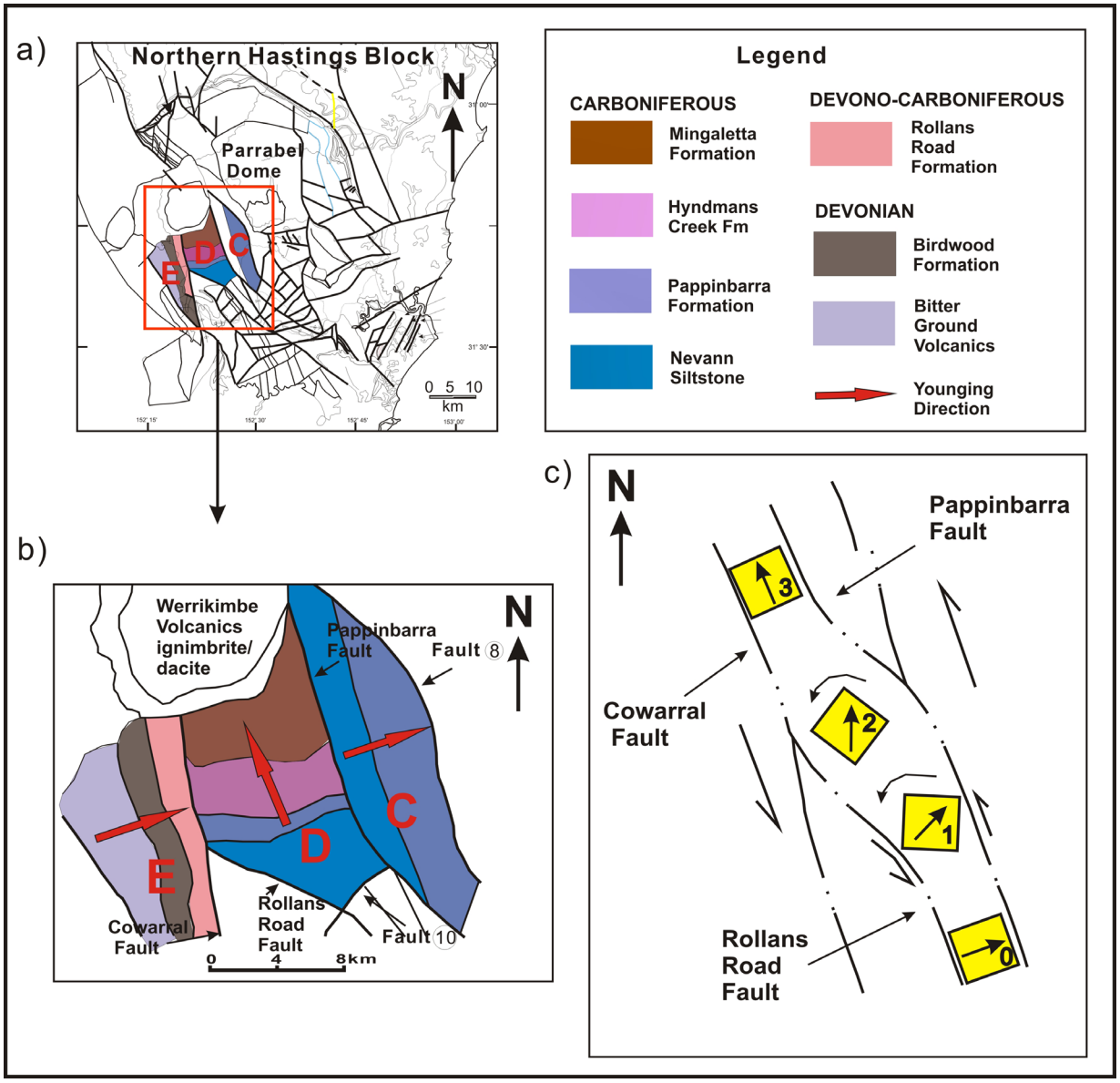

Fig. 5.: Location of the Birdwood Fault Block (Fault block D): (a) within Northern Hastings Block, (b) the surrounding rock sequences face east or west. (c) a possible model to explain how the Birdwood Fault Block experienced at least 90o rotation during it's emplacement (Adapted from Crowell, 1984).

Stability of over-pressured cohesive and frictional materials based on Sequential Limit Analysis

Xiaoping Yuan[1], Yves M. Leroy[1], Bertrand Maillot[3], Yves Guéguen[1]

[1]*Laboratoire de Géologie, CNRS, École Normale Supérieure, Paris, France*
[2]*now at Total, CSTJF, Pau, France*
[3]*Laboratoire Géosciences et Environnement Cergy, Université de Cergy-Pontoise, France*
e-mail: *xyuan@geologie.ens.fr*
session: *Tectonics and Surface Processes*

Summary

The gravitational collapse mechanism in over-pressured cohesive and frictional materials of arbitray topography and resting on an inclined weak décollement is examined by analytical means. The dominant mechanism consists in finding the length of the active décollement and the dips of the normal-fault and of the conjugate shear-plane composing the emerging half-graben, and the dips of the ramp and of the shear-plane bounding the frontal hanging-wall. The predictions of the maximum strength theorem (MST), part of the kinematic approach of limit analysis, not only match exactly the theoretical solutions, but generalises them in several aspects: failure geometry, composed of cohesive material, arbitrary topography and pre-existing faults. We show in particular that the MST predicts the failure geometry of the body triggerred by fluid over-pressure in a physical experiment. The evolution of the materials on the décollement is predicted with a two step method called sequential limit analysis. The first step is based on the above dominant mechanism. The second step leads to a modification of the geometry due to extensional fault-bend folds and compressional fold-thrust belts. The evolution simulation captures the main features of gravitational collapse of the sandbox analogue experiment.

Introduction

The geodynamics context of interest here is mainly extensional zones, motivated by the following examples : seismic reflection profiles documented many extensional wedges associated with normal-faults, such as the Brazos Ridge fault, offshore Texas [Xiao and Suppe, 1992; Withjack et al., 1995] and sequences of normal-faults in the convergent margin off Antofagasta [Delouis et al., 1998; von Huene and Ranero, 2003; Sallarés and Ranero, 2005]. The more complex Niger Delta shows the link between the extensional province on the shelf and the contraction in the toe-thrust systems in the deep water [Corredor et al., 2005; Kostenko et al., 2008]. Instabilities of compression/extension were also reproduced in the laboratory with sandbox analogue experiments [Mourgues et al., 2009; Lacoste et al., 2012].

The objective of this work is to propose a simple method to analyze the gravitational deformation occurring in over-pressured cohesive and frictional wedges extending the stability conditions presented by Lacoste et al., [2012] to an arbitrary-sloped topography, and cohesive materials. The kinematic approach of limit analysis, also called the maximum strength theorem (MST) [Maillot and Leroy, 2006], for compressional deformation [Cubas et al., 2008] and for the onset of gravitational instability in over-pressured materials [Yuan et al., 2014] is extended for that purpose.

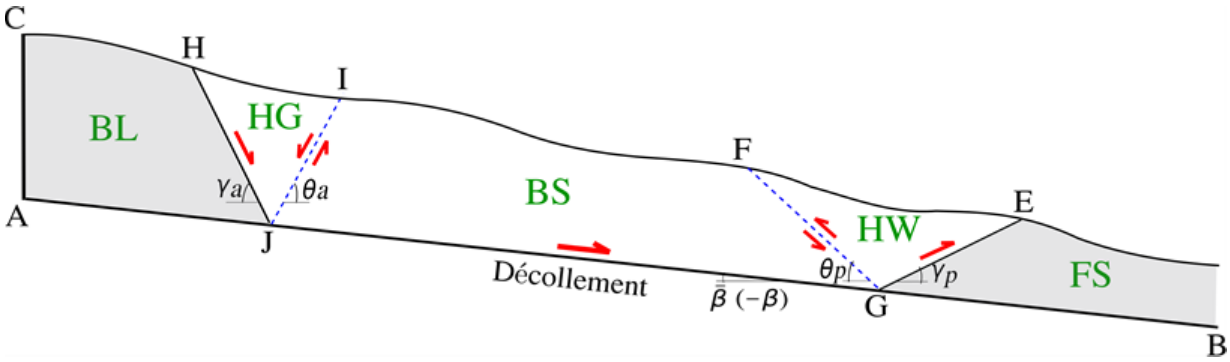

Fig. 1.: The prototype of gravitational instability composed of half-graben (HG), back-stop (BS) and hanging-wall (HW).

Prototype and of the collapse mechanism

The geometry of our prototype and of the collapse mechanism is presented in Figure 1. It consists of a slope of arbitrary topography resting on a décollement inclined (AB) at an angle β. The mode consists of the gravitational collapse by the action of two normal faults bounding a half-graben (HG) and two reverse faults composing a frontal hang-wall (HW), rooting on the décollement and completed by the seaward sliding of a back-stop (BS), the transition part of the materials. Materials within the HG are sliding on the normal-fault (JH dipping at γa) and part of the material is flushed through the conjugate shear plane (JI, dipping at θa). This flux has for consequence the push of the BS part of the slope seaward, as in Figure 1, parallel to the décollement. The HW bounded by a ramp GE dipping at γp and shear-plane GF dipping at θp is formed by the seaward movement of the BS.

Application of the maximum strength theorem (MST) requires now to maximise the difference between external effective power and maximum resisting power for the proposed velocity field in terms of the dips γa, θa, γp and θp and the length LJG. If that maximum difference power is negative, the system is stable, otherwise there is a quasi static or a dynamic instability and the optimum five parameters (γa, θa, γp, θp, LJG) define the dominant collapse mechanism.

Onset validation

It is now proposed to apply the collapse mechanism accounting for the slope parallel model. The arbitrary topography is simplified to be a straight line parallel to the décollement, e.g. $\alpha = \beta$ (Figure 2a), and h is the thickness between the topography and the décollement. The collapse length [LJG/h]c is compared with the theoretical collapse length from (9) in Lacoste et al. [2012]. The comparison of the MST (symbols) and theoretical results (curves) are presented in Figure 2b for two sets of décollement overpressure ratio λD = 0.6, 0.8 with the décollement friction angle ϕD = 10$\circ$ and bulk λB = λhydro = 0.5. They are coinciding with each other very well. The comparison is extended in Figure 2c which presents the optimum dips of active and passive faults according the two theories, keeping the décollement pressure ratio constant λD = 0.8. The theoretical dips (γac, θac, γpc, θpc) are provided by the method of the geometrical construction of Mohr's circles [Lehner, 1986] for the active and passive Rankine stress state. The two sets of predictions coincide exactly. Note that the sum of active faults $\gamma ac + \theta ac = 50\circ (= \pi/2 - \phi B)$ and passive dips γpc + θpc = 120$\circ$ ($= \pi/2 + \phi$B).

The dips of active faults are also validated by applying the MST to the sand-box experiment of Mourgues and Cobbold [2003] for the increase of décollement fluid ratio. The experimental set-up consists of rectangular glass box in which sand packs were built with a length 40 cm and the

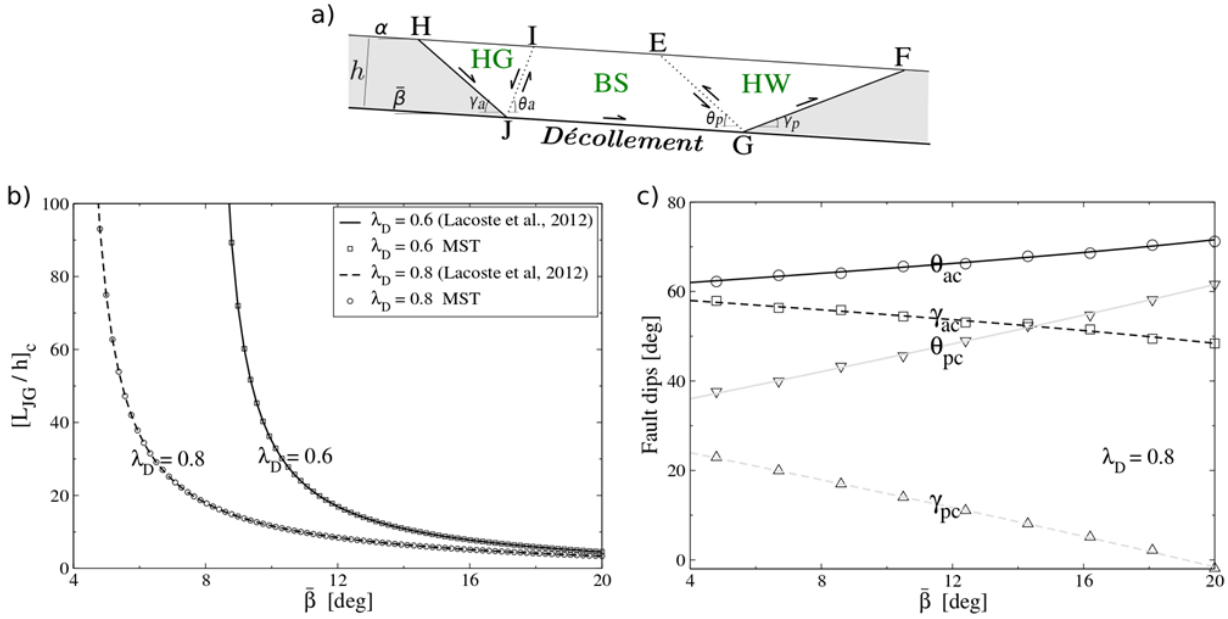

Fig. 2.: a) Illustration of the slope parallel model ($\alpha = \beta$). The validation for the collapse length ([LJG/h]c) and fault dips (γac, θac, γpc, θpc) keeping the bulk pressure ratio constant λB = 0.5 and décollement friction angle ϕD = 10∘. b). Collapse length [LJG/h]c as the function of décollement dip β. c). The dips of faults as the function of décollement dip β for the active and passive failure. The symbols are the predictions of maximum strength theorem and the curves are the theoretical results [Lacoste et al., 2012].

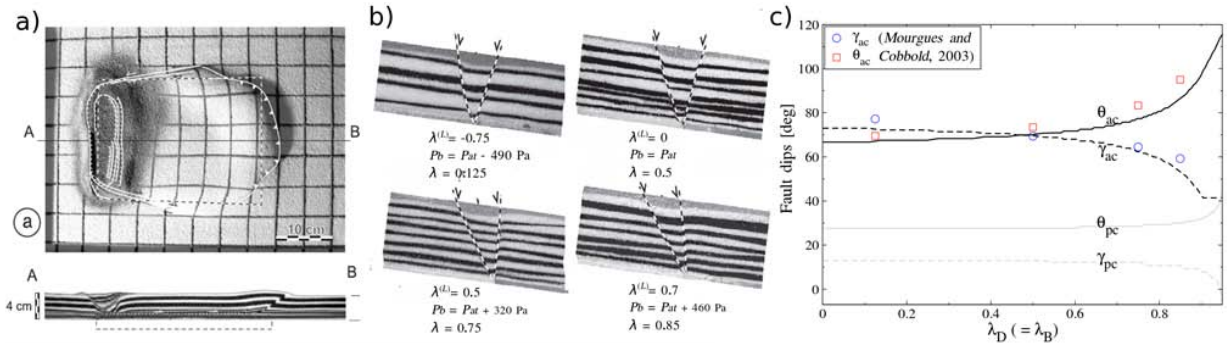

Fig. 3.: a) Gravitational collapse as a result of fluid overpressure from analogue experiments [Mourgues and Cobbold, 2003]. The extensional faults form by different air pressure, modified after Mourgues and Cobbold [2003], b). The comparison of extensional fault dips (γac, θac) from experiments and predictions from MST as function of fluid ratio, c).

height 4 cm, yielding a surface slope $\alpha = \beta = 6.7$∘. It rests on one overlapping sieve. Beneath the sieve was a pressure chamber, which acted as a reservoir for compressed air and provided a uniform air pressure (Pb) at the base of the model. Air flowed through the sand in a direction perpendicular to the slope, and the air pressures in upper chamber is Pup (atmospheric pressure Pat in this experiment). The uniform air pressure through the sand body in the experiment produced identical pressure ratios in the décollement and into the wedge : λB = λD [Mourgues and Cobbold, 2003; Lacoste et al., 2012; Pons and Mourgues, 2012]. The sand density ρs (1700 kg/m^3), the internal friction coefficient $\mu = 1.18$ (ϕB = 50∘) and the bulk cohesion (12 - 72 Pa)

are provided by the authors. We assume the cohesion CD = 0 Pa and the décollement friction can be any value (e.g. ϕD = 10$\circ$ in this analysis) since the active fault dips of interest are independent on this value. The experimental results and predictions from MST are presented in Figure 3c where the dips of faults are as function of fluid ratio λD (= λB). The experimental results show that the normal-fault dip γac (circle symbols) decreases and the shear-plane dip θac (square symbols) increases with the increases of fluid ratios. The theoretical results (γac, θac, black curves) present the same trend with the results of experiment. We conclude that the series of four experiments is well described by the MST despite the lack of passive fault dips γpc, θpc from the experiments for the comparison.

Evolution

The complete evolution is analyzed in Figure 4 which presents four stages revealing the processes of development. The material rests on a décollement with an initial topography slope $\alpha = \beta =$ 5$\circ$. The décollement fluid overpressure is applied in the red dashed box (Figure 4). The density of saturated material ρ = 2000 kg/m^3 (hydrostatic pressure ratio λhydro = 0.5), décollement ratio λD = 0.9 and bulk ratio λB = 0.7. The décollement friction angle ϕD = 10$\circ$ and material friction angle ϕB = 30$\circ$. The materials and interfaces are assumed cohesionless. The frontal part become thick by a series of three folds increasing in amplitude downdip, and the back region is thinned by a series of normal faulting. The deformation captures the main features of gravitational collapse of the analogue experiment in Figure 3a. The simulation was carried out until stability was reached, i.e., when the external effective power became less than the maximum resisting power The present approach does not allow us to determine the power of acceleration, and therefore we have no time scale to follow the evolution of a gravitational collapse. Comparison to more general methods accounting for inertia effect will be necessary to evaluate the adequacy of our quasi-static solutions.

Conclusion

The work proposes a mechanical analysis for extensional province and compressional toe inspired by the extensional fault-bend folds and compressional fold-thrust belts, respectively. This mechanism generalise in several aspects : fluid pressure, composed of cohesive material, arbitrary topography and failure geometry of the materials. We validate it by comparing with theoretical solutions and experimental results for the onset of failure. The evolution simulation captures the basic features of sandbox analogue experiments. Beyond the direct applications presented here, there are some perspectives the development of sequential limit analysis in other settings such as the sedimentation influence in Niger Delta [Corredor et al., 2005; Kostenko et al., 2008], the fluid ratio change with sedimentation, the effect of listric normal fault, and the weakening of pre-existing faults.

References

Cubas, N., Y. M. Leroy, and B. Maillot (2008), Prediction of thrusting sequences in accretionary wedges, Journal of Geophysical Research, 113 (B12), 1–21.

Delouis, B., H. Philip, L. Dorbath, and A. Cisternas (1998), Recent crustal deformation in the antofagasta region (northern chile) and the subduction process, Geophysical Journal International, 132, 302–338.

Lacoste, A., B. C. Vendeville, R. Mourgues, L. Loncke, and M. Lebacq (2012), Gravitational instabilities triggered byfluid overpressure and downslope incision insights from analytical and analogue modelling, Journal of StructuralGeology, 42 (0), 151 – 162.

Lehner, F. K. (1986), Comments on "Noncohesive Critical Coulomb Wedges: An Exact Solution by F. A. Dahlen, Journal of Geophysical Research, 91 (B1), 793–796.

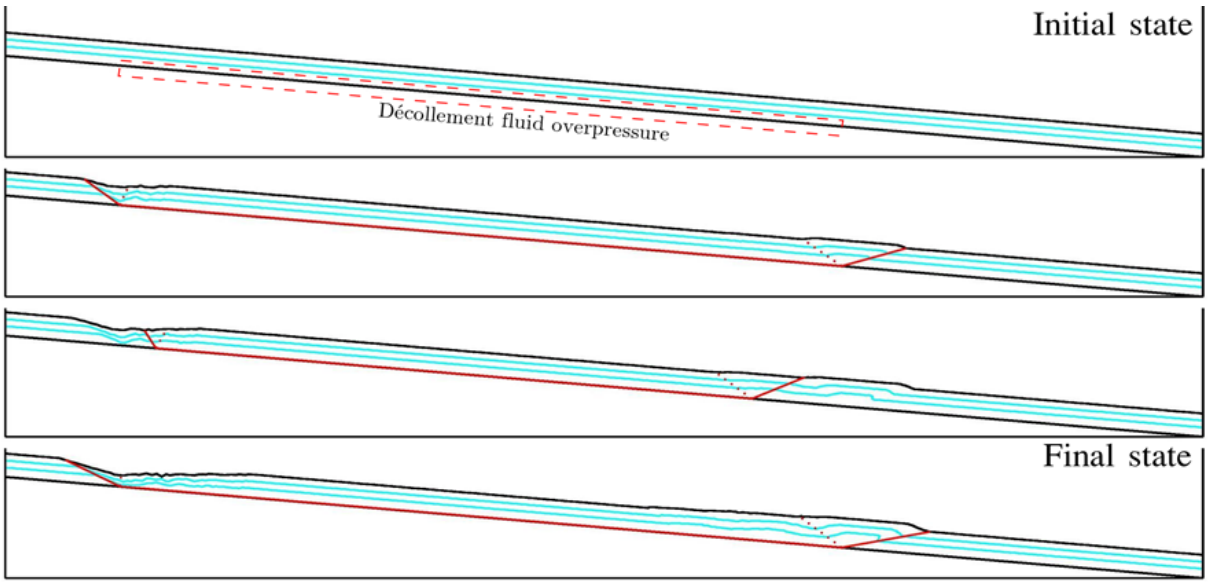

Fig. 4.: The complete evolution of the gravitational collapse triggered by an applied fluid over-pressure along the décollement (red dashed box). In the final state the material is stable for the applied over-pressure. Red lines show the current dominant mechanism. Blue lines representing the internal deformation are passive markers.

Maillot, B., and Y. M. Leroy (2006), Kink-fold onset and development based on the maximum strength theorem, Journal of the Mechanics and Physics of Solids, 54 (10), 2030–2059. Mourgues, R., and P. Cobbold (2003), Some tectonic consequences of fluid overpressures and seepage forces as demonstrated by sandbox modelling, Tectonophysics, 376, 75–97.

Mourgues, R., E. Lecomte, B. Vendeville, and S. Raillard (2009), An experimental investigation of gravity-driven shale tectonics in progradational delta, Tectonophysics, 474, 643–656.

Pons, A., and R. Mourgues (2012), Deformation and stability of over-pressured wedges: Insight from sandbox models, Journal of Geophysical Research, 117 (B09404), doi:10.1029/2012JB009379.

Sallarés, V., and C. R. Ranero (2005), Structure and tectonics of the erosional convergent margin off antofagasta, north chile (23 degrees 30' s), Journal of Geophysical Research, 110 (B06101), doi:10.1029/2004JB003418.

von Huene, R., and C. R. Ranero (2003), Subduction erosion and basal friction along the sediment-starved convergent margin off antofagasta, chile, Journal of Geophysical Research, 108 (B2), doi:10.1029/2001JB001569.

Withjack, M. O., Q. T. Islam, and P. R. Lapointe (1995), Normal faults and their hanging-wall deformation – an experimental study, AAPG Bulletin, 79 (1), 1–18.

Xiao, H.-B., F. A. Dahlen, and J. Suppe (1991), Mechanics of extensional wedges, Journal of Geophysical Research, 96 (B6), 301–318.

Yuan, X. P., Y. M. Leroy, and B. Maillot (2014), Tectonic and gravity extensional collapses in over-pressured cohesiveand frictional wedges, to prepare.

4D Transfer Zone Modeling in Continental Rifts

Frank Zwaan, Guido Schreurs

University of Bern, Switzerland
e-mail: *frank.zwaan@geo.unibe.ch*
session: *Tectonics and Surface Processes*

Introduction

Inherited structures in the Earth's crust are generally considered to represent weak zones along which deformation will focus during subsequent tectonic phases. In extensional settings, such as the Cenozoic European Rift System, the East African Rift System and many others (fig. 1), faulting initiated along such structures. However, to develop a full-scale rift system, these initial faults have to connect, which is usually achieved through transfer zones. Those transfer zones themselves might also follow the course of an inherited structural grain, as is the case in for example the Rhine-Bresse Transfer Zone (Ustaszewski et al., 2005).

The development of transfer zone structures has been investigated by means of analogue modeling. However, most of these studies focus on the oceanic domain and the well-known transfer faults associated with mid-oceanic ridges (eg. Serra & Nelson, 1988; Mauduit & Dauteuil, 1996; Dauteuil et al., 2002; Amibilia et al., 2005). Other studies do focus on the continental domain, but only in the shallow crust (Acocella et al., 1999; Ustaszewski et al., 2005). Basile & Brun (1999) do consider the whole (brittle/ductile) continental crust, but only in a pull-apart setting. All studies mentioned above have in common that they apply a rigid base plate to force localized deformation in overlying sand, clay and/or silicon layers.

The models from Acocella et al. (1999) are taken as a starting point to investigate the influence of inherited crustal weakness geometries on the development of transfer zones in continental rift systems. The model series described here improves upon the previous models by 1) considering the complete continental crust and 2) by the application of a method that creates a more natural, distributed type of deformation than the rigid base plate set-up.

Model Set-up & Methods of Analysis

The machine used for the experiments consisted of two long rigid walls between which a series of 78 cm long, 5 cm high plexiglass and foam bars were tightly stacked to fill the 25 cm wide initial gap (fig. 2A). By moving the walls apart using computer-controlled motors, the decompressing foam expands and fills the extra space. This system allows a uniform extensional deformation at the base of any overlying model materials. In addition, one of the base plates can move laterally, which allows strike-slip and transtensional set-ups. A rubber wall confined the short sides of the models, to ensure uniform extension and to minimize border effects.

To model the ductile lower continental crust, a 1 cm thick layer of PDMS (RGB-0910) silicone putty was placed on the foam/plexiglass base. For the brittle upper crust, a 2 cm thick cover of fine quartz sand was sieved on top of the PDMS, intercalated with thin layers of dark corundum sand to visualize displacement in sections. For further material characteristics, see Buiter et al., (2006) and Panien et al., (2006). The 3 cm of sand and silicone represents a 30 km thick crust. To create pre-existing weak zone, lines of silicone

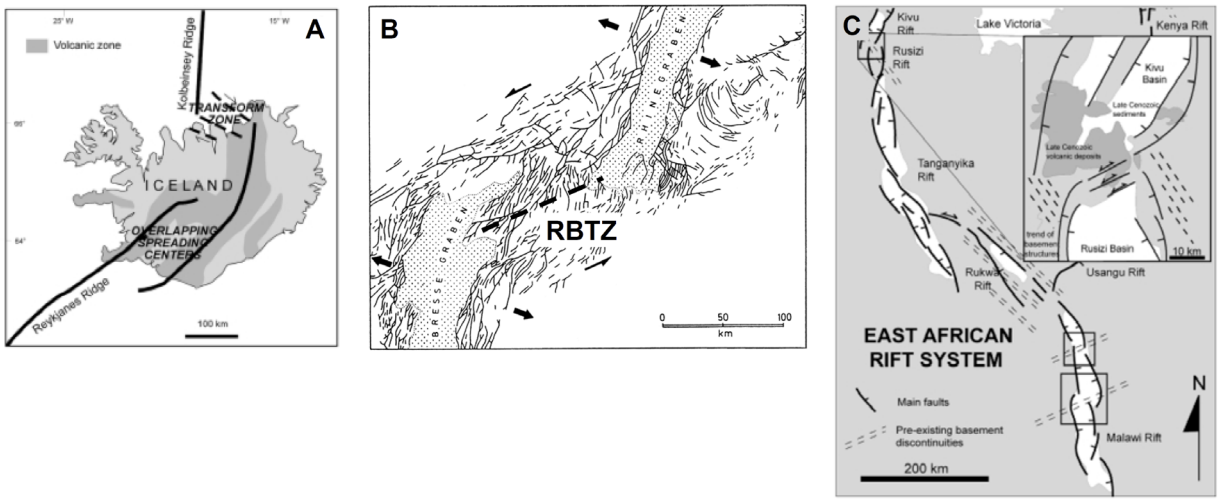

Fig. 1.: Examples of transfer zones in extensional settings: A) Iceland and the Mid Atlantic Ridge, (modified after Acocella et al., 1999); B) The Rhine-Bresse Transfer Zone (RBTZ), which is part of the Cenozoic European Rift System, between the Rhine and Bresse Grabens, eastern France (modified after Illies, 1977); C) The East African Rift System (modified after Acocella et al., 1999).

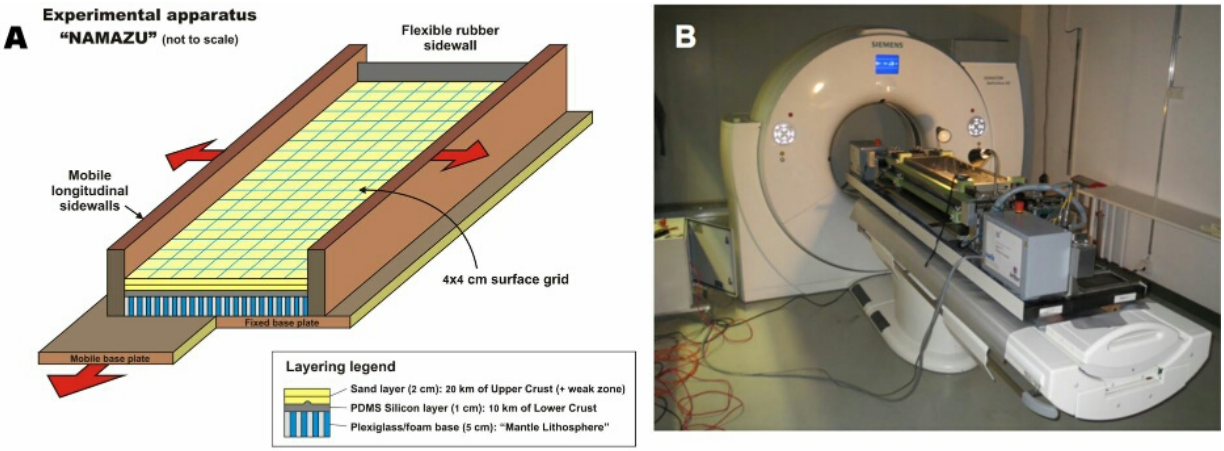

Fig. 2.: A) Model set-up, using a foam and plexiglas base, which allows distributed deformation. Image modified after Schreurs & Colletta (1998); B) CT-scanner installation with the sandbox machine during a model run.

(5x5 mm in diameter) were laid down on top of the basal silicone layer. The extension velocities were in the order of 0.6 cm/h, or ca. 10 mm/y in nature, using the scaling formulas from Corti et al., (2003) and data from Bürgmann & Dresen (2008).

Top view photographs were taken in order to follow the surface evolution. Additional cross-sections were made to observe the final structures at the end of each model run. Furthermore, several models were run in a CT-scanner to reveal the evolution of internal structures while the model was running (fig. 2B).

Results & Discussion

A series of 7 models was completed and interpreted (fig. 4). A first order observation is that the localization of deformation along the longitudinal weak zones worked well, all models developed distinct rift structures. However, several models did not produce linkage between both rift zones, which is an important difference with the results from previous studies. Only in model Tz1, the

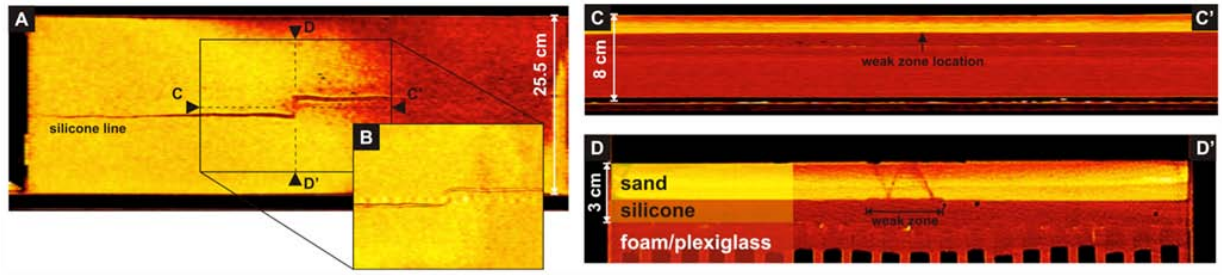

Fig. 3.: CT Sections trough model Tz7 after 60 minutes, showing the lack of deformation along the weak zone between both rift arms. A) Horizontal section at weak zone level, showing the weak zone geometry (compare with fig. 4); B) Horizontal section ca. 5 mm higher than slice A, indicating fault activity (darker lines) along the longitudinal weak zones, but no faulting occurs along the connecting weak zone. The same is evident in sections C-C' and D-D': normal faults are clearly present (D), but the weak zone in between is not active at all (C). For locations of these sections, see A.

45° oriented weak zone was clearly activated. Although the curved rift in model Tz6 seems to follow the weak zone, it actually cuts trough it. In addition, the successful linkage in models Tz5 and Tz7 was not the result of weak zone activation (see the CT imaging in fig. 3), but was most likely due to the close proximity of both rift arms; in the other models the rifts are just too far apart to join. This outcome can be explained by the lack of cohesion in sand (Van Mechelen, 2004): the sand layer is not strong enough to act as a rigid whole. This view is supported by a later experiment in which wet sand was applied and transfer zones did activate.

The models without linkage show propagation of the rift structures along strike of the longitudinal weak zones, but they also show a slightly curving towards the center of the model (model Tz4 did not yet, but shows the same early evolution as model Tz3). These structures are somewhat similar to the overlapping spreading centers in SW Iceland (fig. 1A), although Iceland is situated in an oceanic setting while the models were meant to represent a continental system. In contrast, models Tz5 and Tz7 did develop a linked transfer zone and seem to be quite similar (although a 31° oblique extension was applied to model Tz7). The results are roughly comparable to the structures in the Rhine-Bresse Transfer Zone (fig. 1B): two parallel deep graben structures connected by a less subsided oblique fault zone.

Model Tz6 shows some interesting results; both rift arms have developed in a completely different fashion with respect to each other and with respect to those in the other models of this series. The upper graben (a) has a more normal fault character with little oblique features and propagated furthest. This propagation was oriented perpendicular to the (31° oblique) direction of extension and created corresponding normal faulting. The lower graben (b) on the other hand has developed more oblique features, which are perpendicular to the extension direction. Its propagation shows a strong curve, which might have been influenced by the weak zone. But CT imaging shows that the structure cuts right trough the weak zone; the latter did not activate significantly.

Conclusions and future modeling

The results of this first series of transfer zone models have lead to the following conclusions:

1. The presence of high angle (at least $> 45°$) pre-existing weak zone does not define the occurrence of linkage between two graben structures, although this is probably due to the low cohesion of sand;

2. In contrast, the distance between both rift arms determines the occurrence of linkage here;

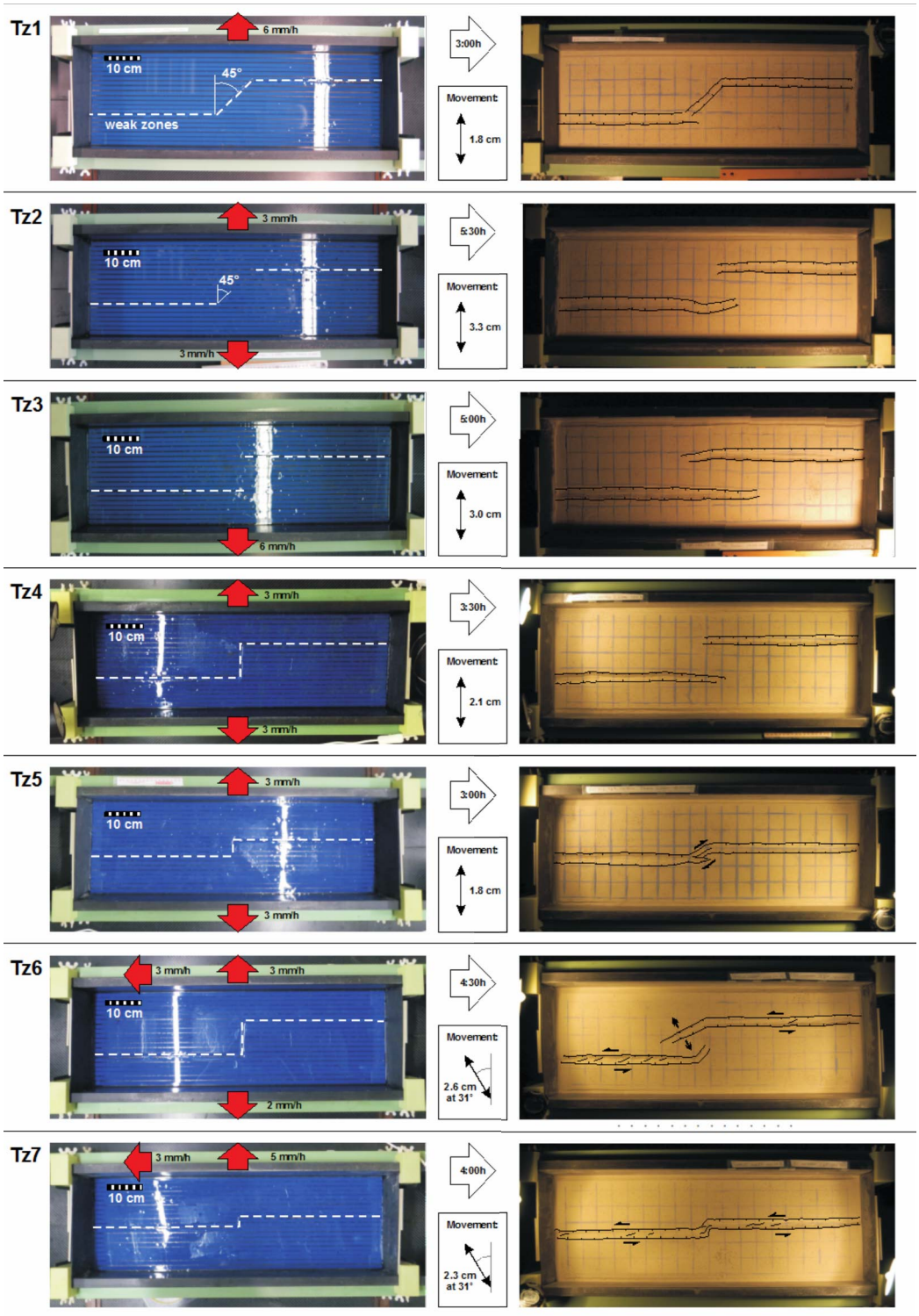

Fig. 4.: Left: Top views of the model set-up showing the weak zone geometry (white dotted lines) and the deformation vectors (red arrows, indicating the extensional deformation and for the transtensional models Tz6 and Tz7, the additional strike-slip components); Right: the resulting surface structures. NB: all models did produce half-graben structures along the longitudinal sidewalls, but these boundary effects were considered not to have a major influence on the structures in the center of the model.

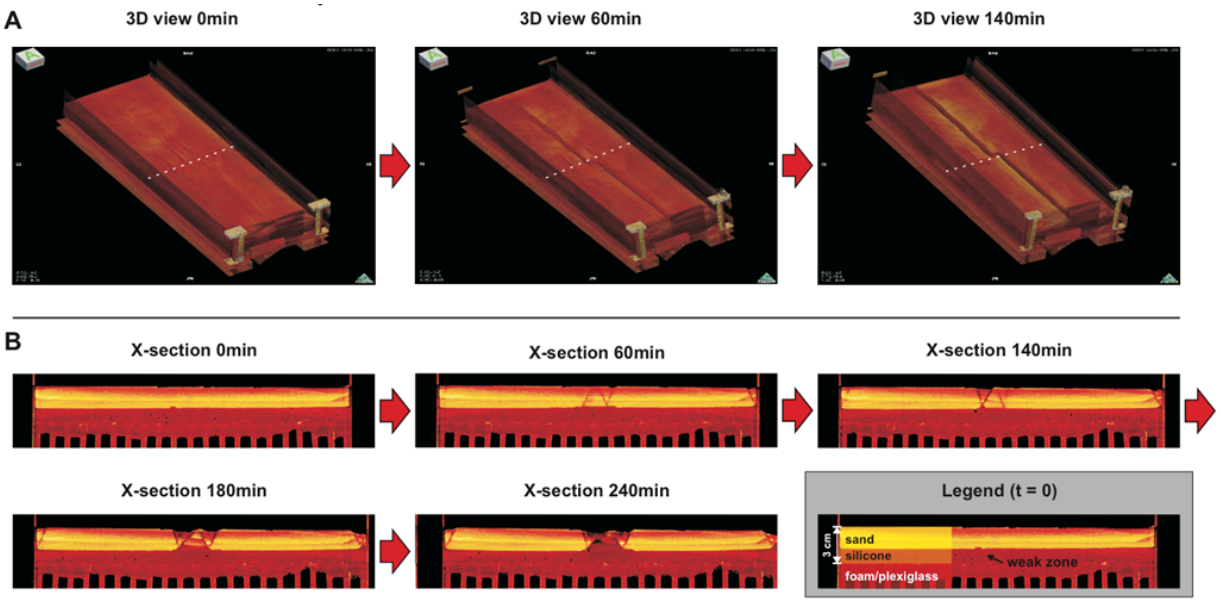

Fig. 5.: Application potential of CT data. A) 3D views of model Tz7, showing the initial model and the deformation after 60 minutes and 140 minutes; B) Cross-sections at the center of model Tz7 (for section locations, see dotted lines in A), showing the progressive deformation through time.

3. Oblique extensional deformation creates rather different structures with respect to orthogonal rifting;

4. Some models resemble natural examples (Iceland, Rhine-Bresse Transfer Zone).

It is however clear that more research is needed to fully describe the system. The top view photos of all models have to be examined in more detail and the available CT data from models Tz4-Tz7 has to be thoroughly analyzed. Also digital image correlation techniques could be applied, especially since the CT data allow motion tracing in 3D. These results should then be compared to those from previous modeling studies and with natural examples.

This model series was part of a PhD project start-up, and partially aimed to test the potential of the newly adjusted sandbox machine in Bern. Future work within this project will mostly focus on transtensional settings: different plate geometries and the modeling of natural examples of oblique extension: e.g. the Norwegian margin, the Knipovich Rigde near Svalbard and the Mid-Atlantic Ridge around Iceland. Also, collaboration with colleagues from the numerical domain will be arranged, to fully combine and exploit the possibilities of both sides of the modeling spectrum.

References

Acocella, V., Faccenna, C., Funiciello, R., Rossetti, F. (1999) Sand-box modelling of basement-controlled transfer zones in extensional domains. Terra Nova, Vol. 11, No. 4, pp 149-156

Amilibia, A., McClay, K. R., Sabat, F., Munoz, J.A., Roca, E. (2005) Analogue Modelling of Inverted Oblique Rift Systems. Geologica Acta, Vol. 3, No. 3, pp 251-271

Basile, C., Brun, J.-P. (1999) Transtensional faulting patterns ranging from pull-apart basins to transform continental margins: an experimental investigation. Journal of Structural Geology, Vol. 21, pp 23-37

Buiter, S. J. H., Babeyko, A. YU., Ellis, S., Gerya, T. V., Kaus, B. J. P., Kellner, A., Schreurs, G., Yamada, Y. (2006) The numerical sandbox: comparison of model results for a shortening and an extension experiment. In: Buiter, S. J. H., Schreurs, G. (eds.) Analogue and Numerical Modelling of Crustal-Scale Processes. Geological Society, London, Special Publications, Vol. 253, pp 29-64

Bürgmann, R., Dresen, G. (2008) Rheology of the Lower Crust and Upper Mantle: Evidence from Rock Mechanics, Geodesy and Field Observations. Annual Review of Earth and Planetary Sciences, Vol. 36, pp 531-567

Corti, G., Bonini, M., Conticelli, S., Innocenti, F., Manetti, P., Sokoutis, D. (2003) Analogue modeling of continental extension: a review focused on the relations between the patterns of deformation and the presence of magma. Earth-Science Reviews, Vol. 63, pp 169-247

Dauteuil, O., Bourgeois, O., Maudit, T. (2002) Lithosphere strength controls oceanic transfer zone structure: insights from analogue models. Geophysical Journal International, Vol. 150, pp 706-714

Illies, J. H. (1977) Ancient and recent rifting in the Rhinegraben. In: Frost, R. T. C., Dikkers, A. J. (eds., 1977) Fault tectonics in N.W. Europe. Geologie en Mijnbouw, Vol. 56, pp 329-350

Mauduit, T., Dauteuil, O. (1996) Small-scale models of oceanic transform zones. Journal of Geophysical Research, Vol. 101, No B9, pp 20,196-20,209

Panien, M., Buiter, S. J. H., Schreurs, G., Pfiffner, O. A. (2006) Inversion of a symmetric basin: insights from a comparison between analogue and numerical experiments. In: Buiter, S. J. H., Schreurs, G. (eds.) Analogue and Numerical Modelling of Crustal-Scale Processes. Geological Society, London, Special Publications, Vol. 253, pp 2253-2270

Schreurs, C., Colletta, B. (1998) Analogue modeling of faulting zones of continental tanstension and transpression. In: Holdsworth, R. E., Strachan, R. A., Dewey, J. F. (eds.) Continental Transpressional and Transtensional Tectonics. Geological Society, London, Special Publications

Serra, S., Nelson, R. A. (1988) Clay modeling of rift asymmetry and associated structures. Tectonophysics, Vol. 153, pp 307-312

Ustaszewski, K., Schumacher, M.E., Schmid, S M., Nieuwland, D. (2005) Fault reactivation in brittle-viscous wrench systems-dynamically scaled analogue models and application to the Rhine-Bresse transfer zone. Quaternary Science Reviews, Vol. 24, pp 365-382

Van Mechelen, J. L. M. (2004) Strength of moist sand controlled by surface tension for tectonic analogue modeling. Tectonophysics, Vol. 384, pp 275-284

Scientific Programme

GeoMod2014 - Conference Outline

Time	31. August	1. September	2. September	3. September
08:45 - 09:00	-	Welcome	-	-
09:00 - 11:00	-	(Seismo-)tectonics (orals)	Volcanism and Volcanotectonics (orals)	Rheology (orals)
11:00 - 13:00	-	(Seismo-)tectonics (posters)	Volcanism and Volcanotectonics (poster)	Rheology (poster)
13:00 - 14:00	-	Lunch break	Lunch break	Lunch break
14:00 - 16:00	-	Tectonics and Surface processes (orals)	Geodynamics (orals)	Fluids and Deformations (orals)
16:00 - 18:00	-	Tectonics and Surface processes (poster)	Geodynamics (posters)	Fluids and Deformations (poster)
18:00 - 21:00	Ice Breaker Party	-	-	-
19:00 - 22:00	-		Joint Conference Dinner	-

GeoMod2014 - Short course on "Constitutive Laws: from Observation to Implementation in Models" by Onno Oncken, Mathias Rosenau, Fabio Corbi, Georg Dresen Erik Rybacki, Stephan Sobolev, and Sascha Brune
Thursday 4 September: 09:00 - 18:00
Friday 5 September: 09:00 - 14:00

GeoMod2014 - Hands-on tutorial on "ASPECT: a next-generation geodynamic modelling software" by Anne Glerum and Juliane Dannberg
Thursday 4 September: 09:00 - 18:00: Tutorial
Friday 5 September: 09:00 - 18:00: ASPECT Strategy Workshop (for Advanced Users) - voluntary

GeoMod2014 Conference Programme (31 August - 3 September)

Sunday 31 August 2014

18:00 - 21:00: Ice Breaker Party at the 'Theaterschiff Potsdam' (Schiffbauergasse 9b, 14467 Potsdam)

Monday 1 September 2014

08:45 - 09:00: Welcome by Prof. Dr. Dr. h.c. Reinhard Hüttl and Prof. Dr. Onno Oncken

09:00 - 11:00: (Seismo-)tectonics Orals (chairs: B. Kaus, O. Oncken)

- 09:00 - 09:30: **Kelin Wang:** *Thermal Expressions of Stick-slip and Creeping Subduction Megathrusts* (keynote)
- 09:30 - 10:00: **Bertrand Maillot:** *The long-term Evolution of Fold-and-Thrust Belts: Consistency of Numerical Approaches and Physical Experiments* (keynote)
- 10:00 - 10:20: **Tasca Santimano** et al.: *Smart or Beautiful? Accretionary wedge evolution seen as a competition between minimum work and critical taper*
- 10:20 - 10:40: **Lorenzo Bonini** et al.: *The role of pre-existing frictional weaknesses on the propagation of extensional faults*
- 10:40 - 11:00: **Ylona van Dinther** et al.: *Seismo-thermo-mechanical modeling of subduction zone seismicity*

11:00 - 13:00: (Seismo-)tectonics Posters (chairs: B. Kaus, O. Oncken)

13:00 - 14:00: Lunch break

14:00 - 16:00: Tectonics and Surface processes Orals (chairs: F. Graveleau, N. Hovius)

- 14:00 - 14:30: **Ritske Huismans:** *Interaction and feedback between surface processes and mountain building* (keynote)
- 14:30 - 15:00: **Stéphane Dominguez:** *Joint analogue modelling of marine and terrestrial geological processes: state of the art and new developments* (keynote)
- 15:00 - 15:15: **Utsav Mannu** et al.: *Dynamic Modelling of Accretionary Prisms and Stratigraphy of Forearc basins*
- 15:15 - 15:30: **Karen Leever:** *3D Analogue Modelling of the Effect of Fan Sedimentation on Accretionary Wedge Dynamics – the Magdalena Fan case, South Caribbean Margin, Colombia*
- 15:30 - 15:45: **Frank Zwaan**, Guido Schreurs: *4D Transfer Zone Modeling in Continental Rift Systems*
- 15:45 - 16:00: **Sergei Medvedev**, Ebbe H. Hartz: *Evolution of topography of post-Devonian Scandinavia: Effects and rates of erosion*

16:00 - 18:00: Tectonics and Surface processes Posters (chairs: F. Graveleau, N. Hovius)

Tuesday 2 September 2014

09:00 - 11:00: Volcanism and Volcanotectonics Orals (chairs: O. Galland, E. Holohan)

- 09:00 - 09:30: **Rikke Pedersen:** *Surface deformation simulations of volcanic and tectonic processes in Iceland* (keynote)
- 09:30 - 10:00: **Olivier Roche**, Yarko Niño: *Mechanisms of entrainment of a granular substrate by pyroclastic density currents: insights from laboratory experiments and models, and implications for flow dynamics* (keynote)
- 10:00 - 10:15: **Rosanne Heistek** et al.: *Temporal changes in mantle wedge geometry and magma generation processes in the Central Andes: towards linking petrological data to thermomechanical models*
- 10:15 - 10:30: **Francesco Maccaferri** et al.: *The gravitational unloading due to rift depression: A mechanism for the formation of off-rift volcanoes in (continental) rift zones*
- 10:30 - 10:45: **Lola Chanceaux**, Thierry Menand: *Solidification effects on sill formation: an experimental approach*
- 10:45 - 11:00: Max Gallagher, **Ben Kennedy** et al.: *Megatsunami generation from caldera subsidence*

11:00 - 13:00: Volcanism and Volcanotectonics Posters (chairs: O. Galland, E. Holohan)

13:00 - 14:00: Lunch break

14:00 - 16:00: Geodynamics Orals (chairs: F. Funiciello, S. Sobolev)

- 14:00 - 14:30: **Anne Davaille:** *Plumes to Plate Tectonics: Insights from Laboratory Experiments* (keynote)
- 14:30 - 15:00: **Bernhard Steinberger** et al.: *On the relation between plate tectonics, large-scale mantle flow and mantle plumes: Some recent results and many open questions* (keynote)
- 15:00 - 15:15: **Paul J. Tackley** et al.: *Influence of Melting on the Long-Term Thermo-Chemical Evolution of Earth's Deep Mantle*
- 15:15 - 15:30: **Maria V. Chertova** et al.: *3-D numerical modeling of subduction evolution of the western Mediterranean region*
- 15:30 - 15:45: Tobias Baumann, **Boris Kaus**, A. Popov: *Constraining the rheology of the lithosphere through geodynamic inverse modelling*
- 15:45 - 16:00: **Elisa Calignano** et al.: *Strain localization during compression of a laterally heterogeneous lithosphere*

16:00 - 18:00: Geodynamics Posters (chairs: F. Funiciello, S. Sobolev), Methods and Materials Posters (chairs: M. Frehner, M. Rosenau)

19:00 - 22:00 Joint conference dinner in Potsdam on the ship 'Belvedere' (Lange Brücke 6, 14467 Potsdam)

Wednesday 3 September 2014

09:00 - 11:00: Rheology Orals (chairs: G. Dresen, H. Sone)

- 09:00 - 09:30: **Yuri Fialko:** *Numerical models of ductile roots of mature strike-slip faults* (keynote)
- 09:30 - 10:00: **Laurent Montési:** *Localization processes on Earth, Mars, and Venus* (keynote)
- 10:00 - 10:20: **Suzon Jammes** et al.: *Localization of deformation in a polymineralic material*
- 10:20 - 10:40: **Sebastian P. Müller** et al.: *Rheology of bubble- and crystal-bearing magma: new analogue experimental data and an effective-medium model*
- 10:40 - 11:00: **Maria A. Nikolinakou** et al.: *Modeling stress evolution around a rising salt diapir*

11:00 - 13:00: Rheology Posters (chairs: G. Dresen, H. Sone)

13:00 - 14:00: Lunch break

14:00 - 16:00: Fluids and Deformations Orals (chairs: S. Miller, M. Moreno)

- 14:00 - 14:30: **Boris Galvan** et al.: *Towards a general simulation tool for complex fluid-rock lithospheric processes: merging pre-processing, processing and post-processing in state-of-the-art computational devices* (keynote)
- 14:30 - 15:00: **Takeshi Tsuji:** *Digital rock physics: Insight into fluid flow and elastic deformation of porous media* (keynote)
- 15:00 - 15:15: **Thomas Heinze** et al.: *Numerical Modelling of earthquake swarms in the Vogtland / West- Bohemia*
- 15:15 - 15:30: **Samuel Angiboust** et al.: *Effect of Fluid Circulation on Intermediate-Depths Subduction Dynamics: From Field Observations to Numerical Modelling*
- 15:30 - 15:45: Magdalena Scheck-Wenderoth, **Judith Sippel** et al.: *Heat transport mechanisms at different scales – a 3D modelling workflow*
- 15:45 - 16:00: **Antoine Jacquey** et al.: *Modelling of fractured reservoirs: Fluid-rock interactions within fault domains*

16:00 - 18:00: Fluids and deformations Posters (chairs: S. Miller, M. Moreno)

The posters will be presented during the entire conference. Each poster session starts with a 1-2 min. short presentation of all participating posters.

GeoMod2014 - Short course on "Constitutive Laws: from Observation to Implementation in Models"

Thursday 4 September 2014

Morning Session: Onno Oncken, Mathias Rosenau, and Fabio Corbi

- 09:00 - 10:00: **Onno Oncken:** Observing deformation kinematics and localization: Observations from the field, geophysical imaging, and geodetic monitoring
- 10:00 - 10:15: Coffee Break
- 10:15 - 11:00: **Mathias Rosenau:** Rheology of rock analogues 1: Elastoplasticity and its application in seismotectonic simulation
- 11:00 - 11:15: Coffee Break
- 11:15 - 12:00: **Fabio Corbi:** Rheology of rock analogues 2: Viscoelasticity and its application in seismotectonic simulation
- 12:00 - 13:00: **Visit to the GFZ Analogue Lab**

13:00 - 14:00: Lunch break

Afternoon Session: Georg Dresen and Erik Rybackii

- 14:00 - 15:15: Rheology of the lower crust : Reconciling laboratory data and field observations
- 15:15 - 15:30: Coffee Break
- 15:30 - 16:45: **Visit to the GFZ rock mechanics lab**
- 16:45 - 17:00: Coffee Break
- 17:00 - 18:00: Rock fracture processes and stick slip sliding –What do we learn from analyzing nanofemto seismicity?

Friday 5 September 2014

Morning Session: Stephan Sobolev and Sascha Brune

- 09:00 - 10:00: **Stephan Sobolev:** Rheology and geodynamic modeling: key controls in plate tectonics and beyond
- 10:00 - 10:15: Coffee Break
- 10:15 - 11:30: **Sascha Brune:** Rock rheology in numerical models: PC exercises and application to rift dynamics
- 11:30 - 11:45 Coffee Break
- 11:45 - 12:30: **Stephan Sobolev:** Rheology and cross-scale modeling: towards understanding of great earthquakes
- 12:30 - 13:00: Discussion

13:00 - 14:00: Lunch and end of the short course

GeoMod2014 – Hands-on tutorial on"ASPECT: a next-generation geodynamic modelling software" by Anne Glerum and Juliane Dannberg

Thursday 4 September 2014

08:30 - 9:00: Registration

- 09:00 - 10:00: **Tutorial 1:** First Steps – Compiling and Running ASPECT, **Lecture:** How to run and visualize simple models
- 10:00 - 11:15: **Lecture** ASPECT – A next-generation geodynamic modelling software, **Tutorial 2:** Convection in a 2D box
- 11:15 - 11:30: Coffee Break
- 11:30 - 13:00: **Tutorial 3:** Using the adaptive mesh refinement and spherical shell geometry **Lecture:** How to run and visualize simple models

13:00 - 14:00: Lunch break

- 14:00 - 15:15: **Tutorial 4:** Using the adaptive mesh refinement and spherical shell geometry and using the function parser
- 15:15 - 15:30: Coffee Break
- 15:30 - 17:00: **Tutorial 5:** Averaging at the example of subduction and using a “sticky air” layer
- 17:00 - 18:00: **Voluntary:** Installing ASPECT on personal computers

18:30: Joint Dinner (to be payed by the participants)

Friday 5 September 2014

09:00 - 18:00: ASPECT Strategy Workshop for Advanced Users: Perspectives for Modelling with ASPECT

Index